CHARACTERISTICS AND DESIGN STRATEGIES FOR NEAR RECTILINEAR HALO ORBITS WITHIN THE EARTH-MOON SYSTEM

A Thesis

Submitted to the Faculty

of

Purdue University

by

Emily M. Zimovan

In Partial Fulfillment of the

Requirements for the Degree

of

Master of Science in Aeronautics and Astronautics

August 2017

Purdue University

West Lafayette, Indiana

THE PURDUE UNIVERSITY GRADUATE SCHOOL
STATEMENT OF THESIS APPROVAL

Professor Kathleen C. Howell, Chair

School of Aeronautics and Astronautics

Professor James M. Longuski

School of Aeronautics and Astronautics

Professor Carolin E. Frueh

School of Aeronautics and Astronautics

Approved by:

Professor Weinong Wayne Chen

Aeronautics and Astronautics Associate Head for Graduate Education

To the women in science, technology, engineering, and mathematics that have come before me, and to those that will come after me.

ACKNOWLEDGMENTS

First, a huge thank you for my parents. You instilled in me from a young age an invaluable love of math and science. Thank you for not just pushing me to question the world around me, but to find the answers. Without your encouragement and support, I would not be where I am today.

From the bottom of my heart, I want to thank my fiancé, Chris. When it felt like no one else in the world could understand where I was coming from or what I was going through, I knew that you actually did. I truly couldn't have done this without you. Your constant love and support mean the world to me. I'm grateful for you in so many ways.

I want to extend my immense gratitude to my advisor, Professor Kathleen C. Howell. Thank you for giving me so many opportunities throughout my time in the research group. Your thoughts, encouragement, advice, and support have been invaluable to my research and time at Purdue.

The members of my research group deserve a thank you, as well. You've listened to me present countless times over the past two years and have given me advice and thoughts that have led my research to where it is now. Thanks for helping me to learn all that I have.

I would also like to thank my committee members, Professors James M. Longuski and Carolin Frueh. I appreciate the time you took to review my thesis and provide me with advice and feedback. Additionally, for helping fund my studies at both Purdue University and NASA Johnson Space Center, I would like to thank the School of Aeronautics and Astronautics, the College of Engineering, and the Purdue University

Graduate School for awarding me with the Charles C. Chappelle Fellowship and the Ross Fellowship. Also, support provided by the NASA JSC NNX13AK60A grant is greatly appreciated. I am also grateful for the use of the outstanding facilities provided by the Rune and Barbara Eliasen Visualization Laboratory.

TABLE OF CONTENTS

Page

Page

Page

LIST OF TABLES

LIST OF FIGURES

Figure Page

Figure Page

Figure Page

Figure Page

ABSTRACT

Zimovan, Emily M. MSAAE, Purdue University, August 2017. Characteristics and Design Strategies for Near Rectilinear Halo Orbits Within the Earth-Moon System. Major Professor: Kathleen C. Howell.

A critical first step towards achieving the goal of a far-reaching human presence in space within the 21st century is the creation of a long-term crewed habitat in cislunar space, well beyond low Earth orbit. Thus, in support of this goal, an investigation is conducted into a class of candidate orbits, in the context of orbital characteristics and preliminary transfers to and from such trajectories. First, the periodic orbits of interest in the CR3BP are analyzed. Additionally, a metric, termed the apse angle, is introduced to quantify changes in orbital geometry once transitioned to a higher-fidelity ephemeris model. A detailed analysis of the southern L_2 halo family of orbits is presented and stability characteristics are used to delineate a favorable region denoted as the Near Rectilinear Halo Orbits (NRHOs). The NRHOs are stable or nearly-stable and, thus, can be maintained over a long duration for a relatively low cost indicating their suitability for a long-term habitat. A key consideration for many applications, synodic resonance is explored within the context of eclipse avoidance options. The geometry of synodic resonant NRHOs allows for the insertion epoch to dictate a simple lunar eclipse avoidance strategy. A straightforward direct transfer option from LEO to the L_2 southern NRHOs is detailed to determine Earth access to such a habitat. A low time of flight is suitable for crewed missions and is, therefore, the primary focus for feasible transfers. To transport humans to deep space destinations, transfers between orbits in cislunar space offer a proving ground to test capabilities and systems. Transfers from a habitat facility to translunar destinations may also require departure from alternative cislunar orbits. Thus, as an inaugural

step into the broader problem, transfers between a representative L_2 southern NRHO and the Distant Retrograde Orbits (DROs) are investigated.

1. INTRODUCTION

Similar to explorers that traveled far from their homelands to reach out and understand the new world, countless robotic probes have been sent by humans into deep space on exploration and science missions. However, a more far-reaching permanent presence beyond low Earth orbit, one that moves beyond exploration missions, is a near-term goal. An increasingly permanent human presence in the regions beyond the Earth-Moon system, similar to the first colonists that strived to build lasting communities in the new world, necessitates the construction of supporting infrastructure. A dynamical understanding of orbits in the Earth-Moon neighborhood that support long-term activities and orbital paths that link locations of interest form a critical step towards the creation of a lasting human presence. To initiate this process, interest has arisen in the construction of a facility in cislunar space to serve as a staging ground for missions within and beyond the Earth-Moon neighborhood. [1, 2] The Asteroid Redirect Mission (ARM) sparked the consideration of multi-body orbits for long-term mission scenarios in cislunar space through an investigation of the distant retrograde orbits. [3] In the near future, Exploration Mission-1 (EM-1) will deliver a human-rated vehicle to an orbit of this type as a technology demonstration of capabilities in a multi-body orbital regime. [4]

One particular application for a long-term facility in cislunar space is to serve as a habitat location for extended crewed operations and as a stepping-stone for human exploration of the solar system. The Deep Space Gateway (DSG) is currently planned as a largely Earth-independent long-term habitat on the far side of the Moon, to be constructed by the year 2027, in order to offer a proving ground for capabilities and systems, as well as a support platform for the future Deep Space Transport

(DST). [1,5] An orbit of interest to support this habitat mission is a southern L_2 near rectilinear halo orbit due to various favorable properties includuing relative stability, ease of communications with the Earth, and access to the lunar surface as well as translunar space. [6–9] However, fundamental questions concerning this type of orbit are yet unanswered. Thus, this investigation focuses on the characterization of the near rectilinear halo orbits in terms of their stability and eclipsing properties within the context of a potential long-duration human habitat. Primarily conducted within the circular restricted-three body model, some investigation into the effects of transitioning to a higher-fidelity ephemeris model are included, as well. A preliminary investigation into the accessibility of this orbit type from low Earth orbit is conducted in addition to the introduction of a basic methodology to access the distant retrograde orbits, another stable family in the vicinity. This investigation relies heavily on the work of prior authors, both in terms of progress in an understanding of multi-body dynamics and evolving computational abilities.

1.1 Previous Contributions

1.1.1 Multi-Body Dynamics

In 1687, with the publication of the *Principia*, Sir Isaac Newton (1643-1727) recorded the laws that govern the motion of N-bodies moving under the Universal Law of Gravitation. Thus began the search for an elusive analytical solution to the complex motion that governed the heavens. [10] Years later, in 1722, Leonhard Euler (1707-1983) simplified a model representing the N-body problem with the formulation of the Circular Restricted Three-Body Problem (CR3BP). [11] A truly key innovation, the view of the problem from the perspective of a rotating frame enabled significant progross. Then, with the assumption of an infinitesimal third body and primary bodies in circular orbits about their common barycenter, simplification

of the N-body problem allowed for the understanding of orbital motion to drastically increase. Joseph-Louis Lagrange (1736-1813) demonstrated the existence of the triangular equilibrium solutions to the CR3BP in 1772, the same year that Euler recognized the existence of the collinear libration points; the emergence of the equillibrium points led to additional understanding and insight into the problem. Over sixty years later, in 1836, an integral of the motion in the CR3BP, now known as the Jacobi integral or Jacobi constant, was noted by Carl Gustav Jacob Jacobi. [12] This integral or constant of the motion, bolstered insight into this dynamical regime and led to the recognition of the existence of bounding surfaces of allowable third body motion, the zero velocity surfaces, shown by Hill in 1878. [13]

Within the second volume of *Les Méthodes Nouvelles de la Mécanique Céleste*, Poincaré identified that no additional algebraic integrals of the motion exist in the CR3BP. [14] Since then, countless authors have explored the complex motion in this dynamical regime. In 1881, a technique to visualize complex solutions in the CR3BP was contributed by Henri Poincaré, now recognized as a Poincaré map. [12] This tool, not directly utilized by Poincaré due to computational limitations in in the early 1900s, offers invaluable insight into dynamical systems. However, not until 1978 was a mission proposed to exloit multi-body dynamical motion; the International Sun-Earth Explorer-3 (ISEE-3) spacecraft was inserted into a Sun-Earth L_1 halo orbit and was maintained for almost four years. [15] Since then, an increasing number of missions are incorporating these types orbits including ARTEMIS (Earth-Moon L_1 and L_2); SOHO, ACE, Genesis, and WIND (Sun-Earth L_1); and WMAP (Sun-Earth L_2). [16, 17]

1.1.2 Differential Corrections

Differential corrections methods, which date back to Newton's *Principia*, are a fundamental aspect of multi-body trajectory design. [10] Many different formulations

of differential corrections algorithms exist within the context of solving two-point boundary value problems. Authors such as Keller [18], as well as Roberts and Shipman [19, 20], produce shooting methods formulations in which a solution to a two-point boundary value problem is determined by integrating an appropriate intial value problem. [21] The advent of modern computers enabled the application of shooting methods to solve complex problems, e.g., trajectory design in the multi-body dynamical regime. A free-variable and constraint method, one specific formulation of a shooting scheme, as detailed by Pavlak, is implemented in this investigation. [22]

1.1.3 Periodic Orbits

As early as 1881, Poincaré demonstrated the existence of an infinite number of periodic solutions in the three-body problem. [14] Since then, many authors have focused on the construction and characterizion of these orbits. As an example, Moulton's collection of analytical methods for approximating periodic motion near the libration points in 1920 inspires continuing efforts. [23] However, large computational advances at the onset of the computer era have allowed many periodic solutions to be computed formally only within the last half-century. As recent samples of such efforts, Grebow characterizes and defines families of related periodic solutions in the CR3BP in an application to lunar south pole coverage [24] and Schlei develops an algorithm to identify many previously unknown planar periodic solutions and provides a significant number of examples. [25] Grebow's detailed overview of the development of periodic orbit solutions in the circular restricted three-body problem is particularly useful many additional references are supplied. [24]

Near Rectilinear Halo Orbits

'Halo' orbits, a term to describe a specific type of three-dimensional periodic orbit possessing a constant line of sight to the Earth, first appears in the literature in work by Farquhar in 1968. [8] Later, Breakwell and Brown, in 1979, demonstrate the existence of a family of related solutions, the family denoted as the L_2 halo orbits; a similar family bifurcating from an L_1 Lyapunov orbit also emerged. The L_1 halo family is characterized in the work by Breakwell and Brown and is also continued with representative periodic orbits from the planar Lyapunov orbit towards the increasingly three-dimensional orbits in the vicinity of the smaller primary. [6] Howell extends the families of L_1 and L_2 halo orbits to other systems in addition to offering a characterization of the L_3 halo family. [9] Notable for the current investigation, Howell and Breakwell (in 1983) develop an approximation for the stable "almost rectilinear halo orbits" within the L_1 and L_2 halo families for computational ease and, perhaps more significantly, also expand the understanding of this orbit type at the time. [7] These orbits are now termed Near Rectilinear Halo Orbits, or NRHOs. Favorable stability properties suggest their suitability for recent applications. Thus, investigation into stationkeeping methodologies for spacecraft in NRHOs are relevant and recent analyses conducted by Guzzetti et al. and Davis et al. are continuing. [26–28] Also key to any use in cislunar space, transfers to and from these orbits are available from various authors such as Capdevila [29], Folta et al. [30], Loucks et al. [31], and Whitley and Martinez. [32] An application to lunar south pole coverage by Grebow, Ozimek, Howell, and Folta in 2006 offered additional options. [33] A brief characterization of the NRHOs in terms of stability characteristics and eclipsing properties is offered by Zimovan et al. [34]

1.2 Current Work

In response to international interest in an infrastructure in cislunar space to allow for an enduring human presence beyond low Earth orbit, the main goal of this research effort is a further characterization of a particular class of orbits that are under current consideration. Continuing analysis of the Earth-Moon southern L_2 Near Rectilinear Halo Orbits (NRHOs) is conducted to gain an understanding of how unique characteristics of these orbits affect their suitability for a long-term space habitat. Additionally, transfers between these and other stable orbits also offer challenges; thus, techniques to design transfers between orbits that lack manifold structures are introduced. This investigation is organized as follows:

- **Chapter 2:** Dynamical Models – In this chapter, the equations of motion are derived for the circular restricted three-body problem and the N-body ephemeris model. Assumptions for each model are presented. The Jacobi constant, zero velocity surfaces, and equilibrium solutions are defined within the context of the circular restricted three-body problem.

- **Chapter 3:** Differential Corrections – Techniques that serve as the foundation for multi-body trajectory design are offered in this chapter. Multi-variable Newton's methods are discussed within the context of both a single-shooting and a multiple-shooting formulation along with common constraints and the derivation of the corresponding partial derivatives. The state transition matrix is derived for both the circular restricted three-body problem and the N-body ephemeris model. Coordinate frame transformations between the rotating frame and the inertial frame are summarized.

- **Chapter 4:** Trajectory Construction: CR3BP and the Ephemeris Model – In this chapter, strategies to compute periodic orbits in the circular restricted three-body problem are introduced. Two approaches to evolve families of related

solutions, i.e., natural parameter continuation and pseudo-arclength continuation, are examined. The distant retrograde orbits, period-3 distant retrograde orbits, as well as the L_1 and L_2 families of periodic halo orbits are discussed in detail. An introduction to manifold computation to explore the natural dynamical flow into and out of an orbit is offered. Poincaré mapping is introduced as a tool to effectively and concisely visualize dynamical motion. Additionally, a technique is suggested to transition converged solutions from the circular restricted three-body model to a higher-fidelity ephemeris model.

- **Chapter 5:** Mission Applications: Orbital Characteristics and Transfer Design – Stability characteristics in the form of the stability index delineate the near rectilinear halo orbits from the larger families of three-dimensional periodic halo orbits. Favorable stability properties for these orbits indicate a potential suitability for long duration, even human-rated, missions. Resonance is discussed in terms of both the sidereal and the synodic period, leading to an investigation into eclipse avoidance via orbital geometry and insertion epoch. A direct transfer option to the near rectilinear halo orbits from low Earth orbit is offered. Transfers between stable orbits that lack effective manifold structures are discussed within the context of transfers between the near rectilinear halo orbits and the distant retrograde orbits.

- **Chapter 6:** Concluding Remarks – First offered is a brief summary of the present investigation. Observations based on the characterization of the southern L_2 near rectilinear halo orbits are highlighted, particularly those that are relevant to a potential long-term facility in cislunar space. Concluding remarks concerning the set of preliminary transfer are included. Recommendations for future work are offered.

2. DYNAMICAL MODELS

Much of the trajectory design work in support of early mission concepts has been conducted in the simplified two-body problem. In this model, vehicle motion is modeled as Keplerian. In the two-body problem, the gravitational effects of two bodies, represented centrobaric point-masses, dictate the motion and other influences are neglected. For example, to model the motion of a satellite orbiting the Earth, a two-body formulation of the problem is reasonable. A tremendous advantage in employing a two-body formulation is the analytical closed-form solution. Thus, a two-body Keplerian model serves as a very successful preliminary design tool over a wide range of scenarios.

As mission concepts increase in complexity, however, the simple two-body model is not sufficiently accurate to allow for prediction and analysis of the true spacecraft motion. Once a preliminary understanding is accomplished by employing a two-body model, a deeper insight may be required to explore a multi-body design space. In addition, some behaviors may not emerge in a lower fidelity model, e.g., the two-body problem. To increase the fidelity of the dynamical model while retaining straightforward fundamental behaviors, an additional gravitational body can be included, resulting in a formulation based on three gravitational bodies. In fact, the Circular Restricted Three-Body Problem (CR3BP) is often satisfactory for preliminary investigations to gain a general understanding of the multi-body design space. For analysis of actual mission scenarios, however, a larger number of gravitational bodies must be introduced with a higher fidelity representation of all planetary states, as provided by the N-body ephemeris model.

2.1 The Circular Restricted Three-Body Model

The three-body problem includes three gravitationally attractive bodies (perhaps two celestial bodies plus a spacecraft) and each of the three bodies influence the motion of the others. Since the ratio of the mass of the Moon to the mass of the Earth is large compared to other planet-moon systems, a spacecraft in cis-lunar space is strongly influenced by both bodies simultaneously. Consequently, the CR3BP serves as a particularly effective model in preliminary design for applications within the Earth-Moon neighborhood. The CR3BP allows for rapid insight into the design space due to some key simplifications.

2.1.1 Assumptions for the Circular Restricted Three-Body Model

The general three-body problem is defined as the inclusion of three bodies, P_1, P_2, and P_3 (of masses m_1, m_2, and m_3, respectively) and each influences the others gravitationally. Note, however, that the general three-body problem requires three second-order vector differential equations to mathematically model the system behavior. Thus, 18 state variables are necessary in the problem ($6n$, where n is the number of bodies) and only ten known integrals of the motion are known to exist when formulated in terms of the inertial frame. As a consequence, an analytical closed-form solution is no longer achievable and numerical integration is required to explore the solution space. To further simplify the problem, the following assumptions lead directly to the reduced CR3BP formulation:

(a) The bodies are modeled as centrobaric point-masses only capable of translational motion.

(b) The third gravitational body, arbitrarily labeled P_3, possesses a significantly smaller mass than the other two bodies ($m_3 << m_1, m_2$); thus, P_3 does not influence the motion of P_1 or P_2.

(c) The primary bodies, arbitrarily labeled P_1 and P_2 (where $m_1 \geq m_2$), move in closed, Keplerian orbits about their common barycenter. This Keplerian motion is assumed to be circular for this formulation.

These three assumptions allow dynamical capture of multi-body dynamical behavior while permitting for straightforward analysis in a simplfied regime. Additionally, these assumptions lead to the autonomous nature of the CR3BP equations of motion as formulated in a rotating reference frame.

2.1.2 Equations of Motion in the Circular Restricted Three-Body Model

Development of the governing mathematical system in the CR3BP relies on the basic assumptions for the motion of the bodies; but, the derivation of the equations of motion is then straightforward. To supply context, the inertially fixed coordinate frame, I, denoted $\hat{X}$-$\hat{Y}$-$\hat{Z}$, is defined with an origin at the P_1-P_2 barycenter. The vectors $\hat{X}$-$\hat{Y}$-$\hat{Z}$ form a dextral, orthonormal triad. The geometry of the general inertial frame is illustrated in Figure 2.1. The primary bodies are assumed to move in a circular orbit relative to each other, thus, the inertially fixed coordinate frame is defined such that P_1 and P_2 lie in the $\hat{X}$-$\hat{Y}$ plane. The $\hat{Z}$-axis is conveniently defined as perpendicular to the orbital plane of the primaries (P_1, P_2) and is also parallel to the orbital angular momentum vector. The particle of interest, P_3, is free to move in all three spatial dimensions. Note, the vector locations of the particles under consideration with respect to the inertially fixed basepoint, B, are denoted by $\mathbf{r}_i$. In this investigation, bold lowercase letters indicate a vector quantity while non-bold lowercase is used to define vector magnitudes and other scalar quantities. Unit

vectors are marked with non-bold text beneath a carat, i.e., $\hat{\bullet}$. Matrices are denoted by boldface capital letters.

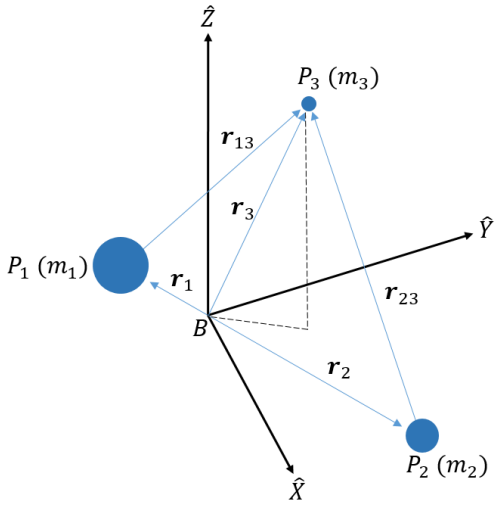

Figure 2.1. Geometry of a Three-Body System Defined in an Inertial Frame

The derivation of the equations governing the CR3BP originates with Newton's Second Law. [10] The motion of the particle of interest, P_3, under the gravitational influence of two other bodies, P_1 and P_2, is governed by the second-order vector differential equation

$$\mathbf{r}_3'' = -\frac{\tilde{G}m_1}{r_{13}^3}\mathbf{r}_{13} - \frac{\tilde{G}m_2}{r_{23}^3}\mathbf{r}_{23} \tag{2.1}$$

Here, $\tilde{G}$ represents the dimensional gravitational constant, and the position of particle P_i with respect to particle P_j is represented by the symbol $\mathbf{r}_{ij}$ such that $\mathbf{r}_{ij} = \mathbf{r}_i - \mathbf{r}_j$. The primes in this equation indicate differentiation with respect to dimensional time. These vectors are defined in an inertial reference frame.

For analysis in the CR3BP, an additional rotating coordinate frame is convenient. The rotating frame, R, first constructed by Euler in 1722, is defined by unit vectors

$\hat{x}$-$\hat{y}$-$\hat{z}$ as illustrated in Figure 2.2. [11] The $\hat{x}$-axis is parallel to the P_1-P_2 line and directed from P_1 towards P_2. The $\hat{z}$-axis is parallel to the inertial $\hat{Z}$-axis. Finally, the $\hat{y}$-axis completes the right-handed, orthonormal triad. Both the inertial and the rotating coordinate frames are centered at the P_1-P_2 barycenter. The orientation of the rotating frame is described by the angle θ which, due to the assumption of circular orbits of the primaries about the barycenter, evolves at a constant rate, i.e., $\theta = Nt$ where, at an initial time, t_0, $\theta_0 = \theta(t_0) = 0$. The value N represents the mean motion associated with the orbit of the primary bodies and t is the elapsed time since the rotating and inertial frames were aligned at t_0. Note, the arrow representing the projection of $\mathbf{r}_3$ into the plane of the primaries is dashed and denoted $\mathbf{r}_{3_p}$ where the subscript "p" indicates a projection and not the original vector. Body P_3 is free to move in all three spatial dimensions.

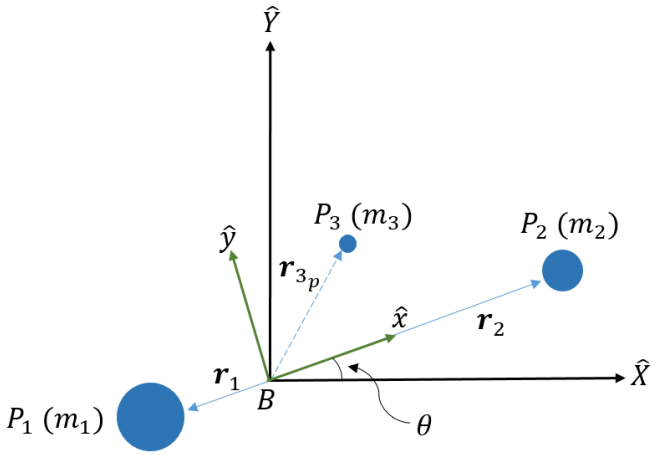

Figure 2.2. Inertial and Rotating Coordinate Frames Definitions

There is no closed-form analytical solution for motion in the CR3BP and therefore, numerical methods are employed. It is useful to nondimensionalize the differential equations to generalize results and to improve the numerical conditioning for integration. Some useful characteristic quantities for distance, mass, and time are

introduced. The characteristic length, l^*, is defined as the distance between the two primaries, i.e.,

$$l^* = r_1 + r_2 \tag{2.2}$$

where r_1 and r_2 are the magnitudes of their corresponding vectors $\mathbf{r}_1$ and $\mathbf{r}_2$. The characteristic mass, m^* is defined as the sum of the masses of the primaries

$$m^* = m_1 + m_2 \tag{2.3}$$

The nondimensional form of the gravitational constant, G, is defined as unity such that the characteristic time, t^*, by Kepler's Third Law is deduced as

$$t^* = \left(\frac{l^{*3}}{\tilde{G} m^*} \right)^{1/2} \tag{2.4}$$

The nondimensional mean motion, n, is then defined as

$$n = N t^* = \left(\frac{\tilde{G} m^*}{l^{*3}} \right)^{1/2} \left(\frac{l^{*3}}{\tilde{G} m^*} \right)^{1/2} = 1 \tag{2.5}$$

Some additional quantities that prove useful are

$$\mu = \frac{m_2}{m^*} \tag{2.6}$$

$$1 - \mu = \frac{m_1}{m^*} \tag{2.7}$$

$$\frac{r_1}{l^*} = \mu \tag{2.8}$$

$$\frac{r_2}{l^*} = 1 - \mu \tag{2.9}$$

For the Earth-Moon system, the characteristic quantities are summarized in Table 2.1. Additional characteristic quantities are reported in the table for the Sun-Earth system for comparison.

Table 2.1. Characteristic Quantities for Nondimensionalization

System	m^* [kg]	l^* [km]	t^* [sec]	μ
Earth-Moon	$6.046804e^{24}$	$3.844000e^{5}$	$3.751903e^{5}$	$1.215059e^{-2}$
Sun-Earth	$1.988800e^{30}$	$1.496500e^{8}$	$5.025263e^{6}$	$3.003486e^{-6}$

The dimensional equation of motion in Equation (2.1) can be rewritten in nondimensional form. The nondimensional position of P_3, with respect to the barycenter, in terms of rotating coordinates is expressed as

$$\boldsymbol{\rho} = \frac{\mathbf{r}_3}{l^*} = x\hat{x} + y\hat{y} + z\hat{z} \tag{2.10}$$

Additionally, the nondimensional relative position vectors can be defined as

$$\mathbf{d} = \frac{\mathbf{r}_{13}}{l^*} = (x+\mu)\hat{x} + y\hat{y} + z\hat{z} \tag{2.11}$$

$$\mathbf{r} = \frac{\mathbf{r}_{23}}{l^*} = (x-1+\mu)\hat{x} + y\hat{y} + z\hat{z} \tag{2.12}$$

Using these expressions, the nondimensional form of the second-order vector differential equation that governs the equations of motion for the CR3BP is defined as

$$\ddot{\boldsymbol{\rho}} = \frac{-(1-\mu)\mathbf{d}}{d^3} - \frac{\mu\mathbf{r}}{r^3} \tag{2.13}$$

where dots indicate differentiation with respect to nondimensional time, t.

The vector differential equation is then rewritten in terms of rotating components for application in the CR3BP. Note that $\dot{\boldsymbol{\rho}}$ is the nondimensional time derivative

of the position vector of P_3, relative to an inertial observer and expressed in terms of rotating frame coordinates and $\ddot{\boldsymbol{\rho}}$ refers to the acceleration of P_3 relative to an inertial observer expressed in the rotating frame. The kinematic expansion for these expressions are then derived from the basic kinematic equation as

$$\dot{\boldsymbol{\rho}} = \frac{{}^{I}d\boldsymbol{\rho}}{dt} = \frac{{}^{R}d\boldsymbol{\rho}}{dt} + {}^{I}\boldsymbol{\omega}^{R} \times \boldsymbol{\rho} \tag{2.14}$$

and

$$\frac{{}^{I}d^2\boldsymbol{\rho}}{dt^2} = \frac{{}^{R}d^2\boldsymbol{\rho}}{dt^2} + 2{}^{I}\boldsymbol{\omega}^{R} \times \frac{{}^{R}d\boldsymbol{\rho}}{dt} + {}^{I}\boldsymbol{\omega}^{R} \times {}^{I}\boldsymbol{\omega}^{R} \times \boldsymbol{\rho} \tag{2.15}$$

where the superscript I refers to an inertial observer, the superscript R refers to an observer in the rotating frame, and ${}^{I}\boldsymbol{\omega}^{R} = n\hat{z}$ is the nondimensional angular velocity of the rotating frame with respect to the inertial frame. Then, from Equation (2.14), the velocity relative to an inertial observer expressed in the rotating frame is given as

$$\dot{\boldsymbol{\rho}} = (\dot{x} - ny)\hat{x} + (\dot{y} + nx)\hat{y} + \dot{z}\hat{z} \tag{2.16}$$

and, from Equation (2.15), the kinematic expansion for the acceleration relative to an inertial observer and expressed in terms of rotating coordinates is

$$\ddot{\boldsymbol{\rho}} = (\ddot{x} - 2n\dot{y} - n^2x)\hat{x} + (\ddot{y} + 2n\dot{x} - n^2y)\hat{y} + \ddot{z}\hat{z} \tag{2.17}$$

Substituting Equation (2.17) into Equation (2.13) and decomposing the expression into scalar components yields three nondimensional second-order differential equations that govern the motion of the CR3BP

$$\ddot{x} - 2n\dot{y} - n^2x = \frac{-(1-\mu)(x+\mu)}{d^3} - \frac{\mu(x-1+\mu)}{r^3} \tag{2.18}$$

$$\ddot{y} + 2n\dot{x} - n^2y = \frac{-(1-\mu)y}{d^3} - \frac{\mu y}{r^3} \tag{2.19}$$

$$\ddot{z} = \frac{-(1-\mu)z}{d^3} - \frac{\mu z}{r^3} \tag{2.20}$$

Due to the assumptions consistent with the CR3BP, the equations of motion in the rotating reference frame are autonomous and the solutions to these differential equations are time-invariant. Through the introduction of the pseudo-potential function, U^*, where

$$U^* = \frac{1-\mu}{d} + \frac{\mu}{r} + \frac{1}{2}n^2(x^2+y^2) \tag{2.21}$$

the equations of motion, Equations (2.18) to (2.20), can be rewritten in an alternate form as

$$\ddot{x} - 2n\dot{y} = \frac{\partial U^*}{\partial x} \tag{2.22}$$

$$\ddot{y} + 2n\dot{x} = \frac{\partial U^*}{\partial y} \tag{2.23}$$

$$\ddot{z} = \frac{\partial U^*}{\partial z} \tag{2.24}$$

These nondimensional equations of motion, relative to the rotating frame, have no known analytical solution. To be analytically solvable, six integrals of the motion must exist for the rotating frame formulation. However, since only one integral of the motion exists in the rotating frame formulation of the problem, numerical integration is required.

2.1.3 Integrals of the Motion

In contrast to the Keplerian two-body problem, the differential equations in the CR3BP do not yield sufficient constants of the motion to produce an analytical closed-

form solution. However, one useful constant of the motion does emerge in the CR3BP rotating-frame formulation.

Jacobi Constant

One energy-like constant of the motion does exist in the rotating-frame formulation of the CR3BP. This scalar, termed the Jacobi constant, JC, provides significant insight into the dynamical behavior in the CR3BP and aids the process of numerical integration. To develop an expression for the Jacobi constant, the vector gradient of the pseudo-potential function,

$$\boldsymbol{\nabla} U^* = (\ddot{x} - 2\dot{y})\hat{x} + (\ddot{y} + 2\dot{x})\hat{y} + \ddot{z}\hat{z} \tag{2.25}$$

is dotted with the rotating velocity vector,

$$\dot{\boldsymbol{\rho}} = \dot{x}\hat{x} + \dot{y}\hat{y} + \dot{z}\hat{z} \tag{2.26}$$

to produce the relationship

$$\boldsymbol{\nabla} U^* \bullet \dot{\boldsymbol{\rho}} = \frac{\partial U^*}{\partial x}\dot{x} + \frac{\partial U^*}{\partial y}\dot{y} + \frac{\partial U^*}{\partial z}\dot{z} \tag{2.27}$$

or

$$\boldsymbol{\nabla} U^* \bullet \dot{\boldsymbol{\rho}} = (\ddot{x} - 2\dot{y})\dot{x} + (\ddot{y} + 2\dot{x})\dot{y} + \ddot{z}\dot{z} \tag{2.28}$$

Noting that the right side Equation (2.27) is equal to the total nondimensional time derivative of the pseudo-potential function, $\frac{dU^*}{dt}$, and the right side of Equation (2.28) is equal to $\ddot{\boldsymbol{\rho}} \bullet \dot{\boldsymbol{\rho}}$, the following expression results

$$\frac{dU^*}{dt} = \ddot{x}\dot{x} + \ddot{y}\dot{y} + \ddot{y}\dot{y} \tag{2.29}$$

Integrating Equation (2.29) with respect to nondimensional time produces

$$2U^* + 2\gamma = \dot{\rho}^2 \tag{2.30}$$

where γ is a *constant* of integration. Multiplying Equation (2.30) by $-\frac{1}{2}$ and rearranging allows for the definition of the Jacobi constant as

$$JC = 2U^* - \dot{\rho}^2 \tag{2.31}$$

Note that in the rotating frame formulation of the CR3BP, the Jacobi constant is the only integral of the motion.

Libration Points

Time-invariant equilibrium solutions to the autonomous equations of motion, Equations (2.18) to (2.20), are available. To determine the locations of the equilibrium points, the vector gradient of the pseudo-potential function is set to zero:

$$\boldsymbol{\nabla} U^* = \mathbf{0} \tag{2.32}$$

which yields

$$\frac{-(1-\mu)(x_{eq}+\mu)}{d_{eq}^3} - \frac{\mu(x_{eq}-1+\mu)}{r_{eq}^3} + n^2 x_{eq} = 0 \tag{2.33}$$

$$\frac{-(1-\mu)y_{eq}}{d_{eq}^3} - \frac{\mu y_{eq}}{r_{eq}^3} + n^2 y_{eq} = 0 \tag{2.34}$$

$$\frac{-(1-\mu)z_{eq}}{d_{eq}^3} - \frac{\mu z_{eq}}{r_{eq}^3} = 0 \tag{2.35}$$

where the subscript eq indicates equilibrium positions as identified in the rotating reference frame.

To compute the equilibrium solutions, Equations (2.33) through (2.35) must be simultaneously satisfied. From Equation (2.35) it is evident that $z_{eq} = 0$ and the equilibrium solutions are evidently in the plane of motion of the primaries. To solve for the x_{eq} and y_{eq} locations of the equilibrium points, two different approaches are pursued. First, defining y_{eq} as zero offers a solution to Equation (2.34). Then, x_{eq} is determined by substituting $y_{eq} = z_{eq} = 0$ into Equation (2.33), and then constructing the roots. There are three equilibrium solutions with $y_{eq} = z_{eq} = 0$ that exist on the x-axis, termed the collinear libration points. Two additional, off-axis equilibrium solutions appear by setting $d_{eq} = r_{eq} = 1$. The resulting equilibrium points form equilateral triangles with the primaries at two of the vertices. In total, there are five equilibrium solutions in the rotating frame–the collinear solutions and the triangular solutions, all in the plane of primary motion; the relative locations are plotted in Figure 2.3. These equilibrium points are frequently termed libration points or Lagrange points (due to the initial formulation by Lagrange in 1772 [12]).

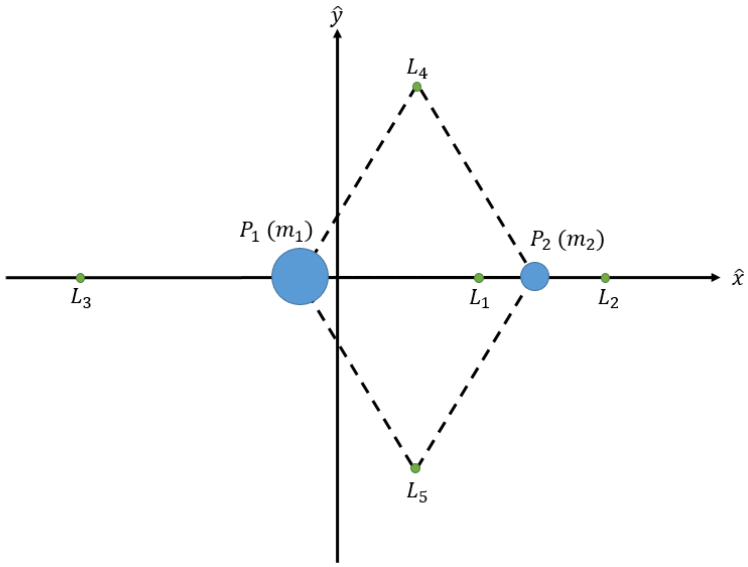

Figure 2.3. Location of the Libration Points as Viewed in the Rotating Frame

The equilibrium points, L_i, are numbered in the order of decreasing value of Jacobi constant; such a numbering is consistent with the order at which they become accessible with increasing orbital energy. Note, L_4 and L_5 become accessible at the same value of Jacobi constant but, by convention, L_4 reflects the equilateral point that leads the Earth-Moon line, i.e., a positive rotating $\hat{y}$ component, and L_5 is the mirror of L_4 across the rotating y-axis and lags behind the x-axis. For reference, the locations of the libration points in the Earth-Moon and Sun-Earth systems are included in Table 2.2. Additionally, the Jacobi constants for the Lagrange points in the Earth-Moon system are listed in Table 2.3.

Table 2.2. Rotating Coordinates of the Libration Points in the Earth-Moon and Sun-Earth Systems

System	Earth-Moon	Sun-Earth
$L_1(x, y, z)$ [nd]	$(0.836915, 0, 0)$	$(0.990027, 0, 0)$
$L_2(x, y, z)$ [nd]	$(1.155682, 0, 0)$	$(1.010034, 0, 0)$
$L_3(x, y, z)$ [nd]	$(-1.005063, 0, 0)$	$(-1.000001, 0, 0)$
$L_4(x, y, z)$ [nd]	$(0.487849, 0.866025, 0)$	$(0.499997, 0.866025, 0)$
$L_5(x, y, z)$ [nd]	$(0.487849, -0.866025, 0)$	$(0.499997, -0.866025, 0)$

Table 2.3. Value of the Jacobi Constant for each Libration Point in the Earth-Moon and Sun-Earth Systems

System	L_1	L_2	L_3	L_4	L_5
Earth-Moon	3.18834	3.17216	3.01215	2.98799	2.98799
Sun-Earth	3.04222	3.04025	3.00021	2.99979	2.99979

Zero Velocity Surfaces

The existence of the Jacobi constant leads to bounds on the allowable motion of the infinitesimal particle, P_3. [35] Such boundaries appear as surfaces in configuration space. The definition of the Jacobi constant, in Equation (2.31), is clearly rewritten as

$$\dot{\rho}^2 = 2U^* - JC \tag{2.36}$$

The fact that the physical velocity cannot be imaginary implies that $\dot{\rho}^2$ must be greater than or equal to zero; thus, an inequality relating JC and U^* results, i.e.,

$$2U^* \geq JC \tag{2.37}$$

This expression, where U^* is a function of x, y, and z, yields restrictions on the position of P_3 for a given value of JC. The collection of inaccessible positions, where the satisfaction of Equation (2.36) requires that the velocity of P_3 be imaginary, are frequently denoted "forbidden regions." The boundary of the forbidden region in configuration space is a three-dimensional set of surfaces that are a function of the value of JC. At the boundary, Equation (2.36) is satisfied when $\dot{\rho} = 0$. Thus, the surfaces that define the boundary are labelled the Zero-Velocity Surfaces (ZVSs). Projecting the ZVSs into the xy-plane yields the Zero-Velocity Curves (ZVCs). The ZVCs were first introduced by Hill in an application to a special case of the CR3BP, known as Hill's problem. [12] A sample ZVS and the corresponding ZVC's are plotted in Figure 2.4 for $JC_{L2} < JC < JC_{L3}$. Note that, since $JC < JC_{L2} < JC_{L1}$, the areas surrounding both L_1 and L_2 are accessible to P_3. In Figure 2.4(a), the near-spherical

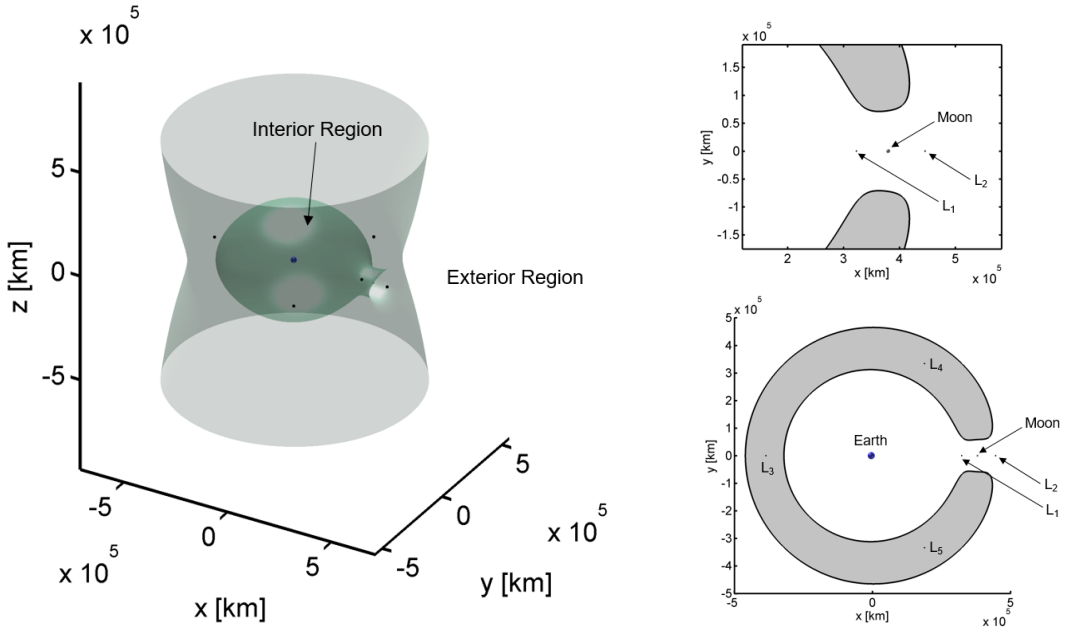

(a) Zero-velocity surface.

(b) Zero-velocity curve.

Figure 2.4. The ZVS and corresponding ZVC for $JC_{L3} < JC < JC_{L2}$. The forbidden regions are shaded in grey.

volume surrounding the larger primary, in this case, the Earth, is denoted as the interior region and is mostly bounded by the ZVS in three-dimensional space. The outer ZVS (in grey) appears nearly cylindrical in shape with an orientation parallel to the z-axis. The region beyond this outer ZVS is denoted the exterior region. The 3-D region between the inner ZVS (green) and the outer surface (grey) is not accessible, i.e., the forbidden region. Thus, to evolve from the interior region to the exterior region (or vice versa), P_3 must pass nearby the smaller primary, the Moon, through the narrow opening linking the interior and exterior regions. Clearly, knowledge of the ZVS at a given value of JC offers insight into potential P_3 trajectory evolutions.

As the value of the Jacobi constant decreases, the interior region expands and the outer ZVS boundary contracts; the spacecraft can then move throughout a larger area. The evolution is apparent by plotting the ZVC in the xy-plane. A few examples of ZVCs for decreasing values of JC appear in Figure 2.5. When JC is greater than JC_{L1} the interior region is separated into an area near P_1 and P_2, as apparent in (a). A spacecraft in the vicinity of P_1 does not possess the required orbital energy to reach P_2 and is captured about P_1; similarly, a spacecraft about P_2 cannot reach P_1 at this energy level. As the value of JC is decreased to be equivalent to JC_{L1}, the accessible areas surrounding each of the primaries expand until the ZVC converges to a single point at L_1 (reflected in (b)). Any further decrease in JC opens the gateway between the regions about the primaries into one accessible interior region, as illustrated in (c). Thus, the pathway linking the regions is termed the L_1 gateway and remains open whenever $JC < JC_{L1}$. The exterior region is *not* accessible from the interior region when $JC > JC_{L2}$, however. Further decreases in the Jacobi constant value to $JC = JC_{L2}$ again results in an increase in the accessible area and the ZVCs meet again in a single point at L_2, as noted in (d). Continually decreasing of the Jacobi constant value opens the L_2 gateway, as apparent in (e). Further decreases in the value of Jacobi constant shrinks the forbidden regions and shifts towards opening the L_3 gateway, as demonstrated in (f) and (g). At the Jacobi constant value equivalent

to JC_{L3}, the ZVC converges to a point at L_3. If $JC < JC_{L3}$, the L_3 gateway opens as well, i.e., Figure (h). The accessible region continues to increase for decreasing values of the Jacobi constant until $JC = JC_{L4} = JC_{L5}$ at which point the ZVCs are co-spatial with L_4 and L_5, and appear as a single dot in the xy-plane in the locations in (i); any further decrease in the Jacobi constant value results in the ZVC disappearing from the xy-plane. Of course, the ZVCs are simply a projection of the three-dimensional ZVS's onto the xy-plane. Significant regions of three-dimensional space may remain inaccessible even if the surfaces no longer intersect the plane of primary motion.

2.2 The N-Body Ephemeris Model

The CR3BP supplies a powerful tool for trajectory analysis and successfully models much of the behavior in the multi-body dynamical regime. However, some applications require a higher-fidelity model to incorporate perturbations from other bodies beyond those modeled in the CR3BP. The N-body ephemeris model is a higher fidelity alternative to the CR3BP. In the N-body ephemeris model, N gravitationally attractive bodies influence the motion of each of the other bodies in the system. These bodies are typically planets, moons, or other significant celestial objects, along with a spacecraft of interest. For spacecraft motion in cislunar space, the Earth, Moon, Sun, and Jupiter are generally the most influential bodies on the motion and are incorporated in this investigation.

2.2.1 Assumptions for the N-Body Ephemeris Model

The N bodies that comprise the ephemeris model, denoted P_j where $j = 1, ..., N$ (of mass m_j), each deliver some gravitational influence on the others. The following assumptions lead to the N-body ephemeris model formulation:

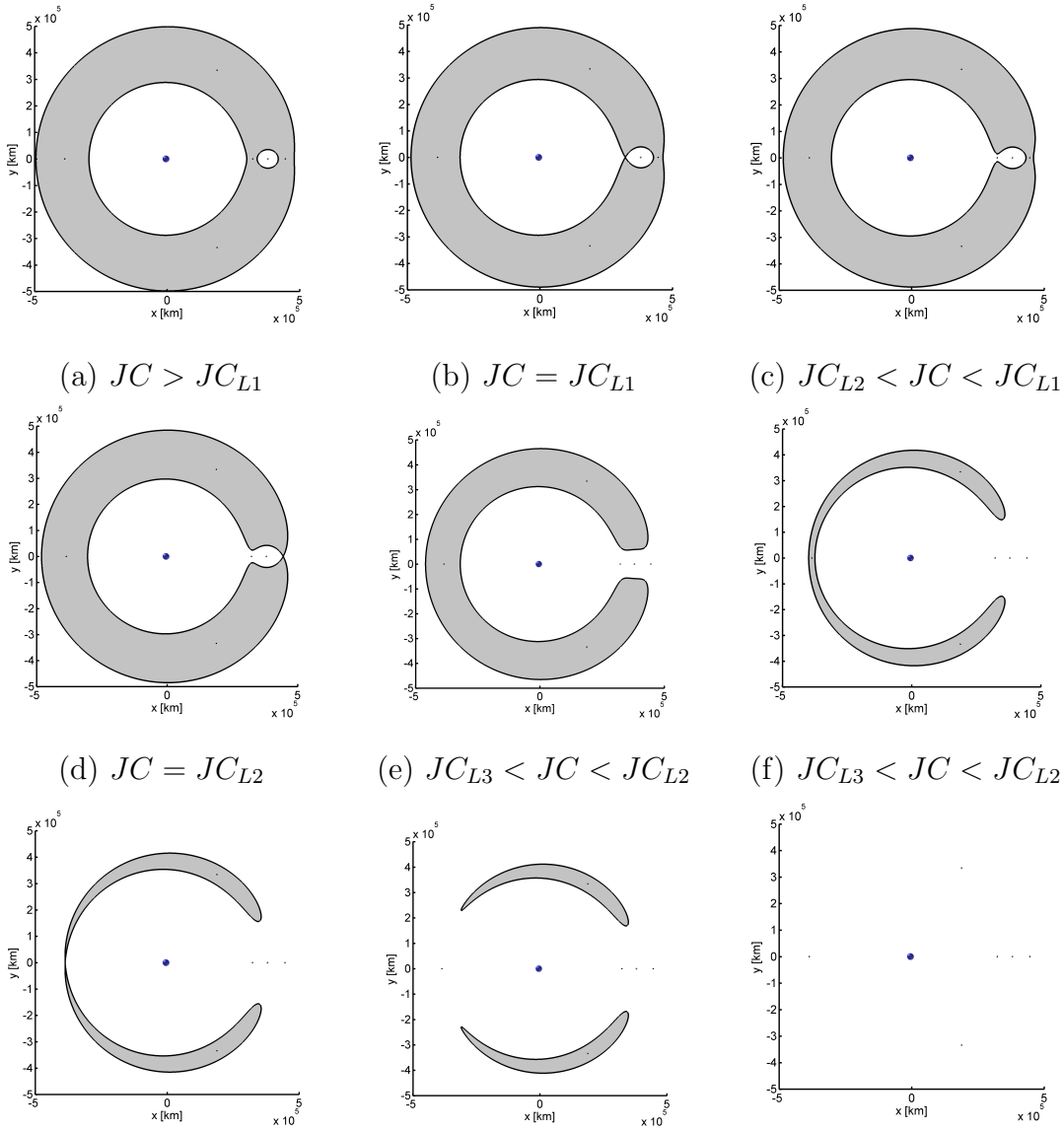

(a) $JC > JC_{L1}$ (b) $JC = JC_{L1}$ (c) $JC_{L2} < JC < JC_{L1}$

(d) $JC = JC_{L2}$ (e) $JC_{L3} < JC < JC_{L2}$ (f) $JC_{L3} < JC < JC_{L2}$

(g) $JC = JC_{L3}$ (h) $JC_{L4} < JC < JC_{L3}$ (i) $JC = JC_{L4} = JC_{L5}$

Figure 2.5. The ZVCs for decreasing values of Jacobi constant in the Earth-Moon three-body system. Earth and Moon are plotted twice their actual size. The forbidden regions are shaded in grey.

(a) Each body is assumed to be a centrobaric point-mass.

(b) The gravitational body of interest P_i possesses a significantly smaller mass than the other gravitational bodies ($m_i << m_j$ for $j = 1, ..., N \quad j \neq i$).

Note, no circular orbit assumptions are included in the derivation of this model. Instead, the trajectory paths associated with each body are obtained from the Jet Propulsion Laboratory's Navigation and Ancillary Information Facility (NAIF) SPICE ephemeris data. [36] Thus, the osculating eccentricity of the Moon's orbit about the Earth is accommodated in the Earth-Moon system. Additionally, the higher fidelity model is time-dependent or non-autonomous. The higher fidelity modeling of multi-body dynamical behavior allows for a wider range of representational environments.

2.2.2 Equations of Motion in the N-Body Ephemeris Model

To derive the equations of motion for the N-body ephemeris model, the differential equations are formulated in the inertial frame. The location of the body of interest, denoted P_i, evolves under the influence of $(N-1)$ perturbing bodies, denoted P_j. The N-body differential equations that describe the position of the body of interest, relative to an arbitrarily defined inertially fixed base point, are formulated using Newton's second law, i.e.,

$$m_i \mathbf{r}_i'' = -\tilde{G} \sum_{\substack{j=1 \\ j \neq i}}^{N} \frac{m_i m_j}{r_{ji}^3} \mathbf{r}_{ji} \tag{2.38}$$

which employs the familiar inverse square gravitational force. Of course, it is more useful to describe the location of the body of interest with respect to some central body, denoted P_k. The geometry of the inertial frame with multiple additional gravitational bodies, located from ephemeris data, appear in Figure 2.6 where the subscript i corresponds to the body of interest (typically a spacecraft), the subscript k indicates the central body, and subscripts j indicates any number of other perturbing bodies. A relative formulation of the N-body equations of motion that govern the motion of

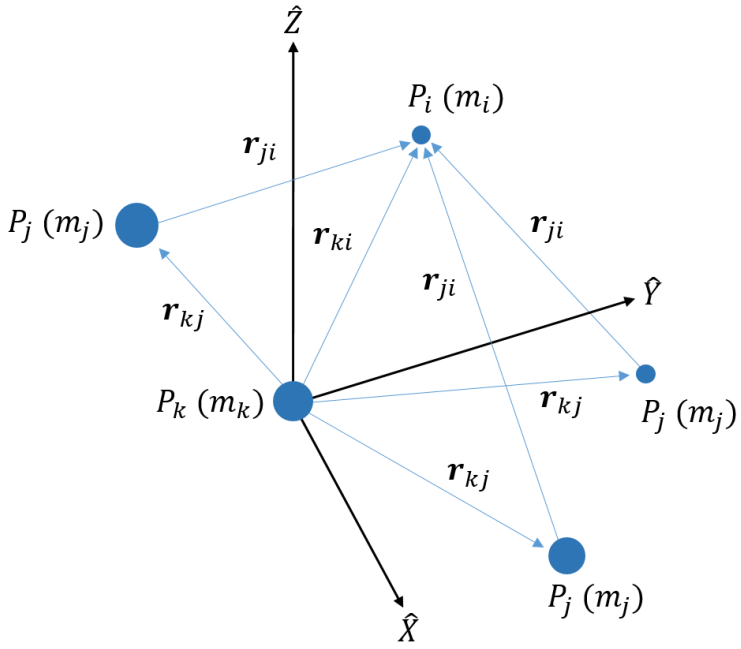

Figure 2.6. Inertial Frame Geometry of an N-Body System

the body of interest, P_i, with respect to the central body, P_k, under the influence of the central body and the other perturbing bodies, P_j, is written as:

$$\mathbf{r}''_{ki} = -\tilde{G}\left(\frac{m_i + m_k}{r_{ki}^3}\right)\mathbf{r}_{ki} + \tilde{G}\sum_{\substack{j=1 \\ j\neq i,k}}^{N} m_j\left(\frac{\mathbf{r}_{ij}}{r_{ij}^3} - \frac{\mathbf{r}_{kj}}{r_{kj}^3}\right) \tag{2.39}$$

The relative position vector, $\mathbf{r}_{kj}$, which represents the location of the perturbing bodies with respect to the central body, is obtained from NAIF's SPICE library [36] and uses DE430 planetary ephemerides. The vector $\mathbf{r}_{ij}$ is defined through vector subtraction, as

$$\mathbf{r}_{ij} = \mathbf{r}_{kj} - \mathbf{r}_{ki} \tag{2.40}$$

and represents the location of the perturbing bodies, P_j, with respect to the body of interest, P_i. For numerical integration and differential corrections purposes, Equation

(2.39) is often non-dimensionalized using characteristic quantities from the CR3BP, as listed in Table 2.1 for this investigation. Defining $\boldsymbol{\zeta}_{ab} = \frac{\mathbf{r}_{ab}}{l^*} = x_{ab}\hat{X} + y_{ab}\hat{Y} + z_{ab}\hat{Z}$, the nondimensional form of Equation (2.39) is

$$\ddot{\boldsymbol{\zeta}}_{ki} = -G\left(\frac{m_i + m_k}{\zeta_{ki}^3}\right)\boldsymbol{\zeta}_{ki} + G\sum_{\substack{j=1 \\ j\neq i,k}}^{N} m_j\left(\frac{\boldsymbol{\zeta}_{ij}}{\zeta_{ij}^3} - \frac{\boldsymbol{\zeta}_{kj}}{\zeta_{kj}^3}\right) \tag{2.41}$$

Due to the non-autonomous nature of these equations, a specific epoch date must be selected for each computation. Solutions are epoch-dependent and different epoch dates result in different solutions due to the changing relative positions of the perturbing bodies across various epoch dates.

3. DIFFERENTIAL CORRECTIONS

Closed-form analytical solutions to the governing equations of motion in the CR3BP and the N-body ephemeris model are not known to exist due to the lack of sufficient integrals of the motion. As a result, numerical strategies are employed to propagate trajectories in these models. But, arbitrary sets of initial conditions rarely yield the desired behavior. Thus, to meet design requirements, some form of differential corrections processes are necessary. In this investigation, corrections strategies based on multi-variable Newton's methods are applied to solve boundary value problems while satisfying a given set of constraints.

3.1 State Transition Matrix

Any corrections strategy is based on an assessment of the sensitivities. Thus, to implement various shooting methods, a scheme to relate variations or perturbations in the initial state, $\mathbf{x}(t_0)$, to variations in a downstream state, $\mathbf{x}(t, \mathbf{x}(t_0))$, must first be derived. The equations of motion are rewritten in first order form as $\dot{\mathbf{x}}(t) = \mathbf{f}(t, \mathbf{x}(t), \boldsymbol{\kappa})$ where the state vector is $\mathbf{x}(t) = [x(t) \quad y(t) \quad z(t) \quad \dot{x}(t) \quad \dot{y}(t) \quad \dot{z}(t)]^T$. Let, $\boldsymbol{\kappa}$ represent a vector of additional variables or parameters. For both the CR3BP and the N-body ephemeris models, $\mathbf{x}(t)$ represents the state vector of interest, i.e., in the CR3BP, $\mathbf{x}(t)$ is the state corresponding to P_3 at time t with respect to the barycenter of P_1 and P_2, and expressed in rotating coordinates; and, in the N-body ephemeris model, $\mathbf{x}(t)$ is the state of P_i relative to P_k and expressed in inertial coor-

dinates. In either model formulation, the vector variation relative to some nominal path is defined as

$$\delta\mathbf{x}(t) = \mathbf{x}(t) - \mathbf{x_n}(t) \tag{3.1}$$

where $\mathbf{x_n}(t)$ indicates a state on the reference or nominal path at some given time, t, and $\mathbf{x}(t)$ identifies a state on some nearby trajectory at time t. Using a first-order Taylor series expansion relative to the nominal path, the linear variational equations, derived from the equations of motion, are written in the form

$$\delta\dot{\mathbf{x}}(t) = \mathbf{A}(t)\delta\mathbf{x}(t) \tag{3.2}$$

where the matrix $\mathbf{A}(t)$ is the Jacobian matrix comprised of the partials of the equations of motion, $\mathbf{f}(t, \mathbf{x}(t), \boldsymbol{\kappa})$, with respect to the states evaluated at time t, i.e., $\mathbf{A}(t) = \frac{\partial \mathbf{f}(t,\mathbf{x}(t),\boldsymbol{\kappa})}{\partial \mathbf{x}(t)}$. The solution to Equation (3.2), in a linear sense, is written in the form of the matrix derivative that relates variations in the initial state to variations in the downstream state, i.e.,

$$\delta\mathbf{x}(t) = \left(\frac{\partial \mathbf{x}(t)}{\partial \mathbf{x}(t_0)}\right)\delta\mathbf{x}(t_0) \tag{3.3}$$

To determine the matrix $\frac{\partial \mathbf{x}(t)}{\partial \mathbf{x}(t_0)}$, the first-order differential equation governing its behavior is derived as follows

$$\frac{d}{dt}\left(\frac{\partial \mathbf{x}(t)}{\partial \mathbf{x}(t_0)}\right) = \frac{d}{d\mathbf{x}(t_0)}\left(\frac{\partial \mathbf{x}(t)}{\partial t}\right) = \frac{d}{d\mathbf{x}(t_0)}\dot{\mathbf{x}}(t) \tag{3.4}$$

which can be rearranged since $\mathbf{x}(t_0)$ and t are independent. Then, by the chain rule, Equation (3.4) is equivalent to

$$\frac{d}{dt}\left(\frac{\partial \mathbf{x}(t)}{\partial \mathbf{x}(t_0)}\right) = \frac{d}{d\mathbf{x}(t_0)}\dot{\mathbf{x}}(t) = \frac{\partial \mathbf{f}(t, \mathbf{x}(t), \boldsymbol{\kappa})}{\partial \mathbf{x}(t)}\frac{\partial \mathbf{x}(t)}{\partial \mathbf{x}(t_0)} = \mathbf{A}(t)\frac{\partial \mathbf{x}(t)}{\partial \mathbf{x}(t_0)} \tag{3.5}$$

Equation (3.5) leads to the definition of the STM, $\mathbf{\Phi}(t, t_0)$, as

$$\mathbf{\Phi}(t, t_0) = \frac{\partial \mathbf{x}(t)}{\partial \mathbf{x}(t_0)} \tag{3.6}$$

with the first-order matrix differential equation governing the evolution of the STM reduced to the form

$$\dot{\mathbf{\Phi}}(t, t_0) = \mathbf{A}(t)\mathbf{\Phi}(t, t_0) \tag{3.7}$$

as derived in Equation (3.5). The initial conditions for propagation of Equation (3.7) are $\mathbf{\Phi}(t_0, t_0) = \mathbf{I}_{6\times 6}$. The elements of the STM are determined from the $\mathbf{A}(t)$ matrix, then integrated with Equation (3.7) along with the equations of motion. Further derivations for the STMs associated with both the CR3BP and the N-body ephemeris models are detailed in the following subsections.

3.1.1 STM for the Circular Restricted Three-Body Model

The governing equations for the STM in the CR3BP in Equation (3.7) are numerically integrated along with the equations of motion governing the states. The equations for the individual STM elements are derived from the linear variational equations relative to a reference arc in the CR3BP. Any path or arc in the CR3BP is a nonlinear solution to Equations (2.22) through (2.24). Thus, the differential equations governing the variations, derived from the equations of motion of the CR3BP, are

$$\delta\ddot{x} - 2n\delta\dot{y} = \frac{\partial U^*}{\partial x \partial x}\delta x + \frac{\partial U^*}{\partial x \partial y}\delta y + \frac{\partial U^*}{\partial x \partial z}\delta z \tag{3.8}$$

$$\delta\ddot{y} + 2n\delta\dot{x} = \frac{\partial U^*}{\partial y \partial x}\delta x + \frac{\partial U^*}{\partial y \partial y}\delta y + \frac{\partial U^*}{\partial y \partial z}\delta z \tag{3.9}$$

$$\delta\ddot{z} = \frac{\partial U^*}{\partial z \partial x}\delta x + \frac{\partial U^*}{\partial z \partial y}\delta y + \frac{\partial U^*}{\partial z \partial z}\delta z \tag{3.10}$$

Equations (3.8) through (3.10) then form the matrix, $\mathbf{A}(t)$ in Equation (3.2), i.e.,

$$\mathbf{A}(t) = \begin{bmatrix} 0 & 0 & 0 & 1 & 0 & 0 \\ 0 & 0 & 0 & 0 & 1 & 0 \\ 0 & 0 & 0 & 0 & 0 & 1 \\ \frac{\partial U^*}{\partial x \partial x} & \frac{\partial U^*}{\partial x \partial y} & \frac{\partial U^*}{\partial x \partial z} & 0 & 2n & 0 \\ \frac{\partial U^*}{\partial y \partial x} & \frac{\partial U^*}{\partial y \partial y} & \frac{\partial U^*}{\partial y \partial z} & -2n & 0 & 0 \\ \frac{\partial U^*}{\partial z \partial x} & \frac{\partial U^*}{\partial z \partial y} & \frac{\partial U^*}{\partial z \partial z} & 0 & 0 & 0 \end{bmatrix} \tag{3.11}$$

The partial derivatives in $\mathbf{A}(t)$, in nondimensional form, appear as

$$\frac{\partial U^*}{\partial x \partial x} = 1 - \frac{1-\mu}{r_{13}^3} - \frac{\mu}{r_{23}^3} + \frac{3(1-\mu)(x+\mu)^2}{r_{13}^5} + \frac{3\mu(x-1+\mu)^2}{r_{23}^5} \tag{3.12}$$

$$\frac{\partial U^*}{\partial x \partial y} = \frac{\partial U^*}{\partial y \partial x} = \frac{3(1-\mu)(x+\mu)y}{r_{13}^5} + \frac{3\mu(x-1+\mu)y}{r_{23}^5} \tag{3.13}$$

$$\frac{\partial U^*}{\partial x \partial z} = \frac{\partial U^*}{\partial z \partial x} = \frac{3(1-\mu)(x+\mu)z}{r_{13}^5} + \frac{3\mu(x-1+\mu)z}{r_{23}^5} \tag{3.14}$$

$$\frac{\partial U^*}{\partial y \partial y} = 1 - \frac{1-\mu}{r_{13}^3} - \frac{\mu}{r_{23}^3} + \frac{3(1-\mu)y^2}{r_{13}^5} + \frac{3\mu y^2}{r_{23}^5} \tag{3.15}$$

$$\frac{\partial U^*}{\partial y \partial z} = \frac{\partial U^*}{\partial z \partial y} = \frac{3(1-\mu)yz}{r_{13}^5} + \frac{3\mu yz}{r_{23}^5} \tag{3.16}$$

$$\frac{\partial U^*}{\partial z \partial z} = 1 - \frac{1-\mu}{r_{13}^3} - \frac{\mu}{r_{23}^3} + \frac{3(1-\mu)z^2}{r_{13}^5} + \frac{3\mu z^2}{r_{23}^5} \tag{3.17}$$

where x, y, and z originate from the definition of $\boldsymbol{\rho} = \frac{\mathbf{r}_3}{l^*} = x\hat{x} + y\hat{y} + z\hat{z}$ in the CR3BP rotating frame. These analytical expressions in the $\mathbf{A}(t)$ matrix are employed in the integration of Equation (3.7) to deliver the STM in the CR3BP.

3.1.2 STM for the N-Body Ephemeris Model

Similar to the derivation for the partials in the $\mathbf{A}(t)$ matrix for application the CR3BP, the partial derivatives in the Jacobian matrix $\mathbf{A}(t)$ for the N-body ephemeris model are also available. These partials are constructed from the linear variational form of the equations of motion in Equation (2.41). Arranging the linear variational equations into matrix form yields the Jacobian matrix $\mathbf{A}(t)$,

$$\mathbf{A}(t) = \begin{bmatrix} 0 & 0 & 0 & 1 & 0 & 0 \\ 0 & 0 & 0 & 0 & 1 & 0 \\ 0 & 0 & 0 & 0 & 0 & 1 \\ A_{41} & A_{42} & A_{43} & 0 & 0 & 0 \\ A_{51} & A_{52} & A_{53} & 0 & 0 & 0 \\ A_{61} & A_{62} & A_{63} & 0 & 0 & 0 \end{bmatrix} \tag{3.18}$$

The $A_{4:6,1:3}$ elements of $\mathbf{A}(t)$ are derived to render the following expressions

$$A_{41} = G(m_i + m_k)\left(\frac{3x^2}{\zeta_{ki}^5} - \frac{1}{\zeta_{ki}^3}\right) + G\sum_{\substack{j=1 \\ j\neq i,k}}^{N} m_j\left(\frac{3x_{ij}^2}{\zeta_{ij}^5} - \frac{1}{\zeta_{ij}^3}\right) \tag{3.19}$$

$$A_{52} = G(m_i + m_k)\left(\frac{3y^2}{\zeta_{ki}^5} - \frac{1}{\zeta_{ki}^3}\right) + G\sum_{\substack{j=1 \\ j\neq i,k}}^{N} m_j\left(\frac{3y_{ij}^2}{\zeta_{ij}^5} - \frac{1}{\zeta_{ij}^3}\right) \tag{3.20}$$

$$A_{63} = G(m_i + m_k)\left(\frac{3z^2}{\zeta_{ki}^5} - \frac{1}{\zeta_{ki}^3}\right) + G\sum_{\substack{j=1 \\ j\neq i,k}}^{N} m_j\left(\frac{3z_{ij}^2}{\zeta_{ij}^5} - \frac{1}{\zeta_{ij}^3}\right) \tag{3.21}$$

$$A_{42} = G(m_i + m_k)\left(\frac{3xy}{\zeta_{ki}^5}\right) + G\sum_{\substack{j=1 \\ j\neq i,k}}^{N} m_j\left(\frac{3x_{ij}y_{ij}}{\zeta_{ij}^5}\right) \tag{3.22}$$

$$A_{43} = G(m_i + m_k)\left(\frac{3xz}{\zeta_{ki}^5}\right) + G\sum_{\substack{j=1 \\ j\neq i,k}}^{N} m_j\left(\frac{3x_{ij}z_{ij}}{\zeta_{ij}^5}\right) \tag{3.23}$$

$$A_{53} = G(m_i + m_k)\left(\frac{3yz}{\zeta_{ki}^5}\right) + G\sum_{\substack{j=1 \\ j\neq i,k}}^{N} m_j\left(\frac{3y_{ij}z_{ij}}{\zeta_{ij}^5}\right) \tag{3.24}$$

$$A_{51} = A_{42} \tag{3.25}$$

$$A_{61} = A_{43} \tag{3.26}$$

$$A_{62} = A_{53} \tag{3.27}$$

Recall that x, y, and z are derived for the vector $\boldsymbol{\zeta}_{ki}$ as $\boldsymbol{\zeta}_{ki} = \frac{\mathbf{r}_{ki}}{l^*} = x_{ki}\hat{X} + y_{ki}\hat{Y} + z_{ki}\hat{Z}$, denoted as $x\hat{X} + y\hat{Y} + z\hat{Z}$ in the inertial frame. The analytical expression for the $\mathbf{A}(t)$ matrix is employed to integrate Equation (3.7) and produce the N-body ephemeris model STM.

3.1.3 Monodromy Matrix

The monodromy matrix, denoted $\boldsymbol{\Phi}(t_0 + P, t_0)$, is equivalent to the STM evaluated over precisely one orbital period and corresponds to a discrete linear mapping. [35] The monodromy matrix has the following properties: [37]

1. The eigenvalues of the monodromy matrix are always in reciprocal pairs.
2. The determinate of $\boldsymbol{\Phi}(t_0 + P, t_0)$ must equal unity.
3. The monodromy matrix is symplectic.

The monodromy matrix, among many applications, is used to assess orbit stability and compute manifold arcs within this investigation. More specifically, the eigenvalues of this matrix, denoted λ_i, are used to assess the stability characteristics of a periodic orbit in a linear sense. Since the monodromy matrix offers discrete time information about the periodic orbit, the stability boundary is the unit circle. A linearly stable periodic orbit is identified by an eigenvalue with magnitude less than unity. An eigenvalue of the monodromy matrix with magnitude greater than one indicates instability. Eigenvalues equal to unity reflect orbit periodicity and the membership of the orbit to a family of related solutions. Additionally, changes in stability across an orbit family, as determined from the eigenvalues of the monodromy matrix, indicate that the family of orbits may encounter a bifurcation. A detailed discussion of bifurcation theory is given by Bosanac. [37]

3.2 Differential Corrections Strategies - Shooting Methods

Differential corrections methods are fundamental to multi-body trajectory design. Many different formulations for differential corrections algorithms exist, particularly focused on solving two-point boundary value problems. In this investigation, differential corrections formulated as shooting schemes are used to design trajectories to meet given constraints. The algorithm for the implementation of a shooting method allows for the manipulation of design variables to satisfy a set of given constraints. From among numerous types of implementation strategies, this analysis employs a free variable and constraint method. Let the free variable vector be defined as

$$\mathbf{X} = \begin{bmatrix} X_1 \\ X_2 \\ \vdots \\ X_n \end{bmatrix} \tag{3.28}$$

where the elements of $\mathbf{X}$ are the n design variables (i.e., the set of variables that are allowed to be modified in the problem). Typically, $\mathbf{X}$ contains state elements, integration times, epochs, and other quantities. The design variables can evolve subject to m scalar constraint equations in $\mathbf{F}(\mathbf{X}) = \mathbf{0}$, or,

$$\mathbf{F}(\mathbf{X}) = \begin{bmatrix} F_1(\mathbf{X}) \\ F_2(\mathbf{X}) \\ \vdots \\ F_m(\mathbf{X}) \end{bmatrix} = \mathbf{0} \tag{3.29}$$

The constraints are typically position, time of flight, or velocity constraints, although many other types of constraints are possible. A scheme to determine a free variable vector, $\mathbf{X}^*$, such that $\mathbf{F}(\mathbf{X}^*) = \mathbf{0}$ (that is, all of the constraint equations are satisfied simultaneously) is derived. An iterative process to solve for $\mathbf{X}^*$, given an initial guess

for the free variable vector, i.e., $\mathbf{X}^0$, is derived by expanding the constraint vector in a Taylor series about the initial guess:

$$\mathbf{F}(\mathbf{X}) = \mathbf{F}(\mathbf{X}^0) + \frac{\partial \mathbf{F}(\mathbf{X}^0)}{\partial \mathbf{X}^0}\left(\mathbf{X} - \mathbf{X}^0\right) + \dots \tag{3.30}$$

Denote $\frac{\partial \mathbf{F}(\mathbf{X}^0)}{\partial \mathbf{X}^0}$ as $D\mathbf{F}(\mathbf{X}^0)$, an $m \times n$ Jacobian matrix that is comprised of the partial derivatives of the constraints with respect to the free variables. Truncating the Taylor series in Equation (3.30) to first-order yields

$$\mathbf{F}(\mathbf{X}) = \mathbf{F}(\mathbf{X}^0) + D\mathbf{F}(\mathbf{X}^0)\left(\mathbf{X} - \mathbf{X}^0\right) \tag{3.31}$$

Noting that a solution implies $\mathbf{F}(\mathbf{X}) = \mathbf{0}$, Equation (3.31), written in an iterative update form, becomes

$$\mathbf{F}(\mathbf{X}^j) + D\mathbf{F}(\mathbf{X}^j)\left(\mathbf{X}^{j+1} - \mathbf{X}^j\right) = \mathbf{0} \tag{3.32}$$

where $\mathbf{X}^j$ is the current iteration of the free variable vector, $\mathbf{X}^{j+1}$ is the next iteration of the free variable vector, and $\mathbf{F}(\mathbf{X}^j)$ is the value of the current constraint vector as evaluated after propagating the equations of motion from the initial condition $\mathbf{X}^j$. Since the current free variable vector and value of the current constraint vector are known, $D\mathbf{F}(\mathbf{X}^j)$ is also available. An iteration process is initiated by employing Equation (3.32) as the update equation. Iterations continue until $\mathbf{F}(\mathbf{X}^{j+1}) = \mathbf{F}(\mathbf{X}^*) = \mathbf{0}$ to some acceptable tolerance. Rearranging Equation (3.32) to solve for $\mathbf{X}^{j+1}$ yields

$$\mathbf{X}^{j+1} = \mathbf{X}^j - D\mathbf{F}(\mathbf{X}^j)^{-1}\mathbf{F}(\mathbf{X}^j) \tag{3.33}$$

In this investigation, iteration on the free variable vector is typically stopped when $||\mathbf{F}(\mathbf{X}^{j+1})||_2 < 10^{-12}$. Here, the L^2 norm is employed, i.e., the square root of the sum of the squares of the elements in $\mathbf{F}(\mathbf{X}^{j+1})$.

If the design vector includes more free variables than the constraint vector, or $n > m$, there are infinitely many solutions to the update equation. In this investigation,

the minimum norm solution is selected. The minimum norm update equation is given by:

$$\mathbf{X}^{j+1} = \mathbf{X}^{j} - D\mathbf{F}(\mathbf{X}^{j})^{T}\left(D\mathbf{F}(\mathbf{X}^{j})D\mathbf{F}(\mathbf{X}^{j})^{T}\right)^{-1}\mathbf{F}(\mathbf{X}^{j}) \tag{3.34}$$

The minimum norm solution is used because it seeks a solution $\mathbf{X}^{j+1}$ that is closest to the initial guess $\mathbf{X}^{j}$. This yields a solution $\mathbf{X}^{*}$ that is as close as possible to $\mathbf{X}^{0}$ and will likely retain characteristics of the initial free variable vector.

3.2.1 Simple Targeting Scheme Formulation

One of the most basic corrections strategies is a simple targeting scheme. Sometimes termed a single shooting method, a single trajectory arc with the appropriate initial state vector is the solution to a two-point boundary value problem. The formulation of the free variable vector and constraint vector is problem dependent, however, the elements of the algorithm are consistent. Let the spacecraft initial state be defined as

$$\mathbf{x}(t_0) = \begin{bmatrix} x(t_0) & y(t_0) & z(t_0) & \dot{x}(t_0) & \dot{y}(t_0) & \dot{z}(t_0) \end{bmatrix}^{T} \tag{3.35}$$

In the CR3BP, $\mathbf{x}(t)$ represents the state vector, i.e., P_3 with respect to the barycenter; in the N-body ephemeris model, $\mathbf{x}(t)$ reflects the state of P_i relative to P_k. From the initial time, the first-order equations of motion, $\dot{\mathbf{x}}(t) = \mathbf{f}(t, \mathbf{x}(t), \boldsymbol{\kappa})$, are propagated to some later time, $t_0 + T$, such that the spacecraft arrives at some point downstream at the state $\mathbf{x}(t_0 + T)$. By modifying the initial state values (position and/or velocity), the spacecraft arrives at an alternative downstream location. To determine an initial state such that the final state of the spacecraft is equal to some desired final position state, $\mathbf{x}_d$, a shooting scheme employs the update equation in Equation (3.33) or Equation (3.34). Note, in a single shooting approach, the design variable vector,

$\mathbf{X}$, includes initial state elements; then, the constraint equation, $\mathbf{F}(\mathbf{X})$, incorporates constraints to enforce some desired final state.

Since a simple targeter is a basic application for a corrections strategy, an example is useful. Figure 3.1 illustrates a targeting algorithm in which only the initial velocity is adjusted to reach some final desired position. For this example, the design variable

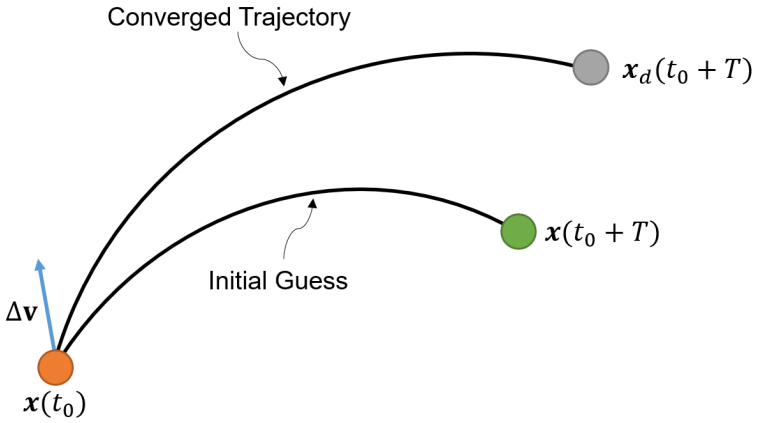

Figure 3.1. Single Shooter Corrections Algorithm Schematic

vector is comprised of the initial velocity components and the integration time along the segment. It can be written as

$$\mathbf{X} = \begin{bmatrix} \dot{x}(t_0) \\ \dot{y}(t_0) \\ \dot{z}(t_0) \\ T \end{bmatrix} \tag{3.36}$$

The constraint vector includes the constraints on the final position along the trajectory, i.e., the final position is equal to some desired position, and is expressed as

$$\mathbf{F}(\mathbf{X}) = \begin{bmatrix} x(t_0+T) - x_d \\ y(t_0+T) - y_d \\ z(t_0+T) - z_d \end{bmatrix} = \mathbf{0} \tag{3.37}$$

Therefore, the partials in the matrix $D\mathbf{F}(\mathbf{X})$ are

$$D\mathbf{F}(\mathbf{X}) = \begin{bmatrix} \frac{\partial x(t_0+T)}{\partial \dot{x}(t_0)} & \frac{\partial x(t_0+T)}{\partial \dot{y}(t_0)} & \frac{\partial x(t_0+T)}{\partial \dot{z}(t_0)} & \frac{\partial x(t_0+T)}{\partial T} \\ \frac{\partial y(t_0+T)}{\partial \dot{x}(t_0)} & \frac{\partial y(t_0+T)}{\partial \dot{y}(t_0)} & \frac{\partial y(t_0+T)}{\partial \dot{z}(t_0)} & \frac{\partial y(t_0+T)}{\partial T} \\ \frac{\partial z(t_0+T)}{\partial \dot{x}(t_0)} & \frac{\partial z(t_0+T)}{\partial \dot{y}(t_0)} & \frac{\partial z(t_0+T)}{\partial \dot{z}(t_0)} & \frac{\partial z(t_0+T)}{\partial T} \end{bmatrix} \tag{3.38}$$

Noting that some of the elements of $D\mathbf{F}(\mathbf{X})$ are, in fact, elements of the STM (where ϕ_{ij} is the (i, j) component of the STM), and others are velocity components, $D\mathbf{F}(\mathbf{X})$ is evaluated straightforwardly as

$$D\mathbf{F}(\mathbf{X}) = \begin{bmatrix} \phi_{14} & \phi_{15} & \phi_{16} & \dot{x}(t_0+T) \\ \phi_{24} & \phi_{25} & \phi_{26} & \dot{y}(t_0+T) \\ \phi_{34} & \phi_{35} & \phi_{36} & \dot{z}(t_0+T) \end{bmatrix} \tag{3.39}$$

In this example, since the integration time along the segment is a design variable, velocity components evaluated at the final time, $t_0 + T$, indicate the impact of time on the states at the final position. When integration time, T, is a free variable, the corrections scheme is denoted a variable-time shooting method. If the time along the segment is not allowed to vary, the shooting method is labeled fixed-time. Variable-time single shooting schemes are employed throughout this analysis, typically for corrections to a periodic orbit.

3.2.2 Multi-Segment Corrections Algorithm Formulation

In more complex design problems, or for longer integration times, a multi-segment corrections algorithm is better suited. A multiple shooting method simultaneously solves several two-point boundary value problems to meet design constraints. To formulate a multiple shooting procedure, a trajectory must be discretized into $(n-1)$ segments, or arcs, that are separated by n patchpoints, or nodes, as illustrated in Figure 3.2. Here, $\mathbf{x}_j^0$ refers to the full six-dimensional state corresponding to patch-

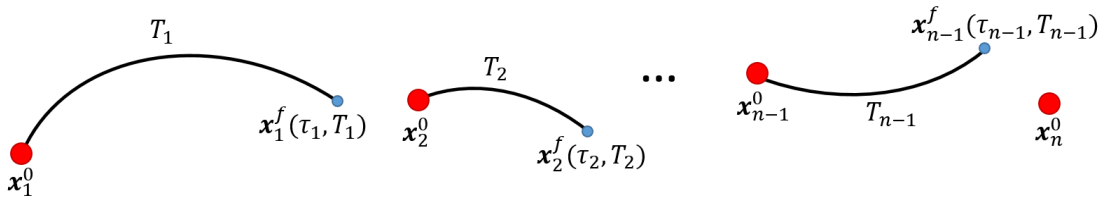

Figure 3.2. Multiple Shooter Corrections Algorithm Schematic

point j at the epoch time τ_j (where $\mathbf{x}_j^0$ is not a function of τ_j), and T_j refers to the integration time along segment j. The final state along a trajectory arc is written as $\mathbf{x}_j^f(\tau_j, T_j)$ and is a function of the initial epoch along the segment, τ_j, and the integration time, T_j. Note, the epoch is only required in the time-dependent N-body ephemeris model; in the CR3BP, the epoch is not incorporated since the system is autonomous. The initial guess for the six-dimensional state at the patchpoints and the resulting arcs do not necessarily yield a continuous path. Thus, continuity constraints, in the form $\mathbf{x}_{j-1}^f(\tau_{j-1}, T_{j-1}) - \mathbf{x}_j^0 = \mathbf{0}$, enforce full state continuity along the converged trajectory. In the non-autonomous ephemeris model, epoch continuity must also be enforced, i.e., the epoch date at the end of one arc must equal the epoch date at the beginning of the subsequent arc. As a note, if an impulsive maneuver is allowed at a patchpoint, position continuity is enforced, while velocity continuity is

omitted from the constraint vector. Any additional path constraints are applied at patchpoints.

As an example of a multi-segment corrections process, i.e., a multiple shooter, full state continuity is enforced over a trajectory in the N-body ephemeris model with n patchpoints. The free variable vector, in this example, includes the position and velocity states at all of the patchpoints, the time along each of the integrated segments, and the epoch times at the patchpoints, i.e.,

$$\mathbf{X} = \begin{bmatrix} \mathbf{x}_1^0 & \dots & \mathbf{x}_n^0 & T_1 & \dots & T_{n-1} & \tau_1 & \dots & \tau_n \end{bmatrix}^T \tag{3.40}$$

The constraint vector then includes state and epoch continuity constraints for each segment, i.e.,

$$\mathbf{F}(\mathbf{X}) = \begin{bmatrix} \mathbf{x}_1^f(\tau_1, T_1) - \mathbf{x}_2^0 \\ \vdots \\ \mathbf{x}_{n-1}^f(\tau_{n-1}, T_{n-1}) - \mathbf{x}_n^0 \\ \tau_1 + T_1 - \tau_2 \\ \vdots \\ \tau_{n-1} + T_{n-1} - \tau_n \end{bmatrix} = \mathbf{0} \tag{3.41}$$

Considering $\mathbf{X}$, and $\mathbf{F}(\mathbf{X})$, the Jacobian matrix, $D\mathbf{F}(\mathbf{X})$, is written as

$$D\mathbf{F}(\mathbf{X}) = \begin{bmatrix} \frac{\partial \mathbf{x}_1^f}{\partial \mathbf{x}_1^0} & -\frac{\partial \mathbf{x}_2^0}{\partial \mathbf{x}_2^0} & & & \frac{\partial \mathbf{x}_1^f}{\partial T_1} & & & \frac{\partial \mathbf{x}_1^f}{\partial \tau_1} & & & \\ & \ddots & \ddots & & & \ddots & & & \ddots & & \\ & & \frac{\partial \mathbf{x}_{\mathbf{n-1}}^{\mathbf{f}}}{\partial \mathbf{x}_{\mathbf{n-1}}^{\mathbf{0}}} & -\frac{\partial \mathbf{x}_n^0}{\partial \mathbf{x}_n^0} & & \frac{\partial \mathbf{x}_{n-1}^f}{\partial T_{n-1}} & & & \frac{\partial \mathbf{x}_{n-1}^f}{\partial \tau_{n-1}} & \\ & & & & \frac{\partial T_1}{\partial T_1} & & & \frac{\partial \tau_1}{\partial \tau_1} & -\frac{\partial \tau_2}{\partial \tau_2} & & \\ & & & & & \ddots & & & \ddots & \ddots & \\ & & & & & & \frac{\partial T_{n-1}}{\partial T_{n-1}} & & & \frac{\partial \tau_{n-1}}{\partial \tau_{n-1}} & -\frac{\partial \tau_n}{\partial \tau_n} \end{bmatrix} \tag{3.42}$$

By simplifying the partial derivatives and substituting STM elements where appropriate, Equation (3.42) is rewritten as

$$D\mathbf{F}(\mathbf{X}) = \begin{bmatrix} \mathbf{\Phi_1} & -\mathbf{I_{6\times 6}} & & & \dot{\mathbf{x}}_1^f & & & \frac{\partial \mathbf{x}_1^f}{\partial \tau_1} & & \\ & \ddots & \ddots & & & \ddots & & & \ddots & \\ & & \mathbf{\Phi_{n-1}} & -\mathbf{I_{6\times 6}} & & \dot{\mathbf{x}}_{n-1}^f & & & \frac{\partial \mathbf{x}_{n-1}^f}{\partial \tau_{n-1}} & \\ & & & & 1 & & 1 & -1 & & \\ & & & & & \ddots & & \ddots & \ddots & \\ & & & & & & 1 & & 1 & -1 \end{bmatrix} \tag{3.43}$$

where $\mathbf{\Phi_j}$ refers to the STM along segment j or $\mathbf{\Phi_j}(\tau_j + T_j, \tau_j)$, and $\frac{\partial \mathbf{x}_j^f}{\partial \tau_j}$ is the partial derivative for the final state along the j^{th} segment with respect to the epoch corresponding to the j^{th} patchpoint.

Partials with respect to epoch time, τ_j, and any constraints on epoch time are *only* applicable in the N-body ephemeris model. In the CR3BP, these partials and constraints are not applicable and are omitted from $\mathbf{F}(\mathbf{X})$ and $D\mathbf{F}(\mathbf{X})$. The design variables for a similar example in the CR3BP would include patchpoint states and segment integration times (in the case of a variable-time multiple shooter), while the constraints would simply enforce state continuity. Similar to the fixed-time single shooter, if times between patchpoints remain fixed, integration time does not appear in the design variable vector. A multiple shooting scheme is used throughout this investigation for converging trajectories that meet design constraints in both the CR3BP and in the N-body ephemeris model.

3.2.3 Additional Constraints

Additional constraints may be added along a trajectory to meet design requirements; adding the constraints on the patchpoint states is the most straightforward implementation. While there are many possible constraints, some useful types are described here. Typically, analytical partial derivatives in $D\mathbf{F}(\mathbf{X})$ are preferred, however, incorporating some types of constraints can be challenging due to the derivations for the required partial derivatives. As an alternative, a central differencing method or complex step differentiation can be employed to numerically approximate derivatives. Numerical methods are also useful in verification of the accuracy of analytical partial derivatives. Note that constraints formulated in the CR3BP are not always straightforward for a direct shift into the N-body ephemeris model (and vice versa) due to the problem formulation in different frames. Sample constraints are introduced below.

(i) Altitude

An altitude constraint supports, for example, a Low Earth Orbit (LEO) departure or a lunar flyby. To formulate an altitude constraint with respect to a primary body, within the context of the CR3BP, the position of the patchpoint with respect to the primary body is first determined. In the CR3BP, adjustment of the patchpoint state is required since the position state is defined with respect to the barycenter of the primary bodies. In the ephemeris model, the patchpoint position states are expressed with respect to a central body; if the central body is the body of interest, no manipulation is required.

In the case of an altitude constraint with respect to the Earth in the CR3BP Earth-Moon system, the $\mathbf{d}$ vector, or the nondimensional form of $\mathbf{r}_{13}$ from Equation (2.11), is used within the constraint formulation since a relative position of the spacecraft

with respect to Earth is necessary. The constraint on altitude with respect to the Earth is then formulated as

$$F(\mathbf{X}) = d^2 - (R_{Earth} + h)^2 = 0 \tag{3.44}$$

where $d^2 = (x + \mu)^2 + y^2 + z^2$ is the square of the distance between the spacecraft and the center of the Earth, R_{Earth} is the radius of the Earth, and h is the desired constraint altitude. Note that each term in Equation (3.44) is squared so that the magnitude of each term is effectively compared without the use of an absolute value operator (the absolute value function is not smooth, and is therefore not continuously differentiable). The required partial derivatives for this constraint are

$$\frac{\partial F(\mathbf{X})}{\partial x} = 2(x + \mu) \tag{3.45}$$

$$\frac{\partial F(\mathbf{X})}{\partial y} = 2y \tag{3.46}$$

$$\frac{\partial F(\mathbf{X})}{\partial z} = 2z \tag{3.47}$$

These partials are placed in the appropriate location in the $D\mathbf{F}(\mathbf{X})$ matrix. Use caution as the position vector corresponding to the patchpoint is nondimensional, so the constraint value for the altitude, $r_{Earth} + h$ must be nondimensional, as well. This constraint formulation is employed for departures from LEO and for lunar flybys.

(ii) Tangential Velocity

It may be useful to constrain the velocity vector corresponding to the state at a patchpoint to be aligned with a specified vector direction. For example, relevant applications include transfers into periodic orbits, where a tangential arrival or de-

parture equates to a lower cost, or an arbitrary maneuver along a trajectory that is constrained to be tangential. In the CR3BP, this constraint is formulated as

$$F(\mathbf{X}) = \begin{bmatrix} \dot{x} \\ \dot{y} \\ \dot{z} \end{bmatrix} \bullet \mathbf{v}_{tangent} - \sqrt{\dot{x}^2 + \dot{y}^2 + \dot{z}^2} = 0 \tag{3.48}$$

or

$$F(\mathbf{X}) = \dot{x}\dot{x}_{tangent} + \dot{y}\dot{y}_{tangent} + \dot{z}\dot{z}_{tangent} - \sqrt{\dot{x}^2 + \dot{y}^2 + \dot{z}^2} = 0 \tag{3.49}$$

where $\mathbf{v}_{tangent} = [\dot{x}_{tangent} \quad \dot{y}_{tangent} \quad \dot{z}_{tangent}]^T$ is a unit vector. This constraint evolves from the definition of a dot product as $\mathbf{a} \bullet \mathbf{b} = ab\cos(\beta)$ and when the vectors, $\mathbf{a}$ and $\mathbf{b}$ are tangential, β (the angle between the vectors) is zero and the definition reduces to $\mathbf{a} \bullet \mathbf{b} = ab$. The required partial derivatives to be placed in $D\mathbf{F}(\mathbf{X})$ are

$$\frac{\partial F(\mathbf{X})}{\partial \dot{x}} = \dot{x}_{tangent} - \frac{\dot{x}}{\sqrt{\dot{x}^2 + \dot{y}^2 + \dot{z}^2}} \tag{3.50}$$

$$\frac{\partial F(\mathbf{X})}{\partial \dot{y}} = \dot{y}_{tangent} - \frac{\dot{y}}{\sqrt{\dot{x}^2 + \dot{y}^2 + \dot{z}^2}} \tag{3.51}$$

$$\frac{\partial F(\mathbf{X})}{\partial \dot{z}} = \dot{z}_{tangent} - \frac{\dot{z}}{\sqrt{\dot{x}^2 + \dot{y}^2 + \dot{z}^2}} \tag{3.52}$$

This constraint is implemented for tangential arrivals and departures in support of various types of transfer trajectories.

(iii) Apsis

Constraining a node or patchpoint to an apse point is useful for a variety of scenarios. In this investigation, this constraint is typically implemented simultaneously

with an altitude constraint to force a specific flyby altitude of a primary at an apse location. The constraint, is formulated as

$$F(\mathbf{X}) = \begin{bmatrix} x \\ y \\ z \end{bmatrix} \bullet \begin{bmatrix} \dot{x} \\ \dot{y} \\ \dot{z} \end{bmatrix} = x\dot{x} + y\dot{y} = z\dot{z} = 0 \tag{3.53}$$

This constraint is again formulated from $\mathbf{a} \bullet \mathbf{b} = ab\cos(\beta)$. When the position and velocity vector corresponding to a particular patchpoint are perpendicular, e.g., at an apse, the dot product is equal to zero. The partial derivatives of this constraint with respect to the free variables are then straightforward, i.e.,

$$\frac{\partial F(\mathbf{X})}{\partial x} = \dot{x} \tag{3.54}$$

$$\frac{\partial F(\mathbf{X})}{\partial y} = \dot{y} \tag{3.55}$$

$$\frac{\partial F(\mathbf{X})}{\partial z} = \dot{z} \tag{3.56}$$

$$\frac{\partial F(\mathbf{X})}{\partial \dot{x}} = x \tag{3.57}$$

$$\frac{\partial F(\mathbf{X})}{\partial \dot{y}} = y \tag{3.58}$$

$$\frac{\partial F(\mathbf{X})}{\partial \dot{z}} = z \tag{3.59}$$

Typically, this constraint is employed to fix flyby conditions and, potentially, in conjunction with an altitude constraint.

(iv) Epoch

Epoch continuity is always enforced along trajectories in the N-body ephemeris model. The constraint is formulated as

$$F(\mathbf{X}) = \tau_{j-1} + T_{j-1} - \tau_j = 0 \tag{3.60}$$

Also a scalar, this epoch requirement constrains the last point along segment $j-1$ to possess the same epoch as the first point of segment j. The required partials are

$$\frac{\partial F(\mathbf{X})}{\partial \tau_{j-1}} = \frac{\mathbf{x}_{j-1}^f}{\partial \tau_{j-1}} \tag{3.61}$$

$$\frac{\partial F(\mathbf{X})}{\partial T_{j-1}} = -\frac{\mathbf{x}_{j-1}^f}{\partial T_{j-1}} = -\dot{\mathbf{x}}_{j-1}^f \tag{3.62}$$

$$\frac{\partial F(\mathbf{X})}{\partial \tau_j} = -\frac{\mathbf{x}_j^f}{\partial \tau_j} \tag{3.63}$$

Derivatives that represent the sensitivity of the final state along a segment to the epoch time, or $\frac{\partial \mathbf{x}_j^f}{\partial \tau_j}$ and $\frac{\mathbf{x}_{j-1}^f}{\partial \tau_{j-1}}$, are not straightforward. To construct the expressions, consider the first-order equations of motion for the N-body ephemeris model written to highlight some functional dependencies,

$$\dot{\mathbf{x}}(t) = \mathbf{f}\left(t, \mathbf{x}(t), \sum_{\substack{j=1 \\ j\neq i,k}}^{N} \boldsymbol{\zeta}_{kj}(\tau_j)\right) \tag{3.64}$$

where $\boldsymbol{\zeta}_{kj}(\tau_j)$ is the position vector of the perturbing body relative to the central body at a specified epoch time, τ_j. There is clearly a relationship between the final state along a segment and the epoch at the beginning of the same segment. Note

that a first-order differential equation governing the partial, $\frac{\partial \mathbf{x}(t)}{\partial \tau_j}$, can leverage the following

$$\frac{d}{dt}\left(\frac{\partial \mathbf{x}(t)}{\partial \tau_j}\right) = \frac{d}{d\tau_j}\left(\frac{\partial \mathbf{x}(t)}{\partial t}\right) \tag{3.65}$$

where the variables in the denominators can be swapped since t and τ_j are independent. Substituting Equation (3.64) into Equation (3.65) and employing the chain rule yields

$$\frac{d}{dt}\left(\frac{\partial \mathbf{x}(t)}{\partial \tau_j}\right) = \frac{d}{d\tau_j}\dot{\mathbf{x}} = \frac{d}{d\tau_j}\mathbf{f}\left(t, \mathbf{x}(t), \sum_{\substack{j=1 \\ j\neq i,k}}^{N} \boldsymbol{\zeta}_{kj}(\tau_j)\right) \tag{3.66}$$

which is equivalent to

$$\frac{d}{dt}\left(\frac{\partial \mathbf{x}(t)}{\partial \tau_j}\right) = \frac{\partial \mathbf{f}}{\partial \mathbf{x}(t)}\frac{d\mathbf{x}(t)}{d\tau_j} + \sum_{\substack{j=1 \\ j\neq i,k}}^{N} \frac{\partial \mathbf{f}}{\partial \boldsymbol{\zeta}_{kj}(\tau_j)}\frac{\partial \boldsymbol{\zeta}_{kj}(\tau_j)}{\partial \tau_j} \tag{3.67}$$

Noting that $\frac{\partial \mathbf{f}}{\partial \mathbf{x}(t)} = \mathbf{A}(t)$ and that $\frac{\partial \boldsymbol{\zeta}_{kj}(\tau_j)}{\partial \tau_j} = \frac{\partial \boldsymbol{\zeta}_{kj}(\tau_j)}{\partial t} = \dot{\boldsymbol{\zeta}}_{kj}(\tau_j)$ (the velocity of the perturbing body with respect to the central body at τ_j), Equation (3.67) reduces to

$$\frac{d}{dt}\left(\frac{\partial \mathbf{x}(t)}{\partial \tau_j}\right) = \mathbf{A}(t)\frac{d\mathbf{x}(t)}{d\tau_j} + \sum_{\substack{j=1 \\ j\neq i,k}}^{N} \frac{\partial \mathbf{f}}{\partial \boldsymbol{\zeta}_{kj}(\tau_j)}\dot{\boldsymbol{\zeta}}_{kj}(\tau_j) \tag{3.68}$$

The partial, $\frac{\partial \mathbf{f}}{\partial \boldsymbol{\zeta}_{kj}(\tau_j)}$, is determined using complex step differentiation, as demonstrated by Martins et al. [38] Equation (3.68) is then numerically integrated along with the STM and the equations of motion to evaluate $\frac{\partial \mathbf{x}(t)}{\partial \tau_j}$ which yields the partial derivatives $\frac{\partial \mathbf{x}_j^f}{\partial \tau_j}$ and $\frac{\mathbf{x}_{j-1}^f}{\partial \tau_{j-1}}$, evaluated at the final time along segments j and $(j-1)$, respectively (as used in Equations (3.61) and (3.63)). These partial derivatives support epoch continuity constraints. An epoch continuity constraint is necessary for every trajectory developed in the ephemeris model.

3.3 Coordinate Frames

An important aspect of multi-body trajectory design is the ability to transform state vectors between coordinate frames. Coordinate frame transformation allows trajectories to be viewed from various perspectives to gain insight into the design and to allow for solutions to be transitioned between models of various levels of fidelity, e.g., between the CR3BP and the N-body ephemeris model. The methodologies required to switch between the rotating frame and an arbitrary inertial frame, as well as the rotating frame and the primary-centered J2000 inertial frame, are detailed.

3.3.1 Coordinate Frame Transformation: Rotating Frame to Arbitrary Inertial Frame

To gain insight into a trajectory design concept constructed in the CR3BP, it is beneficial to view the solution in both the traditional rotating frame and in a general inertial frame, as defined in Figure 2.2. Recall that the rotating frame and an arbitrary inertial frame are assumed to be equivalent at time zero (arbitrarily defined in the autonomous CR3BP) and the orientation of the rotating frame with respect to the inertial frame is described simply by the angle $\theta = nt$, where n is the mean motion of the orbit of the primary bodies and t is the time elapsed since the frames were equivalent. Here, $\dot{\theta}$ is assumed constant due to the assumptions in the CR3BP. Both frames are centered at the barycenter of the primary system, and the rotating $\hat{z}$-axis is parallel to the orbital angular momentum and aligned with the inertially fixed $\hat{Z}$-axis. Since the $\hat{x}\hat{y}$-plane and the $\hat{X}\hat{Y}$-plane coincide for all time, a rotating

position vector is transformed to an inertial position vector with a simple rotation matrix:

$$\begin{bmatrix} x \\ y \\ z \end{bmatrix}_I = \begin{bmatrix} \cos\theta & -\sin\theta & 0 \\ \sin\theta & \cos\theta & 0 \\ 0 & 0 & 1 \end{bmatrix} \begin{bmatrix} x \\ y \\ z \end{bmatrix}_R \tag{3.69}$$

or

$$\begin{bmatrix} x \\ y \\ z \end{bmatrix}_I = {}^{\mathbf{I}}\mathbf{C}^{\mathbf{R}} \begin{bmatrix} x \\ y \\ z \end{bmatrix}_R \tag{3.70}$$

where the subscript R indicates a vector expressed in terms of rotating frame coordinates relative to a rotating observer and I denotes a vector expressed in inertial frame coordinates relative to an inertial observer. To compute the velocity with respect to an inertial observer in the rotating frame, the basic kinematic equation, from Equation (2.14), is used. Combining the relationship between the inertial and rotating frames in Equation (3.69) with the expression for the inertial velocity expressed in terms of rotating coordinates in Equation (2.16) yields an expression for the inertial velocity expressed in terms of inertial coordinates, i.e.,

$$\frac{{}^I d\boldsymbol{\rho}}{dt} = \dot{\boldsymbol{\rho}} = ((\dot{x} - ny)\cos\theta - (\dot{y} + nx)\sin\theta)\hat{X} + ((\dot{x} - ny)\sin\theta + (\dot{y} + nx)\cos\theta)\hat{Y} + \dot{z}\hat{Z} \tag{3.71}$$

Combining the simple rotation matrix in Equation (3.69) with Equation (3.71) and writing in matrix form, the total transformation matrix that relates a state with respect to a rotating observer expressed in rotating frame coordinates to a state with

respect to an arbitrary inertial observer expressed in inertial frame coordinates is then written as

$$\begin{bmatrix} x \\ y \\ z \\ \dot{x} \\ \dot{y} \\ \dot{z} \end{bmatrix}_I = \begin{bmatrix} \cos\theta & -\sin\theta & 0 & 0 & 0 & 0 \\ \sin\theta & \cos\theta & 0 & 0 & 0 & 0 \\ 0 & 0 & 1 & 0 & 0 & 0 \\ -n\sin\theta & -n\cos\theta & 0 & \cos\theta & -\sin\theta & 0 \\ n\cos\theta & -n\sin\theta & 0 & \sin\theta & -\cos\theta & 0 \\ 0 & 0 & 0 & 0 & 0 & 1 \end{bmatrix} \begin{bmatrix} x \\ y \\ z \\ \dot{x} \\ \dot{y} \\ \dot{z} \end{bmatrix}_R \tag{3.72}$$

or

$$\begin{bmatrix} x \\ y \\ z \\ \dot{x} \\ \dot{y} \\ \dot{z} \end{bmatrix}_I = \begin{bmatrix} {}^{\mathbf{I}}\mathbf{C}^{\mathbf{R}} & \mathbf{0} \\ n{}^{\mathbf{I}}\dot{\mathbf{C}}^{\mathbf{R}} & {}^{\mathbf{I}}\mathbf{C}^{\mathbf{R}} \end{bmatrix} \begin{bmatrix} x \\ y \\ z \\ \dot{x} \\ \dot{y} \\ \dot{z} \end{bmatrix}_R \tag{3.73}$$

The transformation matrix given in Equation (3.73) transforms a full six-dimensional state vector with respect to an rotating observer expressed in rotating coordinates, i.e., $\begin{bmatrix} x & y & z & \dot{x} & \dot{y} & \dot{z} \end{bmatrix}_R^T$, to a six-dimensional state vector with respect to an inertial observer expressed in terms of inertial coordinates, i.e., $\begin{bmatrix} x & y & z & \dot{x} & \dot{y} & \dot{z} \end{bmatrix}_I^T$.

Although state vectors are typically defined as originating at the barycenter in the rotating frame, other basepoints possess some advantages as well. For example, if a primary-centered inertial state is desired, a simple translation in the rotating frame from the barycenter of the primary bodies to the desired basepoint is a first step; then, the transformation matrix is applied to the translated vector. Additionally, to transform from an inertial state to a rotating state, the inverse of the transformation matrix is multiplied by the inertial state to yield the state as expressed in terms of the rotating coordinates.

As an overview, the steps to transform a six-dimensional state with respect to a rotating observer expressed in the rotating frame to a state with respect to an inertial observer expressed in the inertial frame are:

1. If desired, translate the rotating state that originates at the barycenter of the primaries such that its basepoint is at a different desired location
2. Apply the transformation matrix in Equation (3.73)

This methodology is applied throughout the analysis for transforming a rotating trajectory state into an arbitrary inertial frame to gain additional insight.

3.3.2 Coordinate Frame Transformation: Rotating Frame to J2000 Inertial Frame

Transitioning a state from the rotating frame to the J2000 inertial frame is similar to the procedure to transition a state from the rotating frame to an arbitrary inertial frame from Section 3.3.1, however, planetary ephemerides for a specific epoch date must be incorporated into the transformation. Since the barycenter is not fixed relative to either of the primaries in the N-body ephemeris model, this transformation is typically implemented with the basepoint at one of the primary bodies. To begin, a rotating position vector is translated such that the basepoint is at one of the primary bodies and is dimensionalized using instantaneous characteristic quantities $\tilde{t^*}$ and $\tilde{l^*}$, defined as

$$\tilde{l^*} = r_{12} \tag{3.74}$$

and

$$\tilde{t^*} = \frac{\tilde{l^*}^3}{\sqrt{\tilde{G}m_1 + \tilde{G}m_2}} \tag{3.75}$$

where $\mathbf{r_{12}}$ is the dimensional position vector of P_2 with respect to P_1, available from ephemeris data for a given epoch, $\tilde{G}$ is the dimensional gravitational constant, m_1 is the mass of P_1, and m_2 is the mass of P_2. The dimensional position vector in the rotating frame that originates at a primary, $\mathbf{r_p}$, is then defined as

$$\mathbf{r_p} = \begin{bmatrix} x_p \\ y_p \\ z_p \end{bmatrix}_{\tilde{R}} \tag{3.76}$$

where the subscript p denotes values centered at a primary body and the subscript $\tilde{R}$ indicates that the vector is expressed in rotating frame coordinates. Next, an instantaneous, primary-centered rotating frame is constructed using ephemeris data. This instantaneous frame is defined in terms of unit vectors parallel to axes in the J2000 inertial frame. The corresponding axes are defined as

$$\hat{\hat{x}} = \frac{\mathbf{r_{12}}}{\tilde{l}^*} \tag{3.77}$$

$$\hat{\hat{z}} = \frac{\mathbf{r_{12}} \times \mathbf{v_{12}}}{|\mathbf{r_{12}} \times \mathbf{v_{12}}|} \tag{3.78}$$

$$\hat{\hat{y}} = \hat{\hat{z}} \times \hat{\hat{x}} \tag{3.79}$$

A rotation matrix is defined using these instantaneous rotating axes as

$$^{\mathbf{I}}\mathbf{C}^{\tilde{\mathbf{R}}} = \begin{bmatrix} \hat{\hat{x}} & \hat{\hat{y}} & \hat{\hat{z}} \end{bmatrix} = \begin{bmatrix} C_{11} & C_{12} & C_{13} \\ C_{21} & C_{22} & C_{23} \\ C_{31} & C_{32} & C_{33} \end{bmatrix} \tag{3.80}$$

where $\hat{\hat{x}}$, $\hat{\hat{y}}$, and $\hat{\hat{z}}$ are column unit vectors. Using this instantaneous rotation matrix, a primary-centered dimensional position vector expressed in the rotating frame can

be transformed to a primary-centered dimensional position vector that is expressed in terms of the J2000 inertial coordinates, i.e.,

$$\begin{bmatrix} x_p \\ y_p \\ z_p \end{bmatrix}_I = {}^{\mathbf{I}}\mathbf{C}^{\tilde{\mathbf{R}}} \begin{bmatrix} x_p \\ y_p \\ z_p \end{bmatrix}_{\tilde{R}} \tag{3.81}$$

Since the mean motion of the primaries and, therefore, the angular velocity of the rotating frame with respect to the inertial frame, is no longer constant in the N-body ephemeris model, the instantaneous angular velocity ${}^{\boldsymbol{I}}\boldsymbol{\omega}^{\tilde{\boldsymbol{R}}} = \dot{\tilde{\theta}}\hat{\tilde{z}}$ must be computed as well. The instantaneous angular velocity is evaluated by using the two-body problem definition, i.e.,

$$\dot{\tilde{\theta}} = \frac{|\mathbf{r_{12}} \times \mathbf{v_{12}}|}{r_{12}^2} \tag{3.82}$$

with units of rad/sec. To construct the velocity relative to an observer in the J2000 inertial frame, but expressed in terms of rotating frame coordinates, the basic kinematic equation, from Equation (2.14) is leveraged. Recall the kinematic relationship,

$$\frac{{}^{I}d\boldsymbol{r_p}}{dt} = \frac{{}^{R}d\boldsymbol{r_p}}{dt} + {}^{\boldsymbol{I}}\boldsymbol{\omega}^{\tilde{\boldsymbol{R}}} \times \boldsymbol{r_p} \tag{3.83}$$

that yields

$$\frac{{}^{I}d\boldsymbol{r_p}}{dt} = (\dot{x}_p - \dot{\tilde{\theta}}y_p)\hat{\tilde{x}} + (\dot{y}_p + \dot{\tilde{\theta}}x_p)\hat{\tilde{y}} + \dot{z}_p\hat{\tilde{z}} \tag{3.84}$$

Equation (3.84) is combined with Equation (3.81) to produce an expression for the instantaneous inertial velocity expressed in inertial coordinates, i.e.,

$$\begin{aligned} \frac{{}^{I}d\boldsymbol{r_p}}{dt} = {} & ((\dot{x}_p - \dot{\tilde{\theta}}y_p)C_{11} + (\dot{y}_p + \dot{\tilde{\theta}}x_p)C_{12} + \dot{z}_pC_{13})\hat{X} \\ & + ((\dot{x}_p - \dot{\tilde{\theta}}y_p)C_{21} + (\dot{y}_p + \dot{\tilde{\theta}}x_p)C_{22} + \dot{z}_pC_{23})\hat{Y} \\ & + ((\dot{x}_p - \dot{\tilde{\theta}}y_p)C_{31} + (\dot{y}_p + \dot{\tilde{\theta}}x_p)C_{32} + \dot{z}_pC_{33})\hat{Z} \end{aligned} \tag{3.85}$$

Finally, the total transformation matrix that relates the six-dimensional state given in rotating frame coordinates with respect to a rotating observer to the state expressed in J2000 inertial coordinates with respect to an observer in the J2000 inertial frame, produced by combining Equations (3.85) and (3.81) is given as

$$\begin{bmatrix} x \\ y \\ z \\ \dot{x} \\ \dot{y} \\ \dot{z} \end{bmatrix}_I = \begin{bmatrix} C_{11} & C_{12} & C_{13} & 0 & 0 & 0 \\ C_{21} & C_{22} & C_{23} & 0 & 0 & 0 \\ C_{31} & C_{32} & C_{33} & 0 & 0 & 0 \\ \dot{\tilde{\theta}}C_{12} & -\dot{\tilde{\theta}}C_{11} & 0 & C_{11} & C_{12} & C_{13} \\ \dot{\tilde{\theta}}C_{22} & -\dot{\tilde{\theta}}C_{21} & 0 & C_{21} & C_{22} & C_{23} \\ \dot{\tilde{\theta}}C_{32} & -\dot{\tilde{\theta}}C_{31} & 0 & C_{31} & C_{32} & C_{33} \end{bmatrix} \begin{bmatrix} x \\ y \\ z \\ \dot{x} \\ \dot{y} \\ \dot{z} \end{bmatrix}_{\tilde{R}} \tag{3.86}$$

As previously stated, the rotating position and velocity state *must* first be dimensionalized before a transformation into the J2000 inertial frame using Equation (3.86) since the 6×6 transformation matrix includes dimensional elements in the lower left quadrant. Additionally, note that to transform a state relative to an observer in the J2000 inertial frame expressed in inertial frame coordinates to a state relative to a rotating observer expressed in rotating frame coordinates, the inverse of the transformation matrix in Equation (3.86) is applied.

As it is beneficial to integrate the N-body equations of motion using nondimensional quantities due to numerical challenges, the dimensional states in the J2000 inertial frame resulting from the application of Equation (3.86) must be nondimensionalized as a final step in the transformation process from a state relative to a rotating observer expressed in rotating coordinates to a state relative to a J2000 inertial frame observer expressed in inertial coordinates. Typically, the standard characteristic quantities from the CR3BP are used to nondimensionalize the resulting state, $\begin{bmatrix} x & y & z & \dot{x} & \dot{y} & \dot{z} \end{bmatrix}_I^T$, which is defined as relative to an observer in the J2000 inertial frame and is expressed in inertial coordinates. As an overview, the steps to transform a state relative to a rotating observer that is expressed in the rotating frame to a

state relative to an observer in the J2000 inertial frame that is expressed in the J2000 inertial frame are:

1. Translate the rotating state that has a basepoint at the barycenter of the primaries such that its basepoint is located at the center of a primary
2. Dimensionalize the translated primary-centered rotating state with the instantaneous characteristic quantities
3. Apply the transformation matrix given in Equation (3.86)
4. Nondimensionalize the primary-centered J2000 inertial state using the characteristic quantities from the CR3BP

This methodology is used throughout the analysis for transforming a rotating frame trajectory solution (states expressed in rotating frame coordinates relative to a rotating observer) into states expressed in the J2000 inertial frame relative to an observer in the J2000 inertial frame in order to gain additional insight and to prepare for transitioning a state from the CR3BP to the higher-fidelity N-body ephemeris model.

4. TRAJECTORY CONSTRUCTION: CR3BP AND THE EPHEMERIS MODEL

Periodic orbits are employed in a variety of trajectory design and mission applications and are particularly useful for mission concepts in which a repeating predictable behavior is desired, for example, a long-duration lunar orbiter or a deep-space telescope. Precisely periodic motion exists in the CR3BP about the primaries and in the vicinity of the Lagrange points. However, similarly repeating behaviors emerge in the higher-fidelity ephemeris model, as well. Periodic orbits are generally straightforward to compute in the CR3BP using either a single or multiple shooting scheme. Given trajectory arcs in the CR3BP, including periodic orbits, a process to transition representative states into the N-body ephemeris model yields an initial guess for trajectory construction and analysis in such a higher-fidelity model.

4.1 Periodic Orbit Computation in the CR3BP

A simple type of periodic motion appears in the form of symmetric orbits in the CR3BP. Although other types of non-symmetric periodic motion exist, xz-symmetric orbits are the primary focus in this investigation and, therefore, a strategy to numerically compute this type of periodic motion is introduced. Any numerical corrections algorithm requires a reasonable starting point or guess. An initial guess for trajectory arcs in the CR3BP can originate from a variety of sources. For periodic solutions near libration points, a linear approximation of the behavior serves as a straightforward initial guess for the true motion. [12] Periodic behavior about the primary bodies is resonably approximated as a two-body Keplerian solution. As a third option, initial

guesses also originate from previously converged solutions. Given an initial guess, the corrections process in the CR3BP proceeds.

Due to symmetry, a single shooting algorithm serves as the basis for a simple and efficient corrections process to compute symmetric periodic trajectories. Solutions are constructed by constraining the departure and arrival condition at the xz-plane crossing to be perpendicular. To illustrate the process, a state on the xz-plane is selected, i.e., $y_0 = 0$, were the subscript 0 represents the initial state. Additionally, to ensure a periodic departure from the xz-plane, $\dot{x}_0 = \dot{z}_0 = 0$. The initial condition vector is, therefore, of the form

$$\mathbf{x}_0 = \begin{bmatrix} x_0 & 0 & z_0 & 0 & \dot{y}_0 & 0 \end{bmatrix}^T \tag{4.1}$$

Maintaining an initial condition of the form in Equation (4.1), the free-variable vector is written as

$$\mathbf{X} = \begin{bmatrix} x_0 \\ z_0 \\ \dot{y}_0 \\ T \end{bmatrix} \tag{4.2}$$

where T, the integration time, is included to implement a variable-time shooting algorithm. Note that omitting any of the states in the free-variable vector essentially forces the missing variable to remain equal to the value assumed in the initial guess, $\mathbf{x}_0$. The constraints on the state variables used to enforce a downstream perpendicular xz-plane crossing are then defined as

$$\mathbf{F}(\mathbf{X}) = \begin{bmatrix} y(T) \\ \dot{x}(T) \\ \dot{z}(T) \end{bmatrix} = \mathbf{0} \tag{4.3}$$

Then, it follows that the $D\mathbf{F}(\mathbf{X})$ matrix is expressed as

$$D\mathbf{F}(\mathbf{X}) = \begin{bmatrix} \phi_{21} & \phi_{23} & \phi_{25} & \dot{y}(T) \\ \phi_{41} & \phi_{43} & \phi_{45} & \ddot{x}(T) \\ \phi_{61} & \phi_{63} & \phi_{65} & \ddot{z}(T) \end{bmatrix} \tag{4.4}$$

where ϕ_{ij} are elements of the STM, $\Phi(T, 0)$, and the elements in the last column are evaluated at the final time. Since the number of free-variables is greater than the number of constraints in this formulation, a minimum norm process is used to iterate on the initial condition until the constraints are met to within some tolerance, resulting in a half revolution along a periodic orbit. Recall, a minimum norm strategy is employed since it delivers a final solution that maintains the geometry of the initial guess. Integrating the converged initial state for $2T$ yields the periodic orbit.

This process can also be applied to the planar case by setting $z_0 = 0$ in the initial condition vector and omitting z_0 from the free-variable vector. For the planar case, the free-variable vector, $\mathbf{X}$, is defined as

$$\mathbf{X} = \begin{bmatrix} x_0 \\ \dot{y}_0 \\ T \end{bmatrix} \tag{4.5}$$

Then, the constraint vector becomes

$$\mathbf{F}(\mathbf{X}) = \begin{bmatrix} y(T) \\ \dot{x}(T) \end{bmatrix} = \mathbf{0} \tag{4.6}$$

where $\dot{z} = 0$ is omitted because the motion naturally remains in the plane of primary motion due to the form of the initial conditions. It follows that the $D\mathbf{F}(\mathbf{X})$ matrix is written as

$$D\mathbf{F}(\mathbf{X}) = \begin{bmatrix} \phi_{21} & \phi_{25} & \dot{y}(T) \\ \phi_{41} & \phi_{45} & \ddot{x}(T) \end{bmatrix} \tag{4.7}$$

In this investigation, the single shooting strategy is used to compute a variety of periodic orbits in both the planar and three-dimensional cases. Examples of such applications are insightful.

Planar Application: Construction of a Distant Retrograde Orbit

The family of Distant Retrograde Orbits (DROs) are a generally stable family of planar orbits that encompass the smaller primary. When viewed from the direction of the positive $\hat{z}$ axis in the rotating frame, a spacecraft in a DRO appears to move clockwise, hence the orbits are denoted as retrograde. The DROs are desirable orbits in cislunar space due to the low sensitivity to perturbations over each revolution. The DRO family is not a new discovery; this family of orbits has been examined by various authors since the 1960s. For example, in 1968, Broucke intoduced the DROs as a group of planar periodic retrograde orbits about the Moon, which he donoted as family "C." [39] Notable work by Hénon during the same time frame contributed to the dynamical understanding of the DROs within the context of the Hill problem; these orbits were denoted by Hénon as family "f." [40]

To compute a distant retrograde orbit, a two-body approximation for a circular orbit about the Moon supplies a good initial guess. For a orbital radius of 9000 km (0.023413 nondimensional units), the circular orbital velocity, based on Keplerian motion is 0.738231 km/s (0.720544 nondimensional units). An initial guess for an initial state along the orbit, in terms of nondimensional units, is then

$$\mathbf{x}_0^0 = \begin{bmatrix} ((1-\mu) - 0.023413) & 0 & 0 & 0 & 0.720544 & 0 \end{bmatrix}^T \tag{4.8}$$

with an initial estimate for the integration time equal to half the period of a circular Keplerian orbit, that is, 10.639 minutes (0.102081 nondimensional units). Note that, since the Moon is located at the nondimensional coordinate $((1-\mu), 0, 0)$ in the

CR3BP rotating frame, the value for x_0 is shifted from the barycenter to provide an initial x-coordinate relative to the Moon. This shift is accomplished by subtracting the desired orbital radius, 0.023413 nondimensional units, from $(1-\mu)$ to supply a value for x_0 that is on the near side of the Moon relative to the Earth in the CR3BP rotating frame. As a vehicle in a DRO moves in a clockwise direction about the Moon as viewed from the positive $\hat{z}$ axis, an initial condition on the near side of the Moon relative to the Earth indicates that the y-velocity at the initial time must be positive. In this example, the x-coordinate is omitted from the free-variable vector, thereby forcing the x-coordinate to remain equivalent to the value assigned in $\mathbf{x}_0^0$. Using a single shooting strategy, a periodic DRO is constructed. The final converged initial condition is

$$\mathbf{x}_0^* = \begin{bmatrix} ((1-\mu) - 0.023413) & 0 & 0 & 0 & 0.744742 & 0 \end{bmatrix}^T \tag{4.9}$$

The half-period of the resulting DRO is 0.0991386 nondimensional units or 10.332 hours. The value for the orbital speed at the initial time, $\dot{y}_0$, is equivalent to 0.763023 km/s. Since the initial guess, determined from a Keplerian orbit about the Moon, is close to the true motion, the algorithm converged in just a few iterations. The resulting DRO is plotted in the rotating frame in Figure 4.1. In this example, the update to the free-variable vector is multiplied by an attenuation factor equal to $\frac{1}{2}$ to aid in convergence, i.e., the update equation is now

$$\mathbf{X^{j+1}} = \mathbf{X^j} - \frac{1}{2} D\mathbf{F}(\mathbf{X^j})^{-1}\mathbf{F}(\mathbf{X^j}) \tag{4.10}$$

Differential corrections algorithms are known to be sensitive near the primary bodies, i.e., small changes in an initial condition can result in large changes in the propagated trajectory. Reducing the size of the update to the initial condition vector by using an attenuation factor aids in preventing divergence.

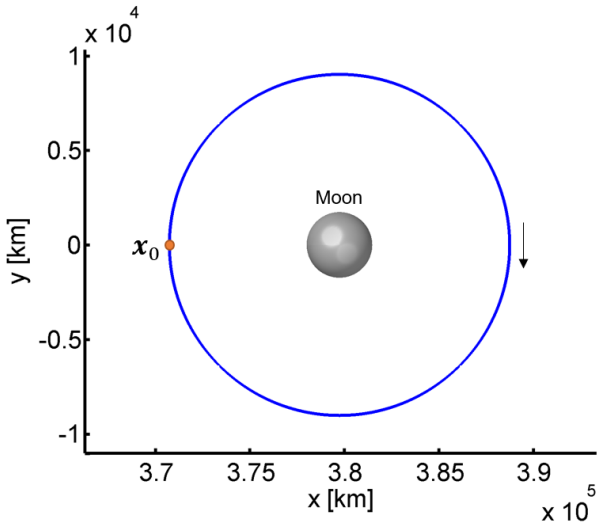

Figure 4.1. A distant retrograde orbit about the Moon in the Earth-Moon rotating frame, computed using a single shooting algorithm.

Three-Dimensional Application: Construction of a Halo Orbit in the Vicinity of Earth-Moon L_2

In 1968, Farquhar first formulated the concept of a "halo" orbit to describe a three-dimensional periodic orbit that was not obscured by the Moon as viewed from Earth. [8] Later work by Breakwell and Brown allowed for the continuation of the L_2 halo family and the computation of the L_1 halo family from the planar bifurcating Lyapunov orbit near the respective Lagrange point to the near-vicinity of the Moon. [6] Howell worked to extend these families of orbits, along with the L_3 halo family, to other systems [9] and to the stable 'near-rectilinear' range close to the nearer primary. [7]

In the Earth-Moon gravitational regime, a critical element in constructing three-dimensional halo orbits is the initial guess for the state vector. An initial guess for an L_2 halo orbit is available from many previous authors. In this investigation, an initial

guess for a northern L_2 halo orbit is obtained from Grebow. [24] The corresponding initial guess for a southern L_2 halo orbit is constructed by reflecting the initial condition for the corresponding northern L_2 halo orbit across the xy-plane, i.e., an initial guess for a southern L_2 halo orbit is

$$\mathbf{x_0^0} = \begin{bmatrix} 1.1503 & 0 & -0.1459 & 0 & -0.2180 & 0 \end{bmatrix}^T \tag{4.11}$$

An estimate for the half-period of this particular halo orbit is 1.5980 nondimensional units or 6.9393 days. Using a single shooting algorithm, the initial condition is updated in an iterative procedure. The converged solution is equivalent to that in Equation (4.11) to four significant digits and the half-period of the resulting periodic halo orbit is 1.5979 nondimensional units or 6.9391 days. The process converges in just two iterations and the converged halo orbit is plotted in Figure 4.2.

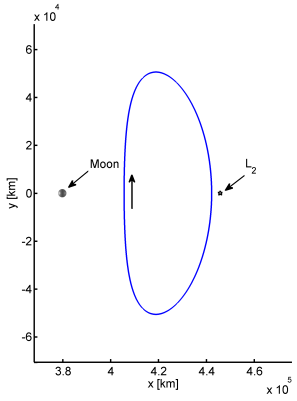

(a) An L_2 southern halo orbit projected into the xy-plane.

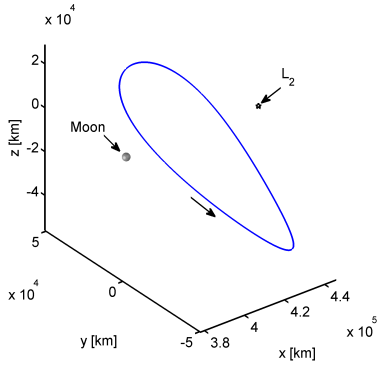

(b) An L_2 southern halo orbit in three-dimensional configuration space

Figure 4.2. An L_2 southern halo orbit computed using a single shooting method.

4.1.1 Continuation of an Orbit Family

Single shooting and multiple shooting schemes are employed to compute a single point solution for a trajectory based on one given set of initial conditions. In general, it is useful to construct a range of related solutions, or a family, if possible. Families of orbits deliver insight into the dynamical characteristics across an entire region and offer various options for trajectory design. Additionally, since a family of orbits spans a range of characteristics, an individual orbit, or family member, is then able to be selected more carefully to meet mission requirements. Multiple strategies to compute families of orbits exist; for example, a natural parameter continuation scheme offers a straightforward approach to compute a family member based on a previously converged solution. Additionally, a strategy that requires less intuition and a broader range of applications, the pseudo-arclength continuation scheme, is also an option.

Natural Parameter Continuation

Natural parameter continuation offers a simple strategy to construct a family of related solutions. To begin, a single converged solution is determined by implementing a numerical corrections process given some initial guess. For example, as described previously, a single shooting easily delivers a periodic orbit. Then, one parameter associated with the converged solution is varied, or incremented by a small, but specified, amount. (This parameter typically possesses some physical significance, e.g., x_0, y_0, z_0, Jacobi constant, or time of flight, among many other possibilities.) The previously converged solution, now with one varied parameter, is then employed as an initial guess for a new trajectory in a differential corrections scheme. Once converged, the new trajectory maintains some characteristics of the previous trajectory, however, the solutions are independent but related across values of the varied parameter. The natural parameter continuation process is then be repeated to construct additional

related trajectories. This continuation scheme applies to both periodic orbits and non-periodic trajectory arcs.

As an example, a continuation scheme with increments in x_0 is detailed for some arbitrary planar periodic orbit. The process proceeds as follows:

1. Using a corrections scheme, converge on some planar periodic orbit with initial conditions $\mathbf{x}^*_{\mathbf{0,j}} = \begin{bmatrix} x_{0,j} & 0 & 0 & 0 & \dot{y}_{0,j} & 0 \end{bmatrix}^T$ and period P_j. Here, the superscript * on a vector quantity refers to a converged solution; no superscript implies an initial guess.

2. Increment x_0 by some small step, β, resulting in an initial guess for a nearby family member, $\mathbf{x_{0,j+1}} = \begin{bmatrix} (x_{0,j} + \beta) & 0 & 0 & 0 & \dot{y}_{0,j} & 0 \end{bmatrix}^T$ with period P_j. Note, a typical value for β is ± 0.0001 nondimensional units (which corresponds to 38.4 km if the increment is in position), depending on the sensitivity in the region.

3. Use $\mathbf{x_{0,j+1}}$ as a guess in a differential corrections scheme to converge on a solution nearby $\mathbf{x}^*_{\mathbf{0,j}}$. Note that the initial x-coordinate must not be included as a free-variable; otherwise, the solution is likely to re-converge onto $\mathbf{x}^*_{\mathbf{0,j}}$.

4. The corrections process converges on the nearby solution, or family member, with converged initial conditions $\mathbf{x}^*_{\mathbf{0,j+1}} = \begin{bmatrix} (x_{0,j} + \beta) & 0 & 0 & 0 & \dot{y}_{0,j+1} & 0 \end{bmatrix}^T$ and period P_{j+1}.

5. The process is repeated to continue the family.

Some of the challenges associated with natural parameter continuation arise from the typically physical significance of the parameter that governs the continuation scheme, thus, some intuition is required concerning the likely evolution of the family of solutions. But, within one family of solutions, the varied parameter is not always the same one. Additionally, complications arise due to the sensitivity of the solution;

the appropriate size for the parameter increment β is not always apparent. Although natural parameter continuation is insightful and straightforward to implement, it is challenging for some applications and alternatives may be necessary.

Pseudo-Arclength Continuation

An alternative continuation scheme is offered by the pseudo-arclength method. [41,42] Pseudo-arclength differs from natural parameter continuation the selection of the increment quantity to advance to the next solution in the family. The increment, or step size, Δs, in the pseudo-arclength continuation strategy is defined in a direction tangent to the family. All free-variables are then updated simultaneously. By stepping in a tangent direction, prior knowledge of the evolution in the solution space is not necessary. Additionally, larger increments are possible and, in many applications in the CR3BP, fewer iterations are required for convergence. However, in this continuation scheme, the step size, Δs, is not an intuitive physical parameter which leads to less insight into the relative distance between solutions.

Leveraging many capabilities of natural parameter continuation, the algorithm for pseudo-arclength continuation is focused on some key modifications. In any continuation scheme, a new member of the family is computed based on a previous solution. A previously converged solution is defined by a free-variable vector denoted $\mathbf{X}_\mathbf{j}^*$, where $\mathbf{F}(\mathbf{X}_\mathbf{j}^*) = \mathbf{0}$; the free-variable vector denoted as $\mathbf{X}_{\mathbf{j+1}}^{\mathbf{0}}$ represents the initial guess for the next family member that may not yet meet the constraints. Given $\mathbf{X}_\mathbf{j}^*$, a unit vector tangent to the family at $\mathbf{X}_\mathbf{j}^*$ is constructed from the null vector, denoted $\Delta\mathbf{X}_\mathbf{j}^*$, of the Jacobian matrix, $D\mathbf{F}(\mathbf{X}_\mathbf{j}^*)$. The null vector of $D\mathbf{F}(\mathbf{X}_\mathbf{j}^*)$ is selected since adding a multiple of the null space vector does not change the solution to the first-order iterative update equation given in Equation (3.31), $\mathbf{F}(\mathbf{X}) = \mathbf{F}(\mathbf{X}^0) + D\mathbf{F}(\mathbf{X}^0)\,(\mathbf{X} - \mathbf{X}^0)$. To ensure that the next solution, $\mathbf{X}_{\mathbf{j+1}}$, is shifted by the scalar step Δs along the

family tangent vector, an additional constraint is added to the original constraint vector, $\mathbf{F}(\mathbf{X_{j+1}})$. This pseudo-arclength constraint is a scalar expressed as

$$(\mathbf{X_{j+1}} - \mathbf{X_j^*})^T \Delta \mathbf{X_j^*} - \Delta s = 0 \tag{4.12}$$

The augmented constraint vector is then

$$\mathbf{G}(\mathbf{X_{j+1}}) = \begin{bmatrix} \mathbf{F}(\mathbf{X_{j+1}}) \\ (\mathbf{X_{j+1}} - \mathbf{X_j^*})^T \Delta \mathbf{X_j^*} - \Delta s \end{bmatrix} = \mathbf{0} \tag{4.13}$$

The derivative of the augmented constraint vector, $\mathbf{G}(\mathbf{X_{j+1}})$ with respect to the free-variables, $\mathbf{X_{j+1}}$, yields an augmented Jacobian matrix, as well, given by

$$D\mathbf{G}(\mathbf{X_{j+1}}) = \frac{\partial \mathbf{G}(\mathbf{X_{j+1}})}{\partial \mathbf{X_{j+1}}} = \begin{bmatrix} D\mathbf{F}(\mathbf{X_{j+1}}) \\ \Delta \mathbf{X_j^{*T}} \end{bmatrix} \tag{4.14}$$

Once the augmented constraint vector and the Jacobian matrix are constructed, an iterative Newton's method is employed to converge on the next family member, $\mathbf{X_{j+1}^*}$.

While the members of many families of periodic orbits are generated using natural parameter continuation, pseudo-arclength continuation is a valuable option. For the specific families in this investigation, pseudo-arclength continuation reduces the computational time and no *a priori* knowledge of the evolution of the family is necessary. Multiple families of periodic orbits are generated to demonstrate the pseduo-arclength strategy.

4.1.2 Examples of Periodic Orbit Families

The distant retrograde orbits, the period-3 distant retrograde orbits, and the L_1 and L_2 halo families are computed using a pseudo-arclength continuation method. These families of orbits are periodic and symmetric across the xz-plane. Nondimen-

sional initial conditions, converged using the nondimensional constants in Table 2.1, for a select number of family members are included for completeness along with the orbital period and value of Jacobi constant for each orbit. The given initial conditions can be used within a corrections process to generate these specific family members, or used to initiate a continuation process.

Distant Retrograde Orbits

The distant retrograde orbits are a planar periodic family of orbits surrounding the smaller primary. These orbits were previously introduced as the example of a planar correction process. A representative set of orbits from the DRO family are plotted in Figure 4.3; the orbits are colored by the value of Jacobi constant. Initial conditions for these orbits in the Earth-Moon system are summarized in Table 4.1 along with the value of the Jacobi constant and orbital period for each orbit. Since the initial conditions for a planar periodic orbit are of the form $\mathbf{x}_0 = \begin{bmatrix} x_0 & 0 & 0 & 0 & \dot{y}_0 & 0 \end{bmatrix}^T$, values for x_0 and y_0 are included in the table. The initial conditions provided are converged using the nondimensional constants in Table 2.1, however, as a limited number of significant digits are included, a corrections scheme may be necessary to ensure precisely periodic motion when employing these conditions to find a periodic solution or within a continuation process. The values in Table 4.1 are nondimensionalized and serve as a good initial guess for each DRO family member. Observe that the Jacobi constant value and the orbital period do not increase linearly as the family members increase in size. The nonlinear relationship between these characteristics and perilune radius appear in Figure 4.4. The value for the Jacobi constant does monotonically decreases as perilune radius increases; the opposite is true for orbital period, i.e., the orbital period increases with increasing perilune radius.

Table 4.1. Initial Conditions for the Distant Retrograde Orbits

JC	**Period**	$\mathbf{x_0}$	$\mathbf{\dot{y}_0}$
3.3949	0.2230147974	0.9624690577	0.7184165432
3.1361	0.6166055596	0.9361690577	0.5420829797
3.0460	1.0873149322	0.9098690577	0.4861304073
2.9982	1.6036604892	0.8835690577	0.4704001643
2.9676	2.1456222060	0.8572690577	0.4752341941
2.9455	2.6935872117	0.8309690577	0.4931694567
2.9278	3.2259140152	0.8046690577	0.5206492176
2.9123	3.7214359005	0.7783690577	0.5556648548
2.8976	4.1639236713	0.7520690577	0.5969085865
2.8828	4.5451073473	0.7257690577	0.6434438745
2.8674	4.8656732383	0.6993690577	0.6947808121
2.8510	5.1282795896	0.6730690577	0.7500292555
2.8334	5.3419826389	0.6467690577	0.8090396816
2.8145	5.5150452938	0.6204690577	0.8716174367
2.7940	5.6550946637	0.5941690577	0.9376894311
2.7720	5.7686517772	0.5678690577	1.0072891703
2.7482	5.8610608744	0.5415690577	1.0805472211
2.7227	5.9366010546	0.5152690577	1.1576874834
2.6952	5.9986577916	0.4889690577	1.2390293886
2.6655	6.0500729893	0.4625690577	1.3253326531

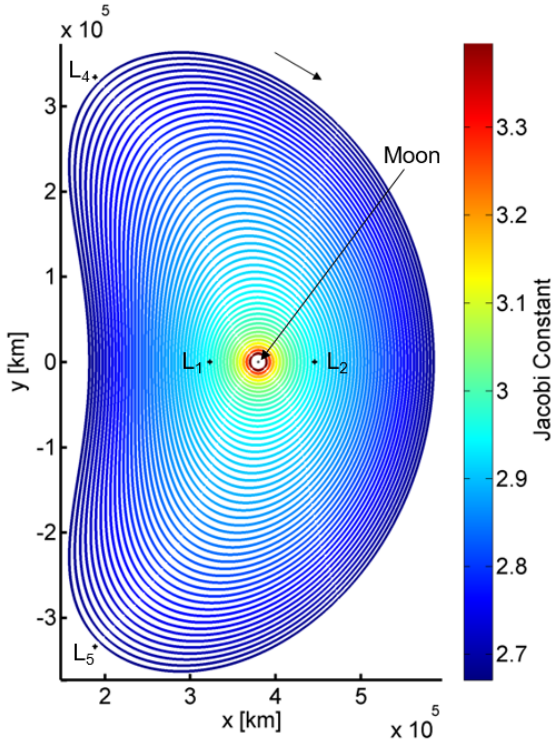

Figure 4.3. Family of distant retrograde orbits about the Moon computed in the Earth-Moon system, colored by Jacobi constant value.

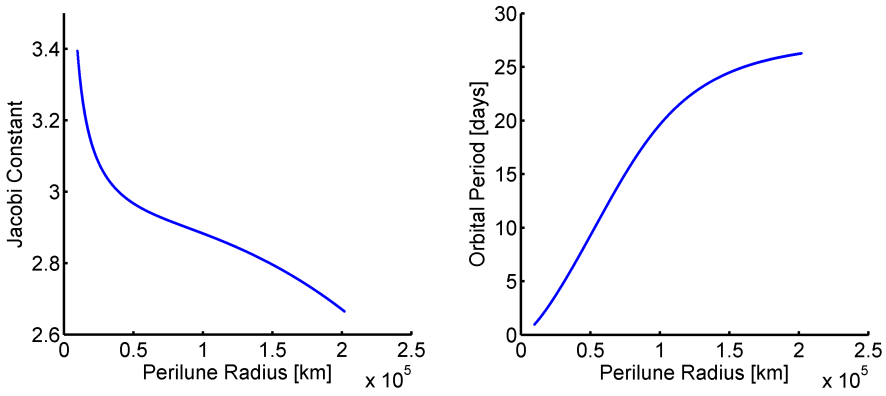

Figure 4.4. Jacobi constant value and orbital period as a function of perilune radius over a range of periodic orbits in the distant retrograde orbit family in the Earth-Moon system.

Period-3 Distant Retrograde Orbits

The Period-3 Distant Retrograde Orbits (P3DRO) are a family of planar periodic orbits that are related to the DROs. In fact, the P3DRO family bifurcates from the DROs at a period-tripling bifurcation. A period tripling bifurcation is evident when a pair of eigenvalues from the monodromy matrix are equivalent to the complex solutions of $\sqrt[3]{1}$, i.e., $-0.5 \pm 0.86603i$. [37] Hénon intorduced the P3DROs in 1970 and denoted them as the "g3" family. [40] Representative members of the P3DRO family, as computed in the Earth-Moon system, are plotted in Figure 4.5, the orbits are colored by their Jacobi constant values. The P3DROs are an example of xz-symmetric periodic orbits with a more complicated geometry. The larger members of the P3DRO family, for example, exhibit multiple relatively close passes of the primaries per period. All members of the P3DRO family include multiple revolutions per period, in contrast to the parent DRO family, in which members only demonstrate one revolution per period. The Jacobi constant value, orbital period, and initial conditions for selected members of the P3DRO family in the Earth-Moon system are listed in Table 4.2. Only x_0 and $\dot{y}_0$ are included in the table as the initial condition takes the form of $\mathbf{x}_0 = \begin{bmatrix} x_0 & 0 & 0 & 0 & \dot{y}_0 & 0 \end{bmatrix}^T$. Given their orbit, it is evident that for a similar value of Jacobi constant, the P3DROs possess an orbital period that is approximately three times the orbital period of the corresponding DRO. The evolution of Jacobi constant value and period as a function of maximum excursion in the $\hat{x}$ direction appears in Figure 4.6. In the case of the P3DROs, maximum excursion in $\hat{x}$ is a unique identifier of an individual family member, while perilune radius, computed as the closest lunar approach along the trajectory, is not unique for each P3DRO.

Table 4.2. Initial Conditions for the Period-3 Distant Retrograde Orbits

JC	**Period**	$\mathbf{x_0}$	$\mathbf{\dot{y}_0}$
2.8342	15.9790376027	0.6330939655	0.8348788013
2.8111	16.5198140699	0.5826849060	0.9538709254
2.7746	17.0122192661	0.5175052261	1.1291604171
2.7216	17.3832543194	0.4427522764	1.3645830079
2.6577	17.6121513448	0.3719618249	1.6320786145
2.5855	17.7517947417	0.3081469240	1.9270583167
2.5125	17.8339899380	0.2553574418	2.2296738813
2.4420	17.8842284455	0.2124895320	2.5356356260
2.3777	17.9155197505	0.1788595441	2.8333212501
2.3162	17.9373234546	0.1506507145	3.1418355100
2.2599	17.9526104960	0.1277321783	3.4508888113
2.2086	17.9638166507	0.1089934411	3.7602690057
2.1634	17.9721331845	0.0940133448	4.0598647195
2.1210	17.9789687348	0.0811272362	4.3695771134
2.0824	17.9845610228	0.0703504270	4.6793766153
2.0474	17.9892638490	0.0612685284	4.9892343150
2.0164	17.9931880844	0.0537885307	5.2891344481
1.9872	17.9967493992	0.0471644337	5.5990584211
1.9604	17.9999177425	0.0414650619	5.9090018917
1.9358	18.0027715305	0.0365306853	6.2189592791

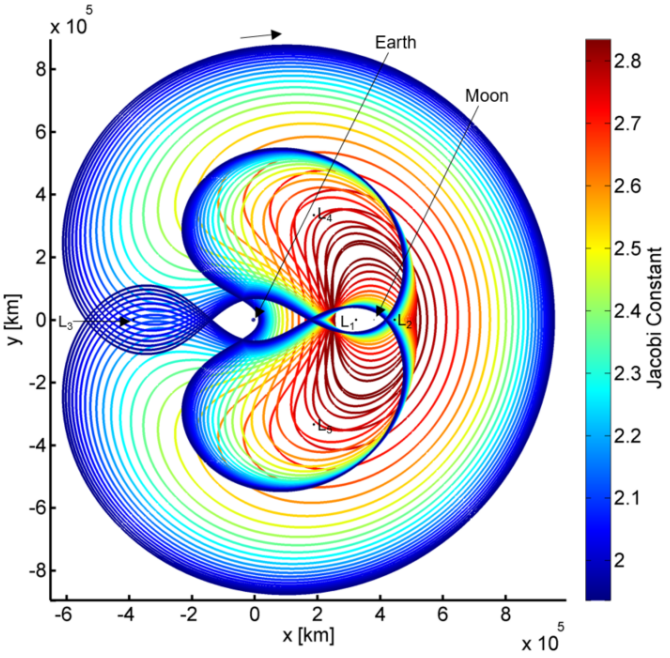

Figure 4.5. Family of period-3 distant retrograde orbits computed in the Earth-Moon system, colored by Jacobi constant value.

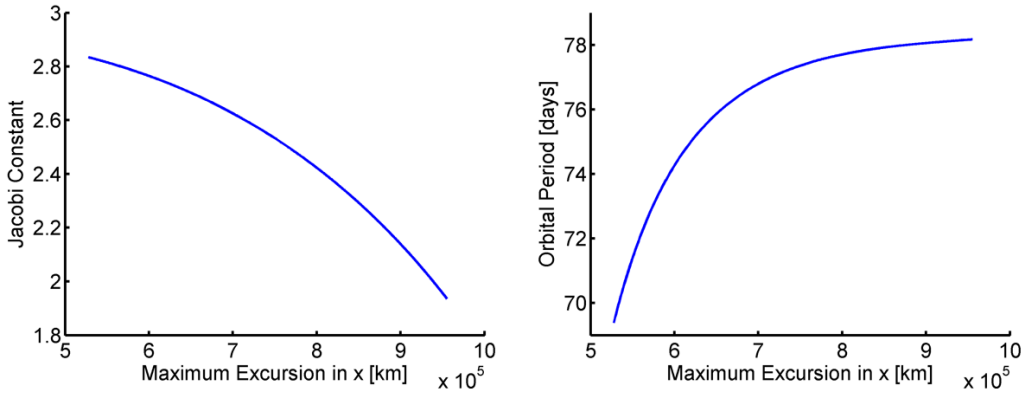

Figure 4.6. Jacobi constant value and orbital period as a function of maximum excursion in the $\hat{x}$ direction for representative orbits in the period-3 distant retrograde periodic orbit family in the Earth-Moon system.

Halo Orbits at Earth-Moon L_1

The halo orbits are a three-dimensional periodic family of orbits about the libration points, previously introduced as an example of computing a three-dimensional periodic orbit. Representative orbits over a large subsection of the halo family in the vicinity of the L_1 point in the Earth-Moon system are plotted in Figure 4.7 where the orbits are colored by Jacobi constant value. Interestingly, the L_1 halo orbits with the lowest values of Jacobi constant are associated with the largest z-amplitude. The L_1 halo family in Figure 4.7, and the corresponding initial conditions in Table 4.3, correspond to the "southern" family of periodic L_1 halo orbits. A reflection across the $z = 0$ plane through the application of the *Mirror Theorem* yields the "northern" L_1 halo family of orbits. [43] The initial values of x_0, z_0 and $\dot{y}_0$ are included in Table 4.3 since the initial state takes the form $\mathbf{x}_0 = \begin{bmatrix} x_0 & 0 & z_0 & 0 & \dot{y}_0 & 0 \end{bmatrix}^T$ in the case of a three-dimensional periodic orbit.

The evolution of the Jacobi constant value and the orbital period as functions of perilune radius for the L_1 halo orbits are plotted in Figure 4.8. Some of these orbits possess perilune radii that are subsurface, i.e., $r_p < R_{Moon}$. Although subsurface portions of the orbit may affect mission applications, computationally, these orbits are still valid solutions; the Moon is represented as a point mass in the CR3BP, therefore, solutions that pass closer to the center of the Moon than an arbitrary radius are still valid. Multiple L_1 halo orbits possess the same orbital period, and, in some cases, the same value of Jacobi constant, however, each family member is uniquely identified by its perilune radius as is evident in Figure 4.8.

Table 4.3. Initial Conditions for the L_1 Halo Orbits

JC	**Period**	$\mathbf{x_0}$	$\mathbf{z_0}$	$\mathbf{\dot{y}_0}$
2.7650	2.7159986012	0.8627102723	-0.4702996003	0.1351811306
2.8108	2.6303896376	0.8824867412	-0.4295792682	0.1168235652
2.8526	2.5253862155	0.8994896761	-0.3893500236	0.1017096929
2.8852	2.4186055725	0.9116731376	-0.3558608940	0.0916962219
2.9148	2.2965495319	0.9214943426	-0.3238011029	0.0848204819
2.9384	2.1788225624	0.9279940378	-0.2972096703	0.0819024094
2.9608	2.0492350902	0.9323498107	-0.2711617980	0.0829745365
2.9797	1.9284597334	0.9334331905	-0.2483007402	0.0899286329
2.9987	1.8126475049	0.9271716074	-0.2221003493	0.1154680681
3.0038	1.8551101606	0.9086559874	-0.2047314903	0.1643943779
3.0012	1.9744679048	0.8939591428	-0.1982839590	0.1969078447
2.9989	2.0945289103	0.8827711645	-0.1942766955	0.2187424072
2.9978	2.2277277332	0.8721327947	-0.1902448896	0.2369919140
2.9989	2.3534714874	0.8631244803	-0.1859405036	0.2500788516
3.0036	2.4902431159	0.8540778472	-0.1796085841	0.2600342141
3.0140	2.6174522586	0.8460069874	-0.1700375804	0.2641550784
3.0427	2.7462016488	0.8368126154	-0.1474695518	0.2560040701
3.0994	2.7866148671	0.8283954852	-0.1030921953	0.2186224503
3.1483	2.7626039170	0.8241429649	-0.0570525318	0.1675318330
3.1743	2.7430553931	0.8233901862	-0.0029876370	0.1264751431

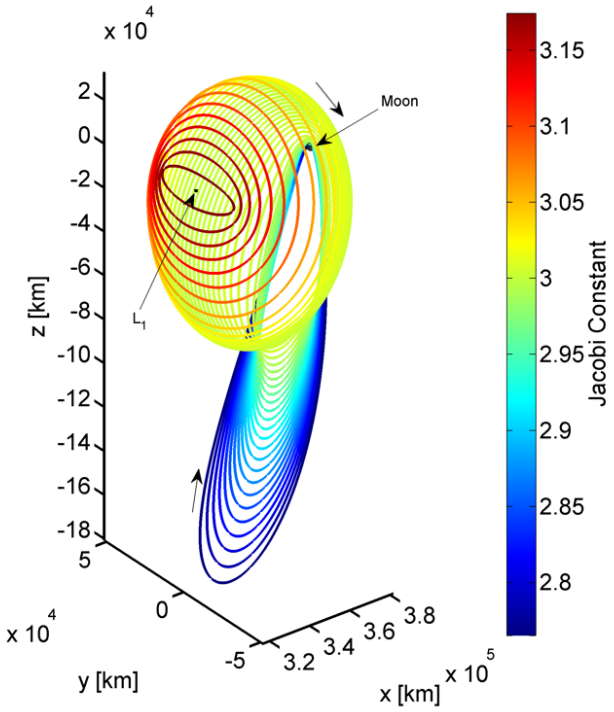

Figure 4.7. Family of L_1 halo orbits computed in the Earth-Moon system, colored by Jacobi constant value.

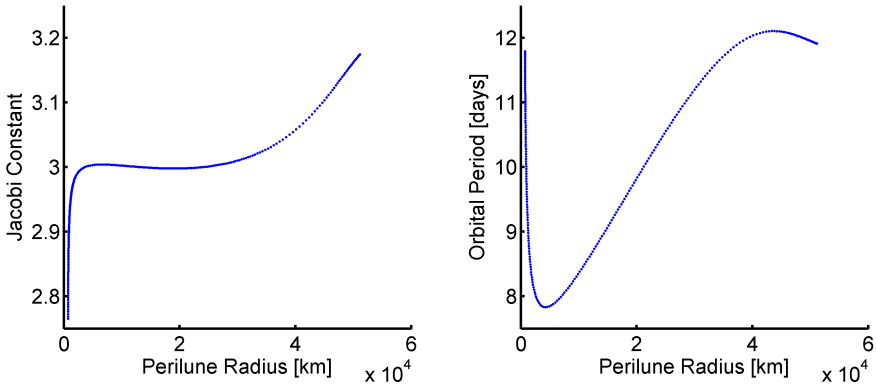

Figure 4.8. Jacobi constant value and orbital period as a function of perilune radius for the periodic L_1 halo orbit family in the Earth-Moon system.

Halo Orbits at Earth-Moon L_2

The L_2 halo family of three-dimensional periodic orbits bifurcates from the planar periodic Lyapunov family of orbits surrounding L_2. [24] Also termed halo orbits, there are significant differences between the L_1 and L_2 families of halo orbits. An orbiting particle in an L_1 halo orbit appears to move clockwise while the flow in L_2 halo orbits is counterclockwise, as viewed from Earth. Additionally, some member orbits in the L_1 halo family with the smallest perilune distances posses significantly large z-amplitude, even in the range of orbits plotted in Figure 4.7. In contrast, as the L_2 halo family evolves with lunar periapsis decreasing, the apoapsis distance also decreases. In terms of geometry in configuration space, the L_1 and L_2 families do share characteristics. In Figure 4.9, the southern L_2 halo family evolves from the bifurcation orbit in the xy-plane towards the smaller primary. The orbits are colored by Jacobi constant value. Again, the orbits in Figure 4.9 and the data in Table 4.4 corresponds to the southern branches of the L_2 halo family of periodic three-dimensional orbits. As before, x_0, z_0 and $\dot{y}_0$ are included in Table 4.4 since the initial condition for these three-dimensional periodic orbits takes the form $\mathbf{x}_0 = \begin{bmatrix} x_0 & 0 & 0 & 0 & \dot{y}_0 & 0 \end{bmatrix}^T$. A corresponding northern branch exists and is computed via the Mirror Theorem. Using a natural parameter continuation scheme in z and incrementing in the positive z-direction from the bifurcation orbit also produces the northern part of the L_2 halo family. In contrast to the L_1 family of halo obrits, both period and perilune radius uniquely identify a specific member of the family. Note that the orbit with the smallest value of Jacobi constant does not correspond to the orbit with the largest or smallest perilune radius. The southern L_2 halo family is the primary focus of this investigation. Significant interest in characteristics that this family of orbits possess is prevalent among multiple space agencies and private companies in support of a mission to create a long-term human habitat in cislunar space. [44] More specifically, interest lies in a subset of these orbits, i.e., the Near Rectilinear Halo Orbits (NRHOs), due to their favorable stability and eclipse avoidance characteristics. [7, 26, 27, 32, 45]

Table 4.4. Initial Conditions for the L_2 Halo Orbits

JC	**Period**	$\mathbf{x_0}$	$\mathbf{z_0}$	$\mathbf{\dot{y}_0}$
3.0591	1.3632096570	1.0110350588	-0.1731500000	-0.0780141199
3.0493	1.4748399512	1.0192741002	-0.1801324242	-0.0971927950
3.0411	1.5872714606	1.0277926091	-0.1858044184	-0.1154896637
3.0341	1.7008482705	1.0362652156	-0.1904417454	-0.1322667493
3.0283	1.8155211042	1.0445681848	-0.1942338538	-0.1473971442
3.0236	1.9311168544	1.0526805665	-0.1972878310	-0.1609628828
3.0199	2.0474562565	1.0606277874	-0.1996480091	-0.1731020372
3.0171	2.1741533495	1.0691059976	-0.2014140887	-0.1847950147
3.0155	2.2915829886	1.0768767277	-0.2022559057	-0.1943508955
3.0152	2.4093619266	1.0846726654	-0.2022295078	-0.2027817501
3.0162	2.5273849254	1.0925906981	-0.2011567058	-0.2101017213
3.0188	2.6455248145	1.1007585320	-0.1987609769	-0.2162644440
3.0234	2.7635889805	1.1093498794	-0.1946155759	-0.2211327592
3.0313	2.8909903824	1.1194130163	-0.1873686594	-0.2246002627
3.0424	3.0073088423	1.1297344316	-0.1769810336	-0.2254855800
3.0584	3.1205655022	1.1413664663	-0.1612996515	-0.2229158600
3.0807	3.2266000495	1.1542349115	-0.1379744940	-0.2147411949
3.1085	3.3173903769	1.1669663066	-0.1049833863	-0.1984458292
3.1359	3.3833013605	1.1766385512	-0.0621463948	-0.1748356762
3.1521	3.4154433338	1.1808881373	-0.0032736457	-0.1559184478

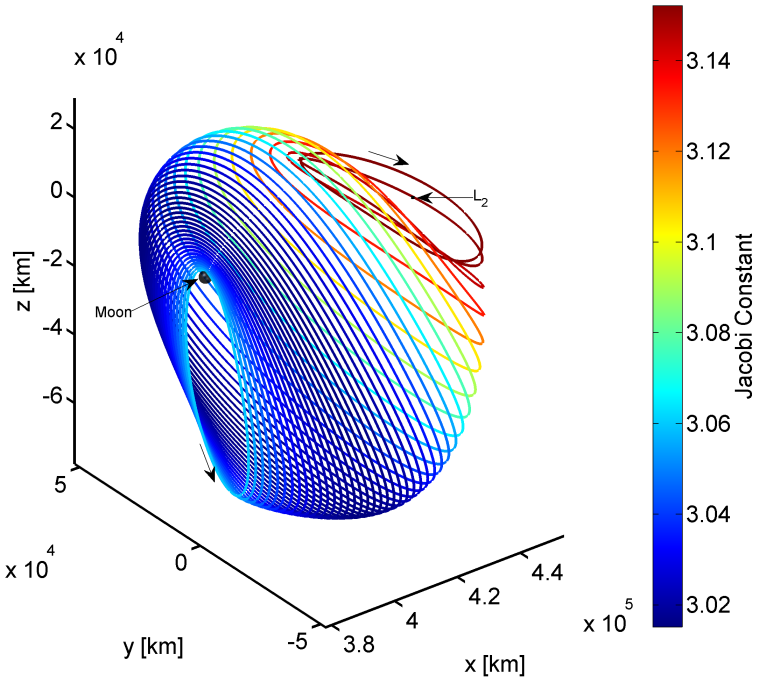

Figure 4.9. Family of L_2 halo orbits computed in the Earth-Moon system, colored by Jacobi constant value.

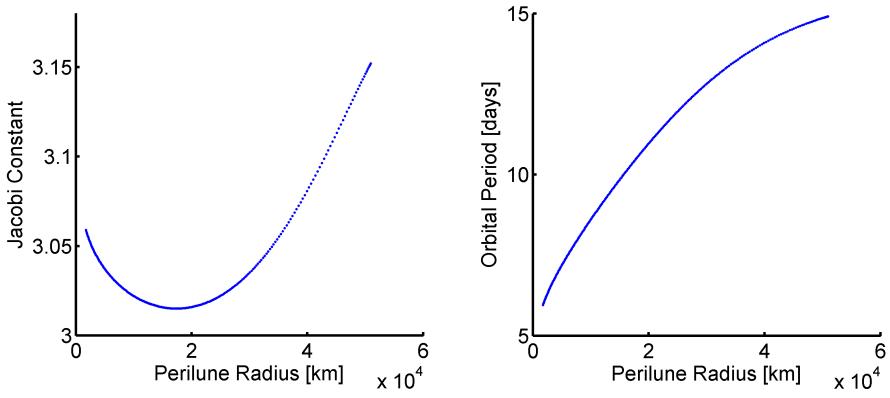

Figure 4.10. Jacobi constant value and orbital period as a function of perilune radius for the periodic L_2 halo orbit family in the Earth-Moon system.

4.2 Poincaré Mapping and Surfaces of Section

Poincaré mapping is a very useful approach to effectively reduce the dimensionality of a dynamical system and allow for concise visualization of the flow. [46] This technique, first introduced by Henri Poincaré in 1881, allows for insight into the design space. To construct a Poincaré map, a smooth surface of section, or hyperplane, at which trajectory crossings are recorded, is selected. This hyperplane, Σ, can be a physical plane (such as the $y = 0$ plane in configuration space) or can be nonphysical (such as periapsis or apoapsis occurrences). Typically, a specific value of Jacobi constant is selected for the Poincaré mapping process, which reduces the dimension of the dynamical system by one. The value of the Jacobi constant remains essentially constant throughout any numerical propagation. Then, a variety of initial conditions, all with the same Jacobi constant, are propagated. Each time the propagated trajectories cross the hyperplane, as illustrated in Figure 4.11, information concerning the trajectory is recorded. Any initial condition $\mathbf{x_0}$ on Σ is mapped forward in time to $P(\mathbf{x_0})$; both points appear discretely on the map. The mapping $\mathbf{x_0} \rightarrow P(\mathbf{x_0})$, termed the Poincarè map, preserves both stability and periodicity. [46] If an orbit is precisely periodic, then $P(\mathbf{x_0}) = \mathbf{x_0} = \mathbf{x^{PO}}$, and the process yields a single point on the hyperplane, i.e., a 'fixed point.' A fixed point on the Poincaré map resulting from periodic motion is also illustrated in Figure 4.11. Clearly, the flow is effectively visualized as discrete crossings of the hyperplane, Σ. Information about the crossings of Σ can then be plotted. As an example, each time a trajectory crosses the $y = 0$ plane, the values of x and $\dot{x}$ are plotted. The values of x, y, $\dot{x}$, and JC are then known and are effectively recorded on a two-dimensional plot, thereby simplifying visualization of the flow. Significant insight into the six-dimensional flow of a trajectory is gained by reducing the dimension of the system through the use of a Poincaré map. Additionally, Poincaré mapping allows for the comparison of many trajectories simultaneously and more completely than in configuration space, dramatically increasing the understanding of the design space.

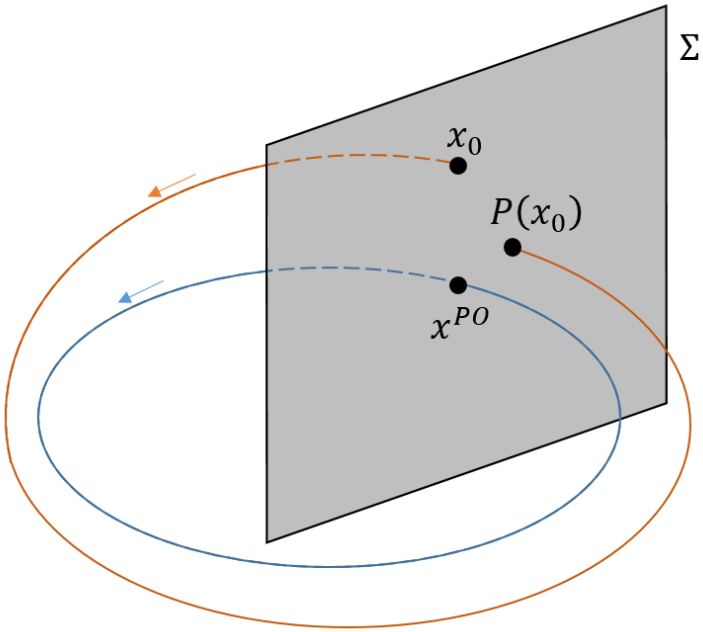

Figure 4.11. Poincaré map schematic, adapted from Perko. [46]

4.3 Computation of Periodic Orbit Invariant Manifolds

In the CR3BP, some periodic orbits are unstable and, therefore, possess both stable and unstable invariant manifolds. [35] In this application, invariant manifolds are six-dimensional structures that govern the flow toward and away from an unstable periodic orbit; leveraging this natural dynamical structure allows transfers to and from the orbit for relatively minor maneuver cost. Manifold structures are, therefore, often a basis for transfer design techniques. Orbit stability, as determined from the eigenvalues of the monodromy matrix determines the types of manifold structures that an orbit possesses. Unstable eigenvalues ($|\lambda_i| > 1$) correspond to unstable manifold structures that depart a periodic orbit, likewise, stable eigenvalues ($|\lambda_i| < 1$) correspond to stable manifold structures that flow into a periodic orbit. Eigenvalues with a magnitude equal to unity lead to the existence of the center manifolds

in which the flow remains in the vicinity of the baseline periodic solution. Since the eigenvalues of the monodromy matrix appear in reciprocal pairs, stable and unstable manifolds always occur together. Periodic orbits also always possess a center manifold structure due to the existence of two eigenvalues of the monodromy matrix equal to unity. Some periodic orbits are stable and possess only center manifolds, therefore, no natural flow towards and away from the orbit exists; one such example is the DROs and some members of the halo families. Thus, manifolds associated with unstable periodic orbits that possess both stable and unstable manifolds, such as the P3DROs, are used to aid transfer design between stable periodic orbits that lack stable and unstable manifold structures.

To compute stable and unstable manifold structures, or, more specifically, trajectories that lie along these manifold surfaces, a step in the direction of the stable or unstable mode of a fixed point, $\mathbf{x_i^{PO}}$, along the periodic orbit must first be taken. The directions of the stable and unstable modes corresponding to a fixed point are determined by the eigenvectors of the monodromy matrix, $\mathbf{\Phi}(t_0 + P, t_0)$, that correspond to the stable and unstable eigenvalues, respectively. Since the mondoromy matrix refers to a discrete time system, the stability bound for the eigenvalues of this matrix is the unit circle. Stable eigenvalues have magnitude less than unity and unstable eigenvalues have magnitude greater than unity. States in which a step has been taken in the direction of a stable or unstable eigenvector, are written as

$$\mathbf{x_S} = \mathbf{x}_i^{PO} \pm \epsilon \boldsymbol{\nu}_S, \quad \mathbf{x}_U = \mathbf{x}_i^{PO} \pm \epsilon \boldsymbol{\nu}_U \tag{4.15}$$

where $\boldsymbol{\nu}$ is an eigenvector of $\mathbf{\Phi}(t_0 + P, t_0)$ that has been normalized with respect to the position coordinates and ϵ is a small perturbation amount in terms of distance that allows for the numerical computation of the manifold structure. [35] A typical value for ϵ is approximately 50 km; larger values are sometimes needed if the the manifolds depart slowly, as is the case for a nearly stable orbit. The perturbed states, $\mathbf{x_S}$ and $\mathbf{x_U}$, are then integrated using the equations of motion. For a stable manifold,

in which the manifold trajectory approaches the fixed point, numerical integration is accomplished in reverse time. In contrast, an unstable manifold departs the fixed point in forward time. The collection of all manifold trajectories from each fixed point along a periodic orbit comprise the manifold surface. A more detailed explanation of manifold theory is detailed in Perko [46] and Koon et al. [35]

4.4 Transitioning CR3BP Solutions into the Ephemeris Model

Often, when a higher fidelity model is necessary for certain applications, preliminary trajectory design is first accomplished in the CR3BP and then transitioned into the higher fidelity N-body ephemeris model. Building a solution in the CR3BP, prior to working within the N-body ephemeris model, is beneficial due to the simplifying assumptions in the CR3BP, the predictable repeating behavior (especially in the case of periodic motion), and the lack of dependence on the epoch. Designing trajectories to meet mission requirements directly in the N-body ephemeris model is possible as well, although it is generally challenging without an a priori solution. In this investigation, trajectory solutions and periodic orbits are computed within the context of the CR3BP and then transitioned to the N-body ephemeris model for further analysis of the effects of higher-order perturbations.

Once a suitable solution is available in the CR3BP, transitioning the solution to the ephemeris model is, in theory, straightforward. Recall that the CR3BP is formulated in a barycenter-centered rotating frame and the N-body ephemeris model is formulated in the J2000 inertial frame. The strategy presented in Section 3.3.2 is used to transition CR3BP patchpoints, i.e., six-dimensional states at intervals along a trajectory arc, from the rotating frame to patchpoints in the J2000 inertial frame at a given epoch. Then, the transformed patchpoints, or state vectors, are converged to a continuous path via a differential corrections technique to enforce continuity and other constraints within the N-body force model. In practice, however, the

transformed patchpoints may not supply a sufficient initial guess for the differential corrections process and resulting in convergence challenges. Additional efforts focused on the numerical process may be necessary. For example, some benefit may be gained by introducing elements of the higher-fidelity model one at a time. As a starting point, the trajectory can first be converged in the N-body ephemeris model with only the primary bodies from the CR3BP influencing the motion of the body of interest. Such a solution differs from the CR3BP solution because the eccentricity of the orbits of the primary bodies as well as epoch date dependence is accommodated within the higher-fidelity model. Then, additional perturbing bodies can be added, one at a time, with the previous solution serving as an initial guess for the next trial. Additionally, attempting to enforce too many constraints simultaneously is challenging in the N-body ephemeris model. Adding constraints one at a time or relaxing certain constraints in preliminary corrections iterations can aid convergence.

Four revolutions along an L_2 halo orbit serve as an example of transitioning a CR3BP orbit or arc to the ephemeris model. In this example, the epoch date is January 25, 2025. The CR3BP periodic L_2 halo orbit possesses a perilune radius equal to 26043 km and an orbital period of 12.15 days. This particular orbit in the CR3BP is plotted in Figure 4.12 in the Earth-Moon rotating frame (red dashed orbit) along with the corresponding trajectory that is converged in the ephemeris model including the gravity of the Earth, Moon, Sun, and Jupiter (EMSJ), plotted as the blue trajectory. Note that the precise periodicity of the halo orbit no longer appears in the ephemeris model and the trajectory varies slightly from the CR3BP counterpart, although a similar geometry is maintained.

4.4.1 Apse Angle

Periodic motion, such as that of the halo orbits in the CR3BP, results in quasi-periodic behavior when transitioned to a higher-fidelity ephemeris force model. Pre-

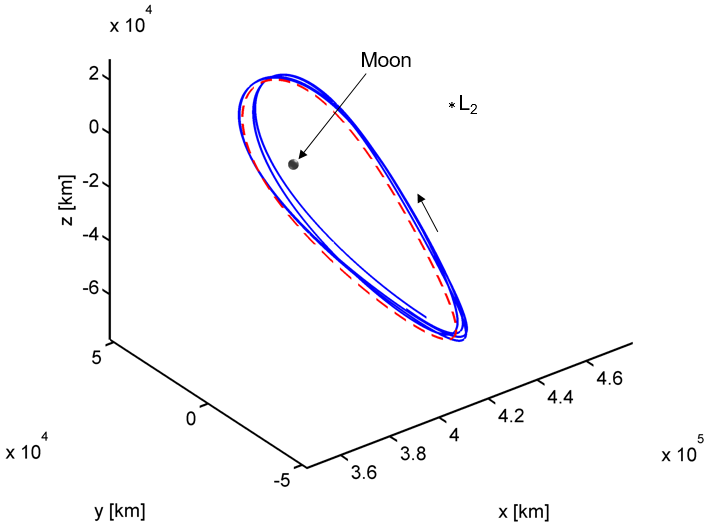

Figure 4.12. Transition of four revolutions of a CR3BP L_2 halo orbit (red dashed) to the EMSJ ephemeris model (blue solid).

cisely periodic motion is no longer apparent in a higher fidelity N-body ephemeris model due to additional perturbations. The transition between force models of varying fidelity can result in either "tight," nearly-periodic motion or "loose," more variable revolutions along a trajectory path. Practitioners frequently examine the representative trajectory in configuration space and seek a parameter that reflects the fundamental dynamical structure. A metric, denoted the apse angle α, is defined to represent the spread of the revolutions along the orbit from a precisely periodic CR3BP analog. The apse angle is particularly useful in the NRHO region within the halo family of orbits. For an NRHO, the projection of the orbit into the yz-plane is most insightful to clarify the apse angle. This metric is depicted in Figure 4.13 for a "loose," more variable orbit and in Figure 4.14 for a "tight" orbit that remains close to the corresponding CR3BP analog.

The apse angle is a measure of both the degree to which one revolution of an ephemeris trajectory mirrors the previous revolution (i.e., the 'excursion' of a series

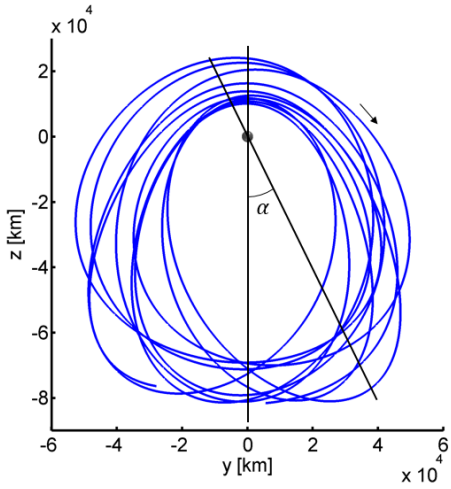

(a) An ephemeris trajectory with a "loose" appearance in the Earth-Moon rotating frame.

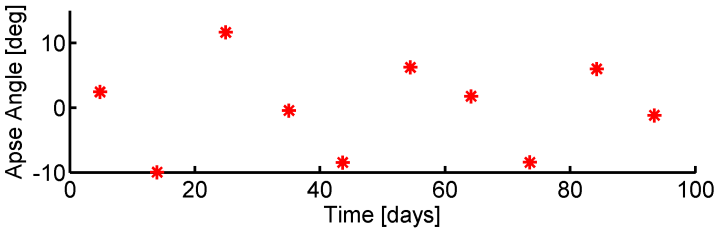

(b) A wide range of apse angle corresponding to a "loose" orbit.

Figure 4.13. An ephemeris trajectory with a wider spread relative to a corresponding CR3BP orbit.

of revolutions from the nominal path) and a metric to assess the drift of an ephemeris trajectory away from a periodic orbit as computed in the CR3BP. As is apparent in Figures 4.13 and 4.14, the apse angle is zero if the orbit is perfectly periodic. For application to three-dimensional orbits that are periodic in the CR3BP, such as the halo orbits, the apse angle tracks the evolution of a corresponding ephemeris trajectory. The apse angle is evaluated as the osculating argument of periapsis, computed along the ephemeris path such that α is evaluated at the closest approach to the Moon.

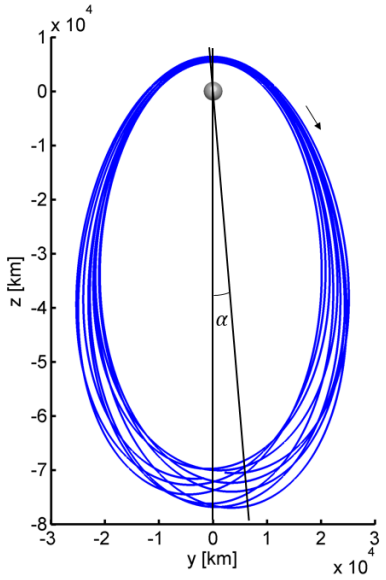

(a) An ephemeris trajectory with a "tight" appearance in the Earth-Moon rotating frame.

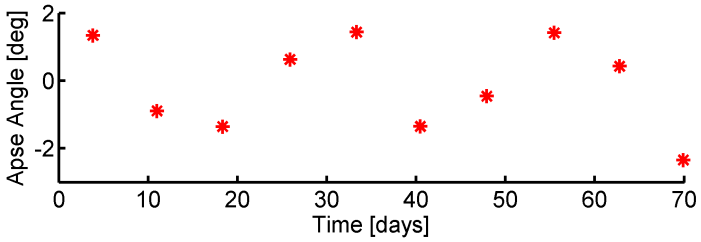

(b) A narrow range of apse angle corresponding to a "tight" orbit.

Figure 4.14. An ephemeris trajectory with a narrow spread that remains close to a corresponding CR3BP orbit.

Then, 90° is subtracted from the value such that the apse angle is measured relative to zero. Thus, the apse angle is computed as

$$\alpha = \omega_{inst}(r_p) - 90^\circ \tag{4.16}$$

where $\omega_{inst}(\cdot)$ indicates the osculating argument of periapsis. Since the apse angle is computed at the closest approach along a trajectory, it is only evaluated once every revolution. By definition, a CR3BP xz-symmetric periodic orbit retains a constant

apse angle, $\alpha = 0^\circ$ since the $\omega_{inst}(r_p) = 90^\circ$. As observed in Figure 4.13, the apse angle can vary widely from revolution to revolution along an ephemeris trajectory. In Figure 4.13(a), a 3:1 synodic resonant NRHO is used as an initial guess and converges to a continuous path in the EMSJ ephemeris model using only a continuity constraint. Alternatively, it is apparent in Figure 4.14–converged given a 4:1 synodic resonant NRHO as the initial guess from the CR3BP–that some ephemeris trajectories closely resemble a corresponding CR3BP counterpart, i.e., the ephemeris trajectory displays nearly repeating behavior. Interestingly, since the orbits in both Figures 4.13(a) and 4.14(a) are, in fact, a 3:1 synodic resonant NRHO and a 4:1 synodic resonant NRHO, respectively, some cyclic behavior in the apse angle is clearly observed in the plots of α in Figures 4.13(b) and 4.14(b). Apse angle is used to identify orbit resonances when visual inspection alone, e.g., in Figure 4.13(b), may not reveal any obviously repeating behavior.

5. MISSION APPLICATIONS: ORBITAL CHARACTERISTICS AND TRANSFER DESIGN

The National Aeronautics and Space Administration (NASA), international partners, and a variety of private organizations view a far-reaching human presence, beyond LEO, as a crucial step in the creation of a strong space economy and as a part of the journey for humans to reach Mars and beyond during the 21st century. [1, 2] With this goal in mind, NASA has selected the L_2 NRHOs as a potential future location for a long-term crewed habitat in cislunar space. This habitat, known as the Deep Space Gateway (DSG), allows for validation of the required systems for Earth independent human support in space and is critical in the establishment of the Deep Space Transport (DST) functionality to ultimately allow human travel into deep space. [1]

To successfully create a long term cislunar habitat, a stable or nearly stable orbit in the Earth-Moon system, one that is able to be maintained over a long interval with minimal propellant cost, is required. The NRHOs offer favorable stability characteristics with the additional benefit of possessing a direct communications link to the Earth. [7,8] As mission constraints often include limits on the thermal environment for the spacecraft and power requirements often limit the allowable time intervals without illuminated solar panels, eclipse duration and frequency are strong considerations for trajectory designs. [45] Some NRHO characteristics that allow for successful eclipse avoidance are highlighted. Orbits associated with an L_2 family typically possess lower access cost than orbits associated with L_1 families [30]. Southern NRHOs are selected due to interest in communications coverage of the south pole of the Moon, a potential location for a ground station. [47] To establish the DST functionality, transfers

between the DSG and other orbits in cislunar space are also of interest. In support of this goal, preliminary transfers between the NRHOs and DROs, another stable orbit of interest in cislunar space, are investigated in conjunction with direct transfers from LEO to the NRHO in support of the construction of the DSG habitat and for crewed transport.

5.1 Stability

The stability of an orbit strongly influences various mission applications. Orbit stability can impact processes, for example, transfer design to and from the orbit can be more efficient due to the existence of manifolds. But, the stability of the orbit also influences outcomes, e.g., stationkeeping costs. For a long-duration mission, such as the DSG, the ability to maintain an orbit for a low cost is crucial, however, insertion options and access to a range of other cislunar orbits is also deemed essential. Thus, orbital stability is a key consideration. A stable, or nearly stable, periodic orbit in the CR3BP is thereby desirable. The stability of a periodic orbit is deduced through the eigenvalues of the monodromy matrix. [35] Recall that the general solution to the linear variational equations derived from the equations of motion in the CR3BP, linearized relative to a given periodic orbit, are written as

$$\delta\mathbf{x}(t) = \mathbf{\Phi}(t, t_0)\delta\mathbf{x}(t_0) \tag{5.1}$$

where $\delta\mathbf{x}(t)$ is the variation relative to the initial state along the orbit and $\mathbf{\Phi}(t, t_0)$ is the State Transistion Matrix (STM) relating the variation at the initial time, t_0, to the variation at some downstream time, t. Since the STM is not a constant matrix and, therefore, not straightforwardly decomposed into eigenvalues and eigenvectors to

assess stability, Floquet techniqeus are employed to decompose the STM and analyze the stability of this time-varying matrix. [37] The decomposed STM is written as:

$$\mathbf{\Phi}(t, t_0) = \mathbf{F}(t)e^{\mathbf{\Omega}t}\mathbf{F}(t_0)^{-1} \tag{5.2}$$

where $\mathbf{F}(t)$ is a periodic matrix and the diagonal elements of the matrix $\mathbf{\Omega}$ are labelled the Poincaré exponents, σ_i. [35] Since $\mathbf{F}(t)$ is periodic, $\mathbf{F}(P + t_0) = \mathbf{F}(t_0)$. Then, assuming $t_0 = 0$, the monodromy matrix is expanded as

$$\mathbf{\Phi}(P, 0) = \mathbf{F}(0)e^{\Omega(P)}\mathbf{F}(0)^{-1} \tag{5.3}$$

Since $e^{\mathbf{\Omega}P}$ is a diagonal matrix, it is clear that $\mathbf{F}(0)$ is formed from the eigenvectors of the monodromy matrix. The diagonal elements of $e^{\mathbf{\Omega}P}$ are, therefore, the eigenvalues of the monodromy matrix, λ_i, where $\lambda_i = \pm e^{\sigma_i P}$. The eigenvalues of the monodromy matrix are the modes that dictate the linear behavior in the vicinity of a periodic orbit and, therefore, the stability of a periodic orbit.

A periodic orbit possesses six eigenvalues and a set of associated eigenvectors. Two eigenvalues, denoted the trivial pair, are always equal to one; these eigenvalues correspond to the periodicity of the orbit and the membership of the orbit in a family of related solutions. The other four eigenvalues occur as two reciprocal pairs and are of the form $\lambda_i = a \pm bi$, where a and b are real numbers. There are two possible forms for each of the nontrivial eigenvalues:

- Complex roots that occur in conjugate pairs, i.e., $\lambda_{1,2} = a \pm bi$. If these roots lie on the unit circle (with magnitude equal to one) then the solution is bounded; a perturbed path neither approaches nor departs from the reference path over time.

- Real roots that occur in reciprocal pairs, i.e., $b = 0$ and $\lambda_1 = a$, $\lambda_2 = 1/a$. These roots correspond to exponential growth or decay of the variation between the reference and perturbed paths over time. An eigenvalue with magnitude greater

than one corresponds to the unstable mode while the eigenvalue with magnitude less than one indicates stable behavior.

The stability of a periodic orbit is described by considering the form and magnitude of each of the four nontrivial eigenvalues. Additionally, when the form and/or the character of the orbital stability changes over a family of orbits, a bifurcation occurs. [46]

5.1.1 CR3BP: Stability Index

It is useful to define a single metric for the purpose of describing the stability of an orbit or for monitoring the likelihood that certain types of bifurcations occur at a specific periodic orbit along a family. Excluding the trivial pair, the reciprocal pairs of eigenvalues, $(\lambda_i,\, 1/\lambda_i)$, are combined to form the stability index, defined as

$$\nu_i = \tfrac{1}{2}\left(\lambda_i + 1/\lambda_i\right) \tag{5.4}$$

for $i = 1, 2$. [24] Each orbit therefore possesses two stability indices. If the stability indices for a particular periodic orbit, ν_i, are both less than one in modulus, then the orbit is stable in a linear sense. Otherwise, if either of the stability indices possess magnitude greater than one, the orbit is unstable. For a diverging path, a larger value of the stability index corresponds to a faster departure from the reference path.

The plots in Figure 5.1 highlight select members of the L_1 and L_2 halo families and delineates the perilune radii and stability indices for each of these orbits. The L_1 and L_2 halo orbits that exist closer to the respective Lagrange points are unstable with stability indices of magnitudes much larger than one while the halo orbits nearer to the smaller primary possess much smaller stability indices of magnitude nearer to one, as is illustrated by the plots of the stability indices for the L_1 and L_2 halo families of periodic orbits plotted in Figure 5.2.

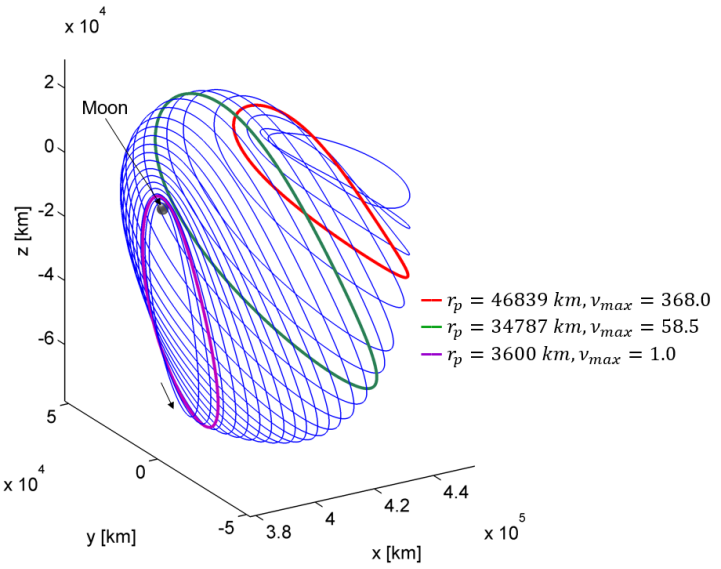

(a) Perilune radius and maximum stability index for select members of the L_2 halo family.

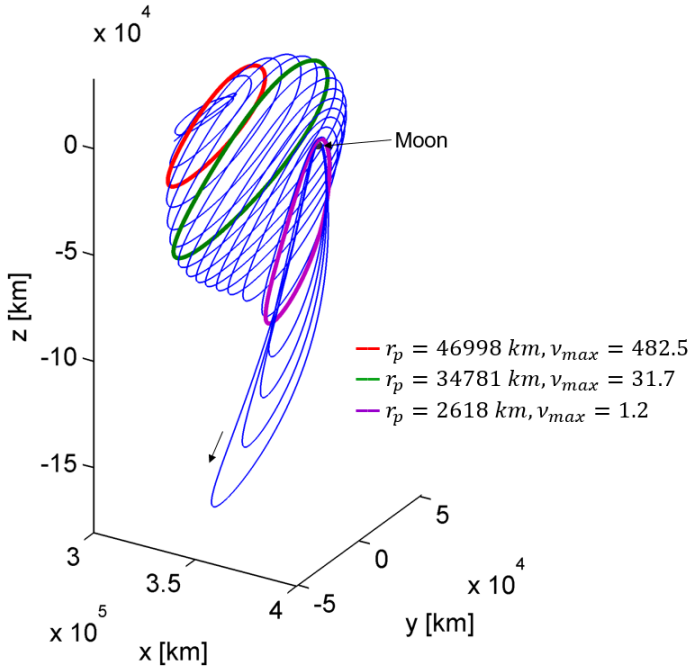

(b) Perilune radius and maximum stability index for select members of the L_1 halo family.

Figure 5.1. Perilune radius and maximum stability index for selected members of the L_1 and L_2 halo families of peridic orbits.

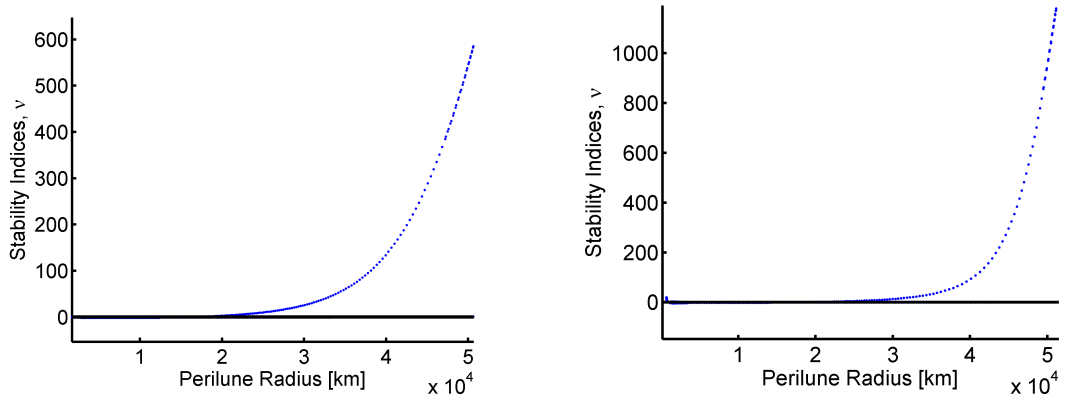

(a) Stability index across the L_2 halo family.

(b) Stability index across the L_1 halo family.

Figure 5.2. Stability index across the halo families in Figure 5.1 showing that the orbits near the Lagrange points are unstable.

The region of interest near the Moon, shown in Figure 5.3, is characterized by stable (or nearly stable) orbits. In fact, the linear stability characteristics associated with the halo families of periodic orbits in the CR3BP serve to delineate the boundaries for the subsection of halo orbits labeled the Near Rectilinear Halo Orbits (NRHOs). In the region of interest near the Moon, across both the L_1 and L_2 halo families, a number of stability switches, or bifurcations, occur. The NRHOs are defined as the subsection of the halo orbit family near the smaller primary body that possesses stability indices all within some small bound surrounding ± 1 and with no stability index that is significantly larger in magnitude than the others. Therefore, an L_2 NRHO is defined, in the Earth-Moon system, as a halo orbit between the first and third stability changes in the region of the smaller primary, marked with arrows in Figure 5.3(a). These stability changes occur at halo orbits possessing perilune radii of 1832 km and 17390 km, respectively. The L_1 NRHOs are defined similarly as the orbits between the first and fourth stability changes within the Earth-Moon system, marked with arrows in Figure 5.3(b). The perilune radii for the NRHOs that coincide with these stability changes are 934 km and 19062 km. Orbits within these bounds,

labeled the L_1 and L_2 NRHOs, are shaded green in Figure 5.4; other members of the respective halo families are colored blue.

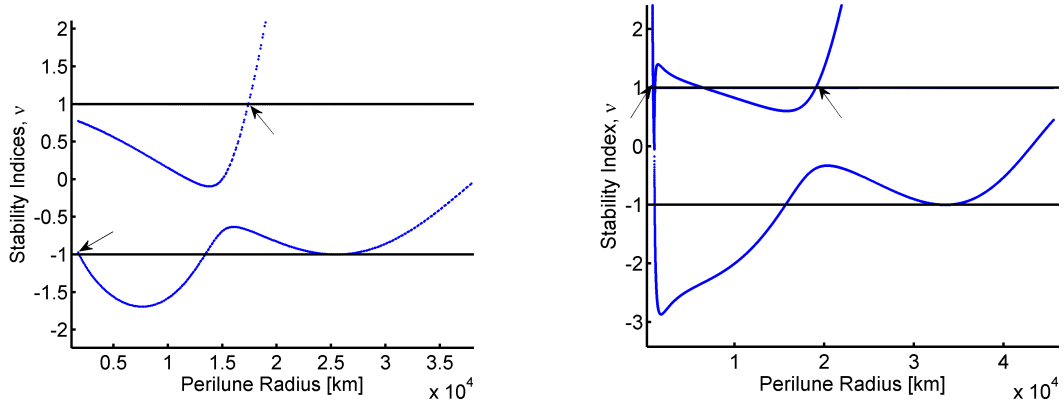

(a) Stability index across the L_2 halo family in the region near the smaller primary.

(b) Stability index across the L_1 halo family in the region near the smaller primary.

Figure 5.3. The region of bounded values of the stability index defines the interval across the halo orbits that are defined as NRHOs.

The definition for the NRHO region for the L_1 and L_2 families of halo orbits equivalently applies to both the northern and southern members. Interestingly, the orbital geometry of the NRHOs, characterized by an elongated, out-of-plane ellipse-like shape in the CR3BP rotating frame, also distinguishes these orbits from the other halo family members. Recall that the Earth-Moon L_2 NRHOs perilune radii range from approximately 1850 km to 17350 km. (Note that the lunar radius is approximately 1737 km, so each of the L_2 NRHOs are accessible in the Earth-Moon system.) The orbital periods across the L_2 NRHOs are between approximately 6 days and just over 10 days, as evident in Figure 4.10. The L_1 NRHOs are characterized by perilune radii ranging from approximately 900 km to 19000 km with periods between approximately 8 days and 10 days, as plotted in Figure 4.10. Not all of the L_1 NRHOs are accessible in the Earth-Moon system, as some intersect the lunar surface. Recall

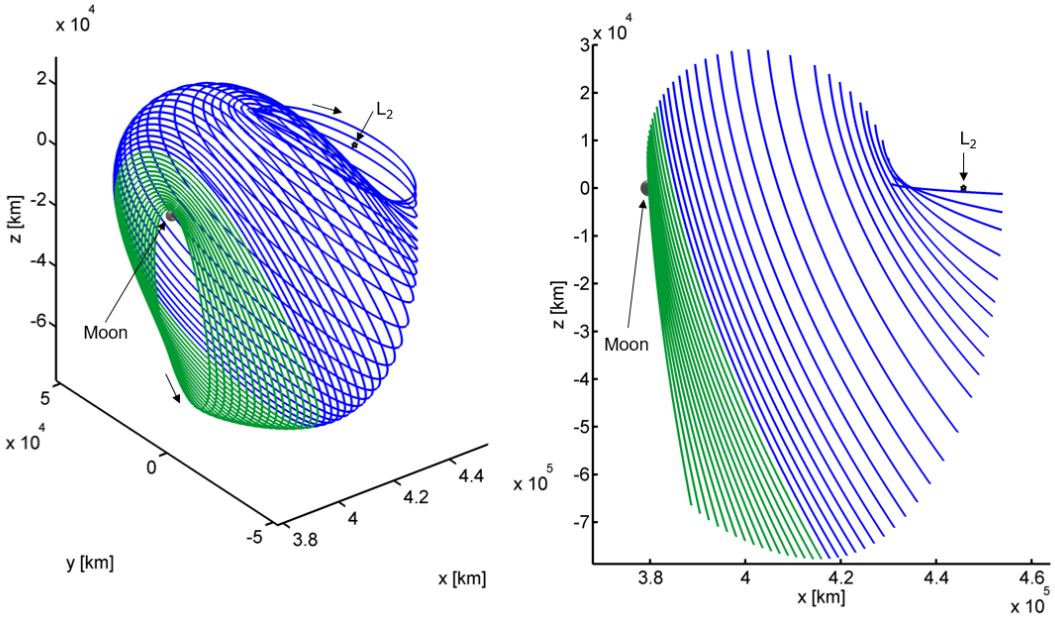

(a) The southern L_2 halo family in the Earth-Moon system.

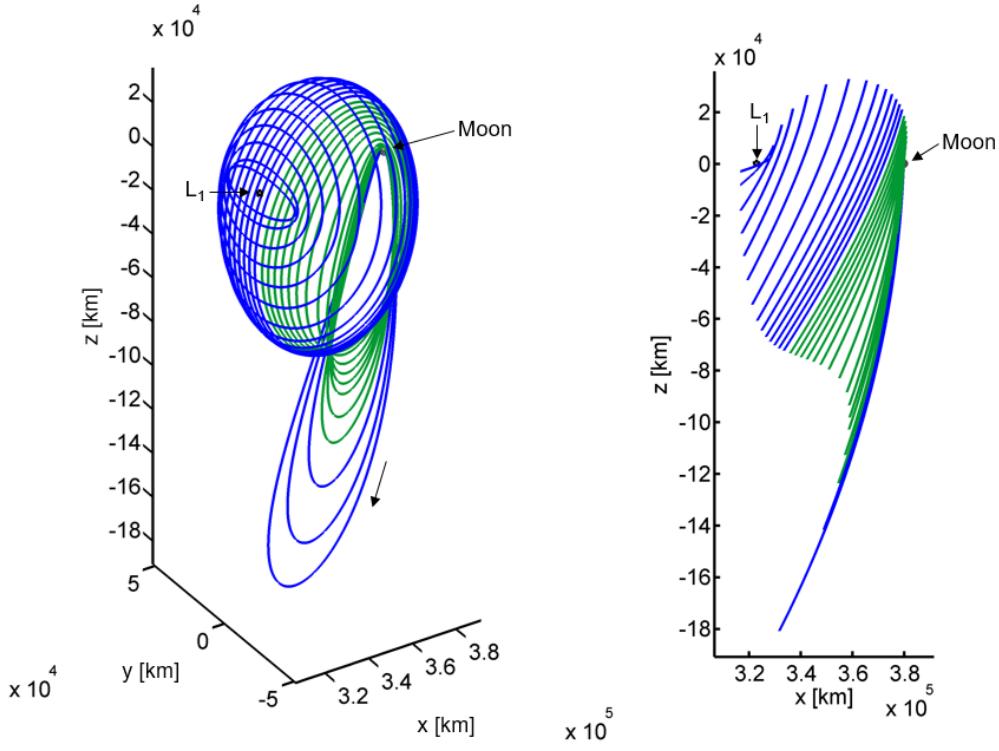

(b) The southern L_1 halo family in the Earth-Moon system.

Figure 5.4. The L_1 and L_2 NRHO regions (green) delineated from the larger halo families (blue).

that Figures 4.8 and 4.10 highlight the Jacobi constant values across the L_1 and L_2 halo families, respectively. Any NRHOs that have stability indices such that $|\nu_i| > 1$ are considered unstable. However, across the NRHO region of the halo families, the magnitude of the stability indices remains close to one. Therefore, the divergence rate is significantly slower than for other halo orbits that are closer to the L_2 or L_1 Lagrangian points, as evaluated in the Earth-Moon system. The temporal scale for the divergence in the case of instability is approximately predicted by the modulus of the stability index. Therefore, when the stability indices possess magnitudes close to one, divergence is slow. Some of the NRHOs, while technically unstable, are considered practically or operationally stable due to their slow rate of divergence. The temporal scale of the diverging motion is derived by considering the time constant, τ, as measured in terms of the number of revolutions corresponding to the dominant motion. The time constant is defined as:

$$\tau[\text{rev}] = \frac{1}{\max\left(\text{abs}\left(\text{real}\left(\sigma_i\right)\right)\right)}\frac{1}{P} = \frac{1}{\max\left(\text{abs}\left(\text{real}\left(ln\left(\lambda_i\right)\right)\right)\right)} \tag{5.5}$$

where $\sigma_i = ln(\lambda_i)/P$ is the Poincaré exponent associated with the monodromy matrix of the periodic orbit. The time constant is infinite for a stable orbit due to the fact that $\lambda_{\max}(\Phi(P,0)) = 1$, $ln(1) = 0$, and $\frac{1}{0} = \infty$, i.e., divergence requires infinite time. Assuming that the growth is proportional to the exponential function $e^{\frac{t[\text{rev}]}{\tau[\text{rev}]}}$, the time constant, τ, is physically interpreted as the time interval necessary for a given initial perturbation to grow by a factor of $e \approx 3$. The time constants defined in terms of number of revolutions till departure (i.e., a perturbation amplifies by three) for the L_1 and L_2 halo orbits in the vicinity of the smaller primary are displayed in Figure 5.5. Note that the NRHOs are either stable or depart in approximately one full revolution. Larger halo orbits, such as those in the vicinity of the Lagrange points, possess larger values of the stability index, and are thus, more unstable and therefore depart much faster–on the order of fractions of a revolution. Favorable stability properties and, thereby, the time scale of divergence in the case of instability, as observed in the CR3BP, suggest the possibility of maintaining NRHO motion over a

long duration. Due to a slow departure rate, few propellant resources are theoretically required to maintain the NRHOs. Since stability is determined in a linear sense, the introduction of a stationkeeping algorithm to maintain NRHO-like motion in a higher-fidelity environment is necessary. [26, 27]

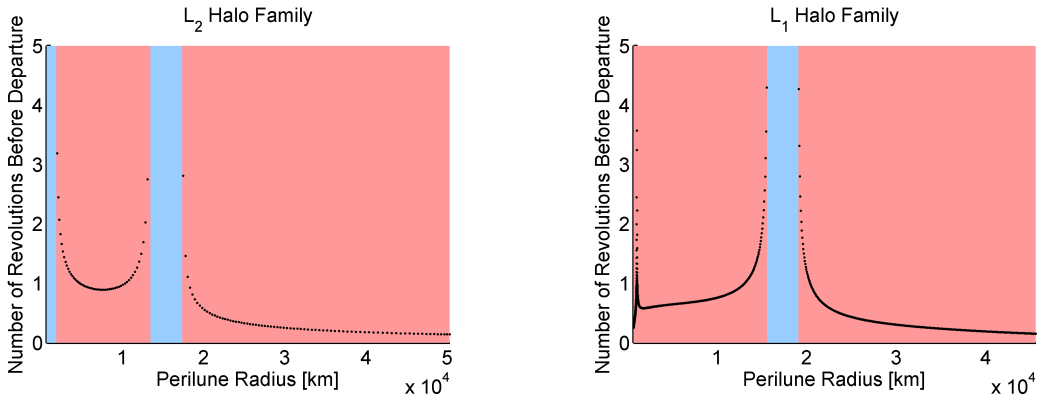

(a) Time constant as a function of perilune radius across the L_2 NRHOs.

(b) Time constant as a function of perilune radius across the L_1 NRHOs.

Figure 5.5. Linear time constant for the NRHO regions within the Earth-Moon system. Blue regions indicate marginally stable orbits; red regions denote unstable orbits.

The distant retrograde orbits are a stable family of periodic orbits about the smaller primary. These orbits, due to their favorable stability properties, are also of interest for long duration missions. In fact, these orbits continue as a focus due to analysis of their use in support of the Asteroid Redirect Mission (ARM) [3] as well as for a staging-ground orbit as part of NASA's mission to reach Mars. [32]. The stability indices for the DROs are plotted in Figure 5.6. Note that the stability indices remain between -1 and 1 over all of the DROs examined, indicating marginal stability. Therefore, a perturbations to a nominal DRO would never depart the vicinity of the original orbit in the CR3BP. The related family of period-3 distant retrograde orbits are, on the other hand, unstable. This instability leads to the existence of

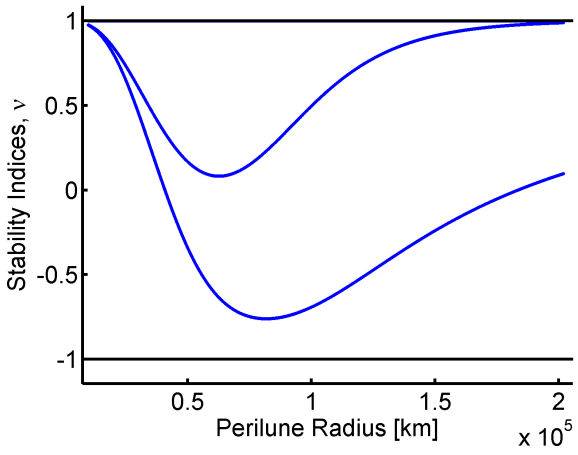

Figure 5.6. Stability index as a function of perilune radius across the DRO family.

both stable and unstable manifold structures associated with the P3DRO periodic orbits. The stability indices for the P3DROs are plotted in Figure 5.7 as a function of maximum excursion in x. Note that over all of the P3DROs considered, at least one stability index has magnitude greater than one. The associated time constant for these orbits are displayed in Figure 5.8, in this plot the red color denotes unstable orbits. Although orbit stability is an important consideration when planning a long-duration mission, other considerations are also a high priority.

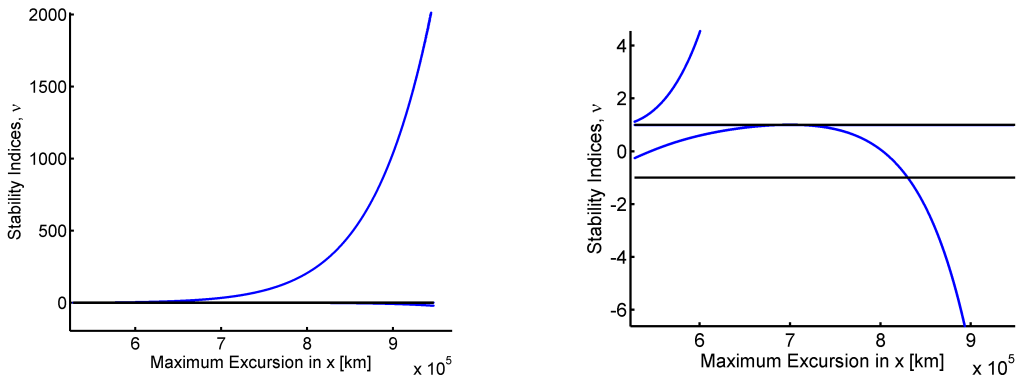

(a) Stability index as a function of maximum excursion in x across the P3DROs.

(b) Stability indices in the region near the stability bounds (± 1).

Figure 5.7. Stability index for the P3DROs within the Earth-Moon system.

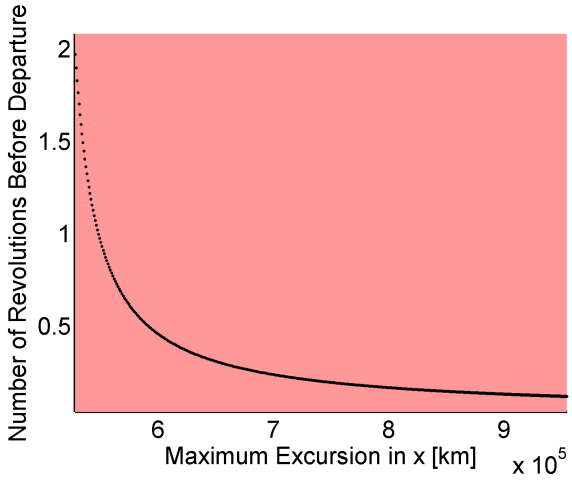

Figure 5.8. Linear time constant as a function of maximum excursion in $\hat{x}$ across the P3DRO family; the red color denotes unstable orbits.

5.2 Eclipsing

Mission constraints on the trajectory often arise from a wide variety of operational requirements. For example, limitations usually exist on the thermal environ-

ment surrounding the spacecraft (the spacecraft cannot become too cold) and, the flight management plan may limit time intevals without a direct communications link to Earth. Additionally, power requirements dictate the maximum allowable time interval without illumination of the solar panels. In fact, these types of restrictions actually dictate the allowable eclipse duration and frequency. [45] The NRHOs offer favorable eclipsing properties due to their primarily out-of-plane orientation. Additionally, because periapsis along an NRHO occurs in close proximity to the Moon and, therefore, the lunar shadow, eclipse durations are relatively short since there is high orbital velocity throughout shadow encounters. Spacecraft in NRHOs are exposed to both Earth eclipse and lunar eclipse conditions. In this investigation, designs to minimize shadow event duration are explored.

5.2.1 Resonance

Orbital resonance plays an important role in designing orbits that ultimately meet eclipse constraints; the position of a spacecraft in a resonant orbit with respect to potentially occluding bodies (such as the Earth and Moon in the case of an NRHO) is repeatable, thereby enabling long-term eclipse avoidance. To define resonance, two types of orbital period, sidereal and synodic, are defined. Sidereal period is focused on the time required for one celestial body (e.g., the Moon) to complete one revolution (precisely, 360 degrees) in its orbit about another (such as the Earth). For example, after one sidereal period of the Moon, a viewer fixed in the center of Earth would see the Moon return to the same location in the sky. The Moon's sidereal period is approximately 27.322 days. The synodic period is concerned with the time between successive conjunctions of a celestial body with the Sun, as viewed from another celestial body. After one synodic period of the Moon, a viewer fixed in the center of Earth would observe that the Moon returns to the same location with respect to the Sun; however, due to the difference between synodic and sidereal period, the

Moon would *not* appear in the same location in the sky. The Moon's synodic period is approximately 29.531 days, slightly longer than its sidereal period. A schematic illustrating both types of orbital period appears in Figure 5.9.

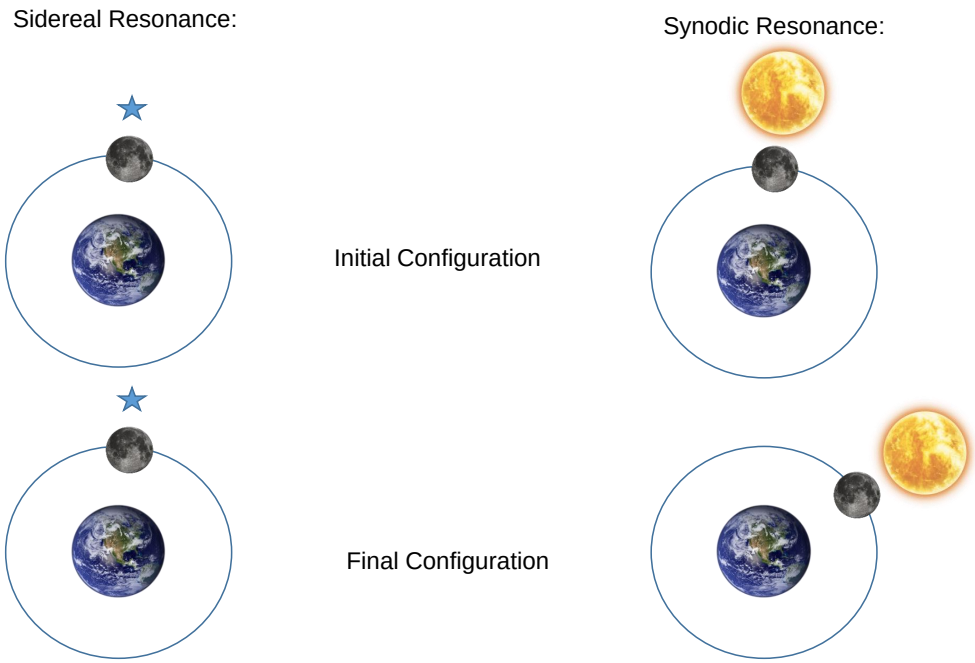

Figure 5.9. Sidereal and Synodic Resonance Schematics

Spaceraft orbital resonance is then defined as the case where the orbital period of the vehicle is in an *integer ratio* with either the synodic or sidereal period of the system. For example, in the Earth-Moon system, a spacecraft in a y:k synodic resonant halo orbit completes precisely 'y' revolutions about the Moon over the course of 'k' synodic periods of the Moon about the Earth, or in other words, the orbital period of the orbit is 'k/y' that of the synodic period of the Moon about the Earth.

Due to the goal of avoiding long duration, frequent, lunar eclipses, the location of the Moon with respect to the Sun and, therefore, the synodic resonance, is a priority. Figure 5.10 displays the y:1 and y:2 synodic resonances for the L_2 halo orbits (computed in the CR3BP), plotted as a function of perilune radius. Note, only

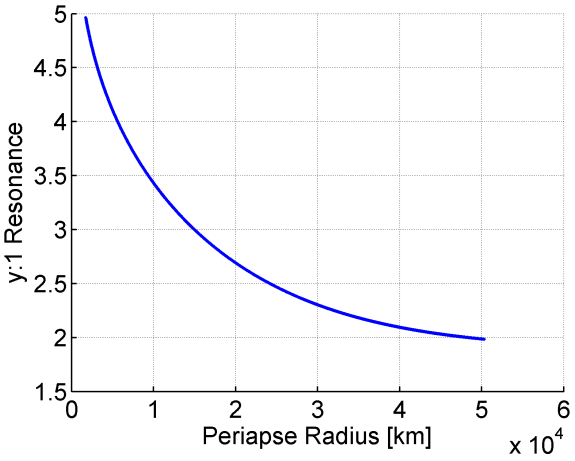

(a) The y:1 synodic resonance indicates that the spacecraft completes y revolutions of the halo orbit in one lunar synodic period.

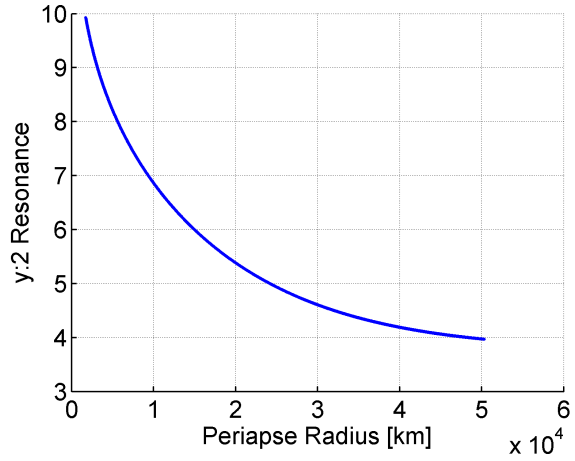

(b) The y:2 synodic resonance reflects a spacecraft that completes y revolutions of the halo orbit in two lunar synodic periods.

Figure 5.10. Synodic resonance of the L_2 halo family as a function of perilune radius.

integer ratios are considered resonant orbits. In Figure 5.10, the ratio y:k reflects the number of completed revolutions, denoted as 'y,' along a specific halo orbit per

'k' synodic cycles of the Moon. For example, a 4:1 synodic resonance occurs for an NRHO with perilune radius of about 5600 km; 4:1 synodic resonance indicates that four revolutions of the NRHO are completed over one lunar synodic period, or that the period of this particular halo orbit is one quarter that of the lunar synodic period. Additionally, a 3:1 synodic resonance occurs for an NRHO possessing a perilune radius equal to approximately 15000 km, while the 9:2 resonant NRHO corresponds to a perilune radius of about 3150 km. The 3:1 synodic resonant orbit, as computed in both the CR3BP and in the higher-fidelity Earth, Moon, Sun, and Jupiter (EMSJ) ephemeris model, appears in Figure 5.11 in the Sun-Moon rotating frame. The Sun-Moon rotating frame is selected for visualization of this orbit since the characteristic looping pattern, indicating resonance, is apparent in this view for synodic resonant orbits. The NRHO in Figure 5.11 completes three complete revolutions over one lunar synodic period; therefore, three distinct lobes appear in the Sun-Moon Rotating frame with each lobe corresponding to one revolution of the NRHO. Generally, for a y:1 synodic resonant orbit, 'y' distinct lobes are observed. For an orbit in a y:2 synodic resonance, 'y' lobes appear, however, the path encompasses the Moon twice rather than once since 'y' revolutions are completed over two lunar synodic periods. Note that in the Sun-Moon rotating frame, not only does synodic resonance become apparent, but also that the Moon's shadow is fixed in the positive x-direction (i.e., the direction oriented from the Sun to the Moon). Clearly, lunar eclipses are completely avoided by aligning the lunar shadow with 'gaps' in the trajectory geometry via careful epoch selection. Assuming an insertion into apoapsis of the NRHO, modifying the date of insertion essentially rotates the trajectory in the Sun-Moon rotating frame allowing the lunar shadow to be positioned favorably. As an example, in Figure 5.11, a large gap, resulting from a lobe within the geometry of the 3:1 synodic resonant NRHO, is aligned along the x-axis in the Sun-Moon rotating frame, thus, for this specific epoch date, no lunar eclipse events are encountered. Similar planning applies to other synodic resonant orbits; if a large gap in the orbital geometry is aligned along the positive x-axis, lunar eclipse events can be eliminated.

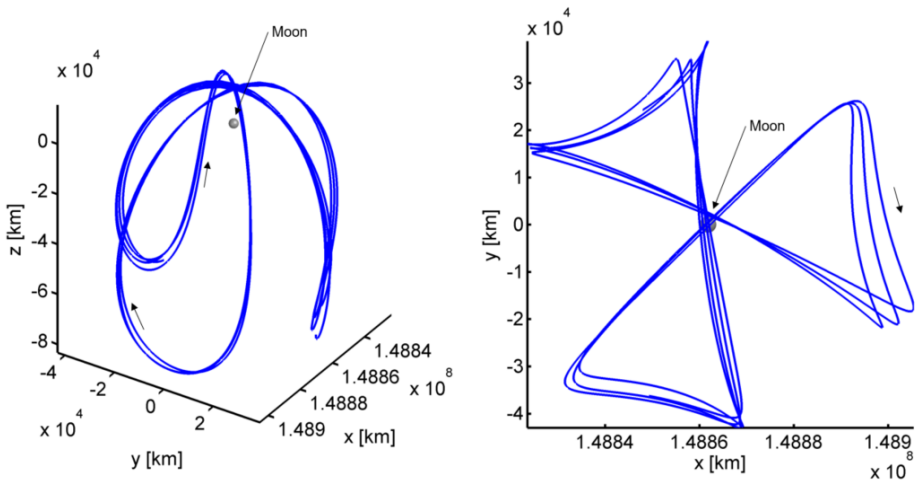

(a) A 3:1 synodic resonant NRHO as computed in the CR3BP shown in the Sun-Moon rotating frame.

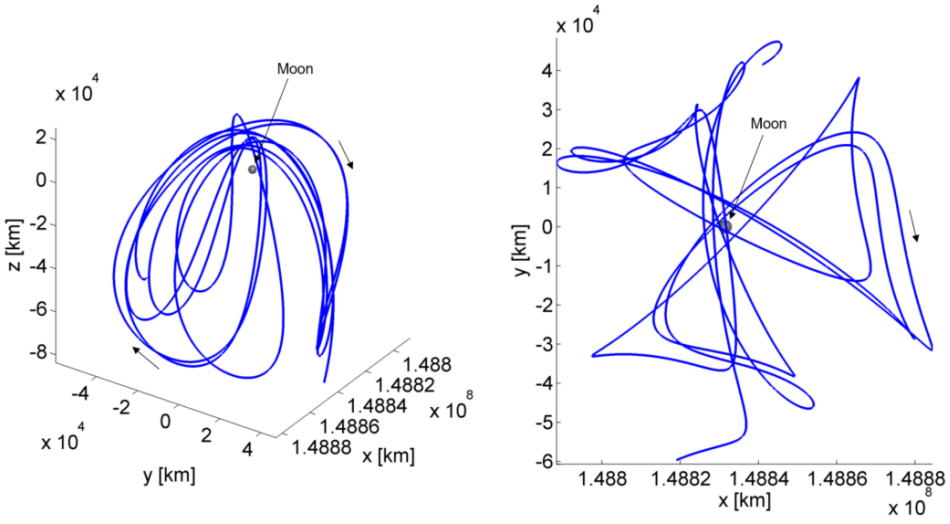

(b) A 3:1 synodic resonant NRHO as computed in the EMSJ ephemeris model shown in the Sun-Moon rotating frame.

Figure 5.11. Ten revolutions of a 3:1 synodic resonant NRHO plotted in the Sun-Moon rotating frame.

To explore a second example, consider a sample 4:1 synodic resonant NRHO as computed in the EMSJ ephemeris model. This orbit is plotted in the Sun-Moon

rotating frame in Figure 5.12 with an insertion epoch selected such that all lunar eclipse events are avoided. Note that the lunar shadow (also reflecting the solar direction) is also added in the figure. Note that this orbit, computed using version 3.0.006 of the Adaptive Trajectory Design (ATD) program, [48] has an insertion epoch date of January 25, 2025, however the insertion in this case is *not* at apoapsis. Effective avoidance of lunar eclipsing is accomplished through careful epoch selection paired with an appropriate resonant orbit leading to favorable geometry of the selected orbit in the Sun-Moon rotating frame. However, eclipses due to the Earth's shadow are also a concern. However, due to NRHO geometry, if the spacecraft apoapsis occurs during each full lunar phase, passage through the Earth's shadow is also avoided. If an Earth eclipse is unavoidable, due to the out-of-plane orbital geometry or other mission constraints, the spacecraft is near periapsis along the NRHO during the event, therefore moving quickly and ensuring a short eclipse duration.

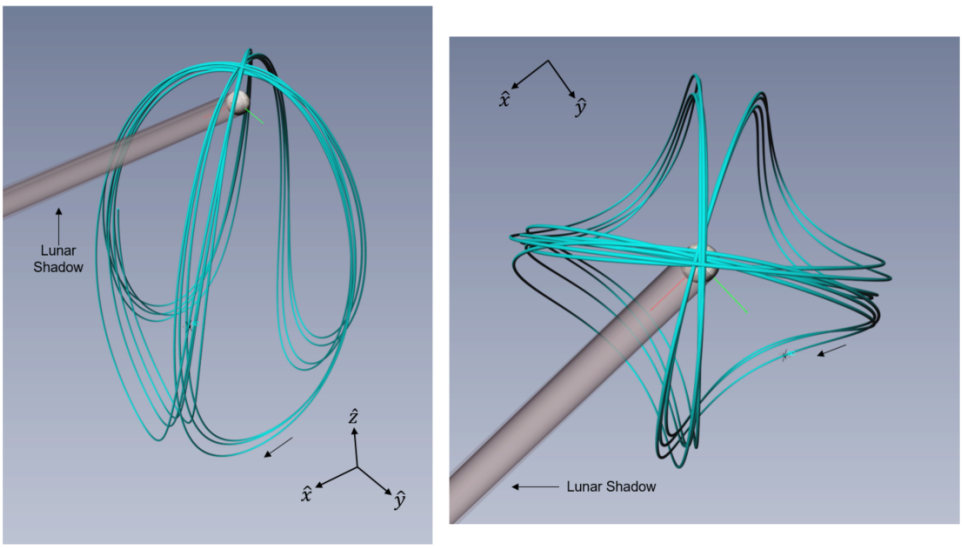

Figure 5.12. A 4:1 synodic resonant NRHO in the Sun-Moon rotating frame. The shadow of the Moon passes through a large gap in the trajectory, completely eliminating lunar eclipse events. [34]

Other mission requirements may dictate an orbital geometry or epoch date such that a lunar eclipse cannot be avoided. As an example of a trajectory that does encounter lunar eclipse events, a 9:2 synodic resonant orbit with an insertion epoch of January 25, 2025, constructed in the ephemeris model and computed using version 3.0.006 of ATD, [48] is plotted in Figure 5.13. In this case, the lunar shadow does not cleanly pass through the very narrow gaps in the orbit and, therefore, for this particular eclipse and trajectory duration, two lunar eclipse events result. The eclipse events are highlighted in red. These eclipse events are each about 60 minutes in duration. For a 9:2 synodic resonant orbit, careful selection of an insertion epoch date can, in fact, completely eliminate the lunar eclipsing in this trajectory, however, due to the narrow trajectory gaps at this resonance, epoch date selection may be more challenging than for the 4:1 synodic resonant NRHO.

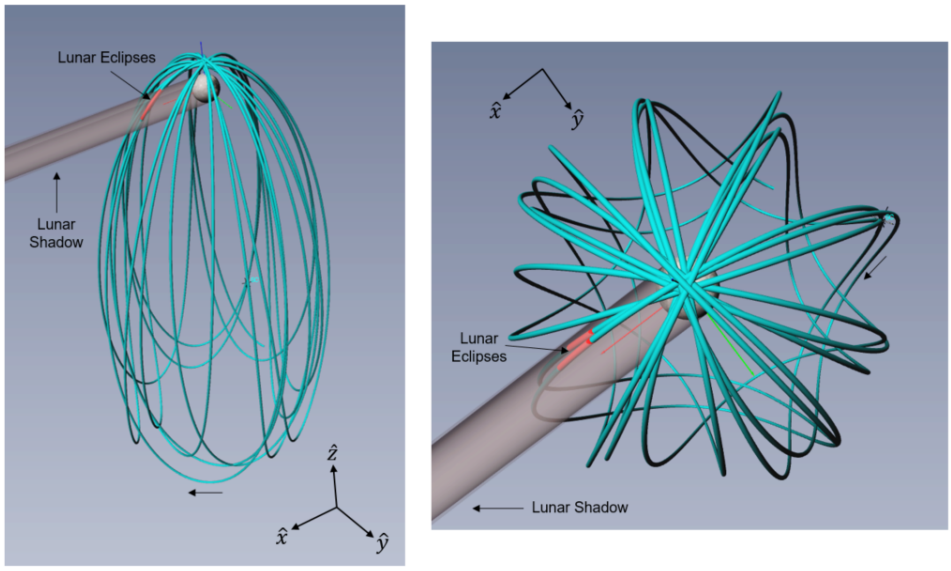

Figure 5.13. A 9:2 synodic resonant NRHO in the Sun-Moon rotating frame. The shadow of the Moon encounters a portion of the trajectory, noted in red. [34]

A non-resonant NRHO with perilune radius equal to 10114 km is constructed in the CR3BP and is plotted in Figure 5.14. Since the period of this NRHO is 8.6346 days, it is neither resonant with the synodic or the sidereal period of the Moon. As such, there are no gaps in the trajectory for straightforward avoidance of a lunar shadow, indicating that lunar eclipsing events may be particularly challenging to avoid for this orbit (or non-synodic resonant orbits, in general). As an alternative, careful phasing may be necessary to minimize lunar eclipses.

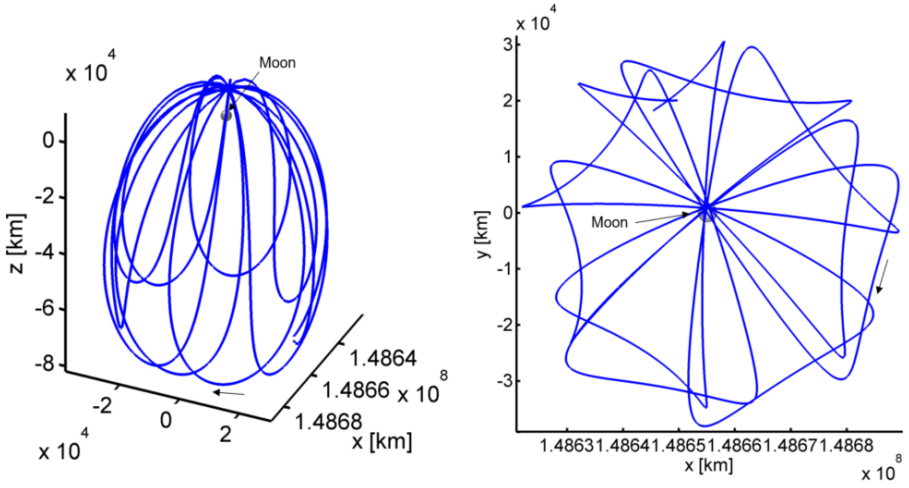

Figure 5.14. A non-resonant NRHO, as computed in the CR3BP, as viewed in the Sun-Moon rotating frame.

5.2.2 Eclipse Duration

For spacecraft in NRHOs that do indeed encounter the shadows of celestial bodies, the duration of time within shadow is based on the geometry of a celestial body's shadow cone. Parameters to compute the shadow geometry and, therefore, the eclipse duration are defined in Figure 5.15. The umbra, colored green in Figure 5.15, is the darkest part of the shadow, defined as the fully shaded interior region where the

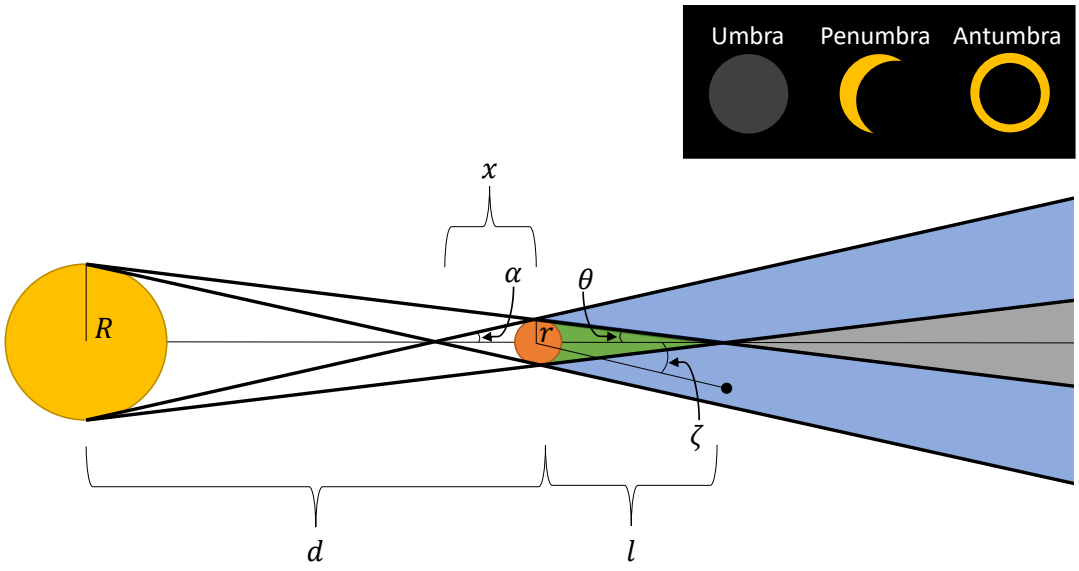

Figure 5.15. Shadow Geometry for a General Celestial Body

light source (i.e., the Sun) is completely obscured by the occluding body (the Earth or the Moon). The inset in Figure 5.15 illustrates that the Sun appears completely blacked out in a total solar eclipse, as viewed from a spacecraft within the umbra of an occluding body. The penumbra, in blue, is defined as a partially shadowed region surrounding the umbra; a viewer in the penumbra observes a sliver of the light source or a partial solar eclipse. The appearance of the Sun to a viewer in the penumbra is demonstrated in the inset in Figure 5.15. The antumbra, the grey area in the figure, is defined as the region where only a portion of the light source is obscured by the occluding body, i.e., at this distance, the relative size of the occluding body is such that it cannot completely block the Sun. A viewer in the antumbra views a ring of light, as apparent in the Figure 5.15 inset. To compute the geometry of the shadow cone, multiple angles and distances are defined. In Figure 5.15, R is the radius of the light source, or Sun (i.e., the yellow sphere) and r is the radius of the occluding body (the Earth or the Moon, i.e., the orange sphere). Additionally, d is the distance

between the center of the light source and the center of the occluding body. Using geometry, the dimensions of the shadow cones are computed as

$$l = \frac{rd}{R - r} \tag{5.6}$$

$$x = \frac{rd}{R + r} \tag{5.7}$$

$$\alpha = \tan^{-1}\left(\frac{r}{x}\right) \tag{5.8}$$

$$\theta = \tan^{-1}\left(\frac{r}{l}\right) \tag{5.9}$$

Using these expressions, the dimensions of the shadow cones corresponding to the penumbra and umbra are easily computed. Once the geometry of the umbra is available, the geometry of the antumbra is found by simply noting that the angle θ is also the cone angle of the antumbra. Simple logic then determines if the spacecraft (denoted by a black dot) is within shadow. First, define $\mathbf{r_{S,s/c}}$ as the vector from the Sun to the spacecraft, $\mathbf{r_{S,O}}$ as the vector from the Sun to the occluding body, and $\mathbf{r_{O,s/c}}$ as the vector from the occluding body to the spacecraft. Then, the spacecraft is in the penumbra if

$$r_{O,s/c}\sin(\zeta) \leq (x + \frac{\mathbf{r_{S,O}}}{r_{S,O}} \bullet \mathbf{r_{O,s/c}})\tan\alpha \tag{5.10}$$

and

$$r_{S,s/c} > r_{SE} \tag{5.11}$$

The spacecraft is located in the umbra if

$$r_{O,s/c}\sin(\zeta) \leq (l - \frac{\mathbf{r_{S,O}}}{r_{S,O}} \bullet \mathbf{r_{O,s/c}})\tan\theta \tag{5.12}$$

and

$$r_{S,s/c} > r_{SE} \tag{5.13}$$

where unbolded quantities indicate the magnitude of the corresponding vector. Depending on mission constraints, if the spacecraft is in shadow for less than a predetermined duration, with eclipse events occurring sufficiently far apart in time, a trajectory with eclipse encounters remains a valid design choice. An example of 15 revolutions along a 4:1 synodic resonant NRHO trajectory, computed in the EMSJ ephemeris model, that encounters eclipses is plotted in Figure 5.16(a). Note that the locations along the trajectory where a spacecraft moving in this NRHO is within shadow are colored in the Moon-centered inertial view; a shadow crossing that is cyan indicates that the vehicle is within the lunar penumbra, a trajectory segment colored magenta indicates that the spacecraft is in the lunar umbra, and similarly, green denotes that the vehicle is within the Earth's penumbra, while a red color indicates that the spacecraft is in the Earth umbra. The orange box in the Sun-Moon rotating frame plot identifies the approximate region along the NRHO that encounter lunar eclipses.

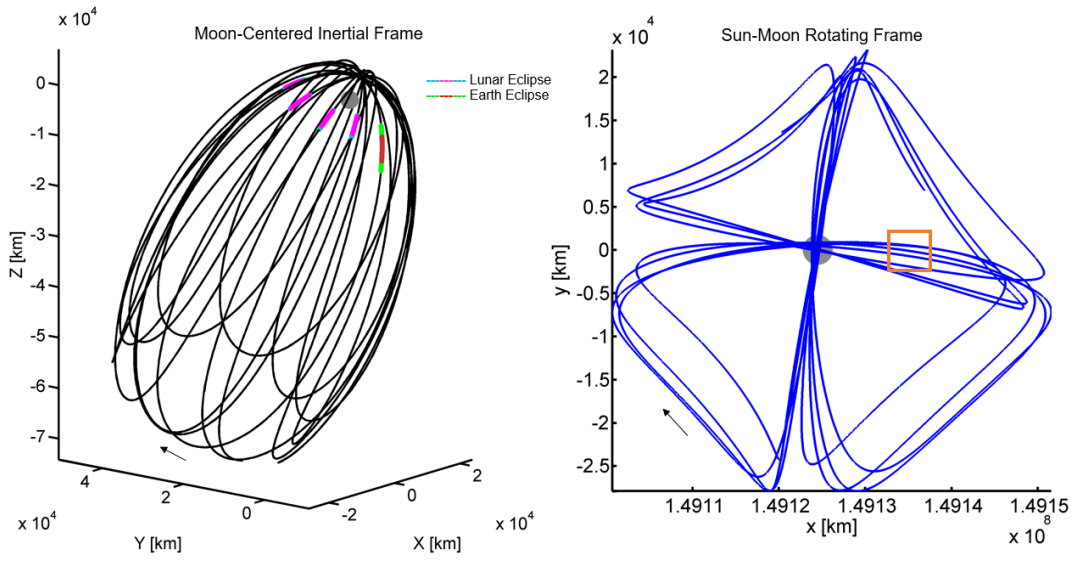

(a) A vehicle in a 4:1 synodic resonant NRHO with an apoapsis insertion date of January 25, 2025 encounters both lunar and Earth eclipses.

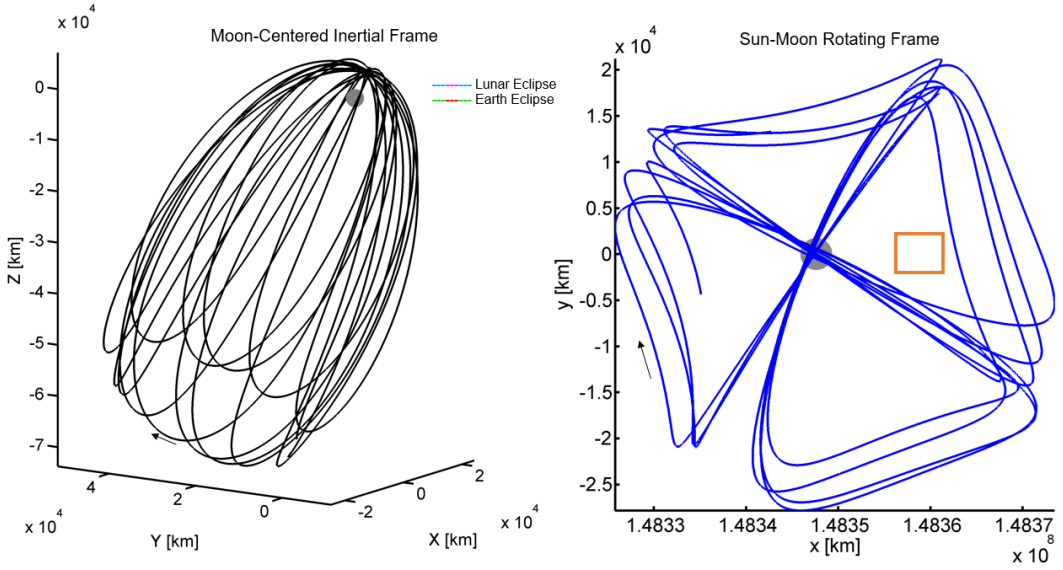

(b) A vehicle in a 4:1 synodic resonant NRHO with an apoapsis insertion date of January 1, 2025 encounters no eclipses.

Figure 5.16. Epoch date determines characteristics of shadow encounters in a 4:1 synodic resonant NRHO.

The duration of individual shadow crossings of the spacecraft, along with the time interval between shadow events are important parameters for operations. For a sample resonant NRHO–one not tuned for eclipse avoidance–eclipse information is reported in Table 5.1. Note that the time between lunar eclipse encounters is approximately

Table 5.1. Shadow events for a January 25, 2025 apoapsis insertion into a 4:1 synodic resonant NRHO.

Event Number	Occluding Body	Shadow Duration [hours]	Time Until Next Eclipse Event [days]
1	Moon	1.3087	29.4752
2	Moon	1.5015	7.3982
3	Earth	2.9098	21.8323
4	Moon	1.4848	29.4685
5	Moon	1.3547	Not Computed

29.4 days, approximately equal to the synodic period of the Moon or four times the period of the 4:1 synodic resonant NRHO. Thus, for an insertion epoch of January 25, 2025 a spacecraft moving on this orbit encounters a lunar eclipse every fourth revolution, as expected. It is apparent in Figure 5.16(b) that by shifting the apoapsis insertion date, the NRHO effectively "rotates" in the Sun-Moon rotating frame and the vehicle no longer encounters any eclipses over the time period considered. Note that in Figure 5.16(b), no portion of the trajectory now passes through the the orange box that indicates the approximate region of the lunar shadow, i.e., the lunar shadow passes through the gap in the orbit.

An additional example illustrates the influence of the epoch date on eclipse encounters. Assume the baseline trajectory is a 9:2 synodic resonant NRHO, as computed in the EMSJ ephemeris model. Two different dates for apoapsis insertion into the 9:2 synodic resonant NRHO are represented in Figure 5.17 (January 1, 2025 in Figure

5.17(b) and January 25, 2025 in Figure 5.17(a)). Similarly to the 4:1 synodic resonant NRHO plotted in Figure 5.16, an adjustment in the epoch date for the insertion effectively rotates the NRHO in the Sun-Moon rotating frame, changing the location of the lunar shadow relative to the orbit and, therefore, the eclipsing event frequency. In this example, for an insertion epoch of January 1, 2025, over 15 revolutions of the 9:2 synodic NRHO, a spacecraft experiences a total of 1.8053 hours of eclipse with 58.9792 days between eclipses. For an insertion epoch of January 25, 2025, a vehicle experiences slightly less shadow time (1.2381 hours), however, the shadow events occur only 12.9304 days apart. The eclipse events for both examples are detailed in Tables 5.2 and 5.3. As is apparent in Figure 5.17(a) and in Table 5.2, one eclipse

Table 5.2. Shadow events for a January 25, 2025 apoapsis insertion into a 9:2 synodic resonant NRHO.

Event Number	Occluding Body	Shadow Duration [hours]	Time Until Next Eclipse Event [days]
1	Moon	0.8883	12.9304
2	Moon	0.3498	Not Computed

Table 5.3. Shadow events for a January 1, 2025 apoapsis insertion into a 9:2 synodic resonant NRHO.

Event Number	Occluding Body	Shadow Duration [hours]	Time Until Next Eclipse Event [days]
1	Moon	0.9260	58.9792
2	Moon	0.8792	Not Computed

occurs over a much shorter duration than the other. This difference in eclipse duration is due to the path of the spacecraft through the shadow cone, as illustrated in Figure 5.18. If the trajectory passes through the center of the shadow cone, similar to

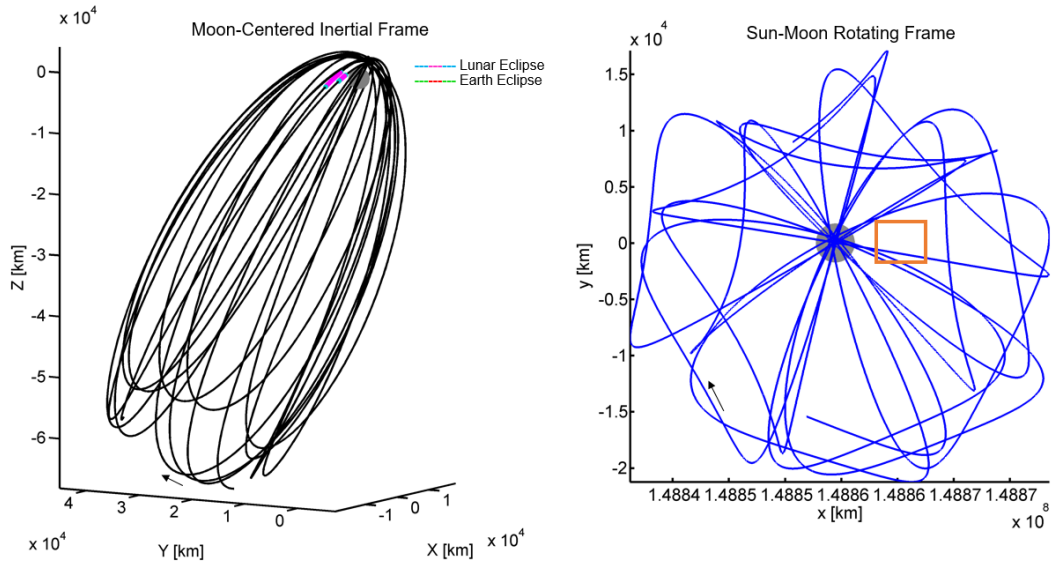

(a) A vehicle in a 9:2 synodic resonant NRHO with an apoapsis insertion date of January 25, 2025.

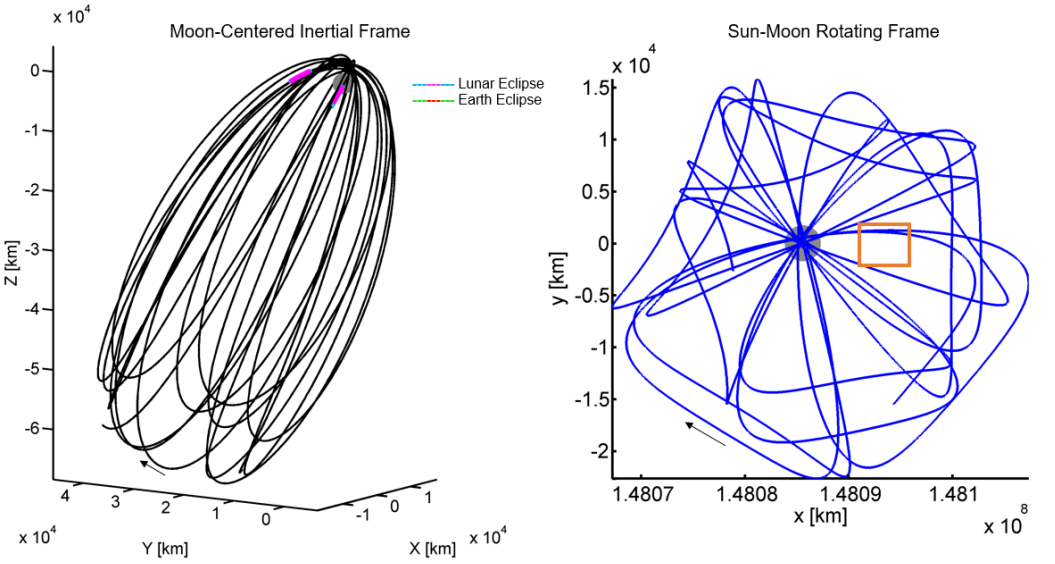

(b) A vehicle in a 9:2 synodic resonant NRHO with an apoapsis insertion date of January 1, 2025.

Figure 5.17. Epoch date determines characteristics of shadow encounters in a 9:2 synodic resonant NRHO.

path 1 (in orange) the duration of the shadow is longer than if the spacecraft passes through the shadow near the edge, as illustrated by path 2 (in green).

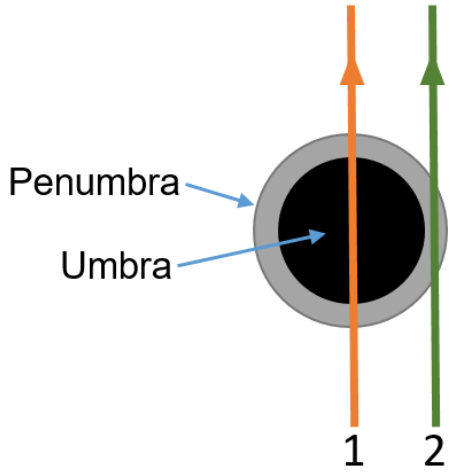

Figure 5.18. The location of transit of the shadow cone influences eclipse duration.

Eclipsing considerations are important in the selection of an orbit for a long-duration mission, however, it is clear that the NRHO geometry plays an important role in determining the frequency of eclipse events. More specifically, by focusing upon a synodic resonant orbit with large gaps (such as the 4:1 synodic resonant orbit) and carefully selecting an epoch date for insertion such that the lunar shadow passes through a gap in the trajectory (as viewed in the Sun-Moon rotating frame), lunar eclipses can be successfully avoided. Additionally, due to the large orbital velocity near periapsis on the NRHOs, any Earth eclipses are relatively short. The NRHOs are favorable from a natural eclipse avoidance standpoint.

5.3 Transfers

To assess the accessibility and applicability of the NRHOs to the DSG proving-ground goals, [1] preliminary transfer trajectories to these periodic orbits that depart from Earth and trajectores that move from the NRHOs to the DROs are constructed. Transfer paths from Low Earth Orit (LEO) to the orbit of interest, the NRHOs, are an important first step in validating the NRHOs as a staging-ground orbit. [45] Additionally, access to other orbits in cislunar space is considered. Pathways to and from other orbits in the Earth-Moon neighborhood and in the vicinity of the gateway orbit, the NRHO, is an additional goal of the DSG plan, in preparation of the Deep Space Transport (DST) functionality. [1, 5] The NRHOs on the L_2 side of the Moon are selected due to the increased ease of access and generally lower transfer costs when compared to trajectories that originate in the vicinity of the L_1 Lagrange point. [30] Recall that southern NRHOs are useful from the standpoint of long-duration coverage of the lunar south pole, a desirable location for a Moon-based facility. [33]

5.3.1 Accessing NRHOs from Low Earth Orbit

The goal of this preliminary investigation is to demonstrate that the L_2 NRHOs can be easily and directly accessed from LEO using a transfer trajectory that is suitable for crewed missions. A relatively low cost transfer, with a short time of flight, that serves as a direct path from LEO to the NRHOs supports the investigation into the suitability of these periodic orbits for the DSG. Additionally, constructing a transfer path that possesses no close flybys of the Moon is desirable from a navigational standpoint.

Methodology

To begin a preliminary transfer design assessment for trajectories from LEO to the NRHOs, a departure altitude and arrival orbit are selected. Here, a departure from a 200 km altitude circular LEO is assumed and, for baseline designs, the 4:1 synodic resonant southern NRHO is selected. In this example of a direct transfer, the arrival at the NRHO is constrained to be tangential and located at apolune. Such a constraint may be limiting but is reasonable for a preliminary trial. Apolune is selected for the arrival location on the NRHO due to its low sensitivity as compared to perilune. Propulsive maneuvers at locations of lower sensitivity are preferred from a navigational standpoint.

To compute a transfer between LEO and the apolune location along the NRHO, an initial guess is initially generated. Propagating forward from a LEO condition (perturbed in velocity) generates a variety of trajectory arcs. These trajectory arcs are plotted in configuration space; then, a path observed to possess desirable behavior, i.e., a trajectory that approaches the lunar vicinity, is selected. Additionally, the velocity vector near the end of the selected segment is generally in the same direction as the velocity at apoapsis along the NRHO, i.e., $\dot{y} < 0$. Rather than a "guess-and-check" approach to of arbitrarily determine appropriate initial states, a segment from a lunar free-return trajectory (in the CR3BP) provides a good initial guess for a segment that reaches the lunar vicinity with the proper velocity direction at the end of the segment. [30] The outbound leg of the free-return path is then discretized into a set of patchpoints for use in a multiple shooting differential corrections scheme. The trajectory segment used for an initial guess in a corrections scheme appears in Figure 5.19, plotted in black. This segment is a part of the complete free-return trajectory, plotted as a red dashed curve in the figure. For use in the multiple-shooting differential corrections scheme, the path is discretized into 15 patchpoints that are equally spaced in time, colored in magenta. A differential corrections scheme

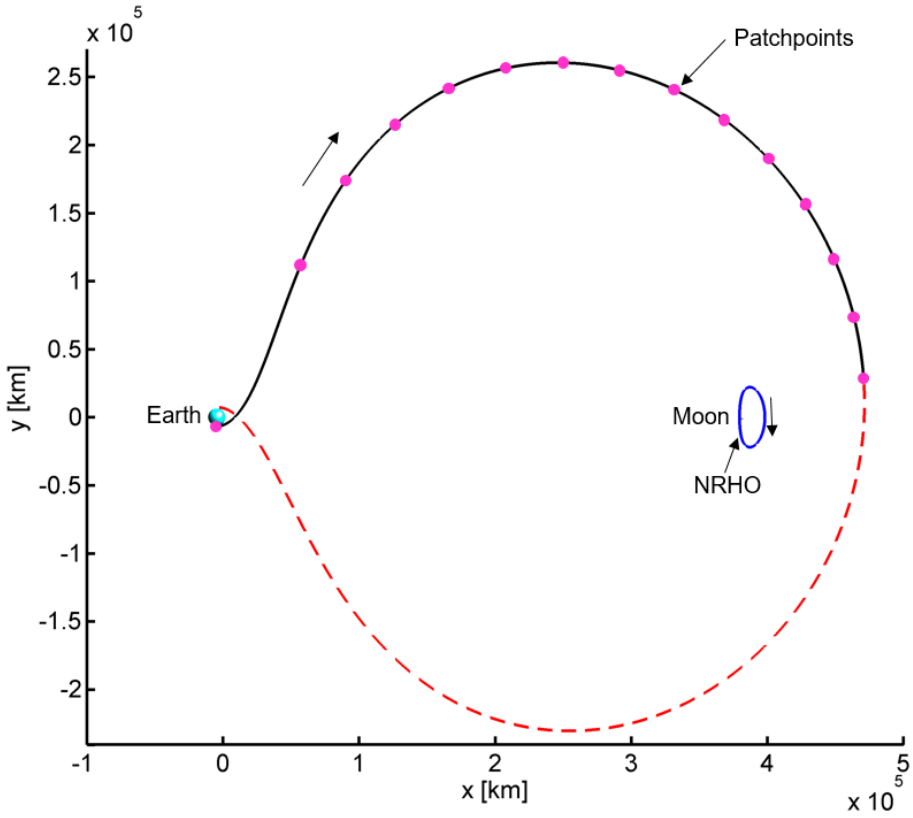

Figure 5.19. A free-return trajectory (from the CR3BP model) is used to generate an initial guess for a transfer from LEO to the 4:1 NRHO.

modifies the six-dimensional states of the patchpoints to meet the constraints on the transfer path, i.e., departure from a 200 km altitude LEO and tangential arrival at apolune along the 4:1 synodic resonant L_2 NRHO.

Results

A straightforward direct transfer option, resulting from the inital guess in Figure 5.19, is plotted in Figure 5.20. Note that the transfer maintains the geometry that is evident in the initial guess. The transfer in Figure 5.20 requires a total time of

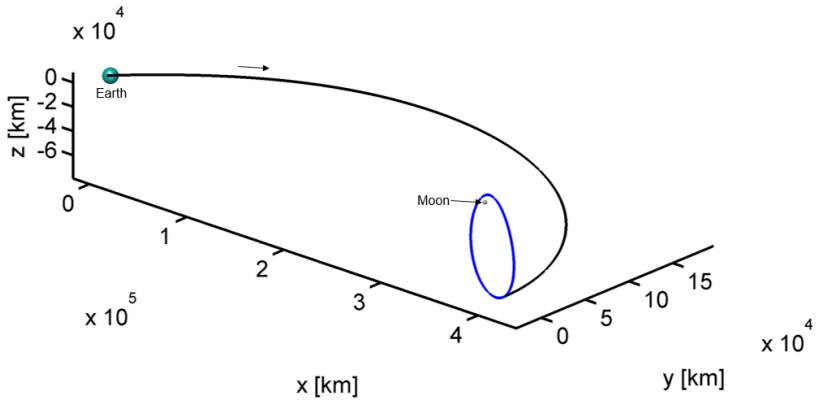

Figure 5.20. A simple transfer from a 200 km altitude LEO to apolune on the 4:1 synodic resonant L_2 NRHO, as computed in the CR3BP.

flight equal to 5.3183 days. Not surprisingly, the impulsive departure from LEO requires 3.1142 km/s while an 0.8341 km/s maneuver is necessary to capture into the NRHO, resulting in a total cost of 3.9483 km/s. An impulsive departure maneuver, i.e., ΔV, of this magnitude is reasonable to reach the lunar vicinity from LEO, and this cost is comparable to other transfers that arrive in the lunar vicinity, as explored by Capdevila. [29] Note that this preliminary transfer concept accommodates inclination; the sample transfer in Figure 5.20 departs a LEO orbit with an inclination of approximately 28 degrees (typical for a launch from Cape Canaveral, Florida which lies at a latitude of about 28.5°).

While many transfer geometries are possible, [30, 31, 45] the specific geometry observed in Figure 5.20 is reasonably low-cost, direct, and short duration. These specific characteristics are preferable for crewed missions. As an additional benefit, this transfer geometry offers relatively low sensitivity as it is observed that the majority of the path remains far from the primary bodies leading to desirable navigational characteristics. Using a continuation scheme, a similar transfer geometry from LEO to individual members of the L_2 NRHO family is constructed and plotted in Figure 5.21(b). The characteristics for this family of transfers is summarized in

Figure 5.21(a). Across the range of NRHOs, the insertion maneuver ranges between 0.8 km/s and 0.87 km/s. The time of flight is bounded between approximately 5.2 to 5.65 days. Investigation considering transfers that incorporate a flyby of the Moon

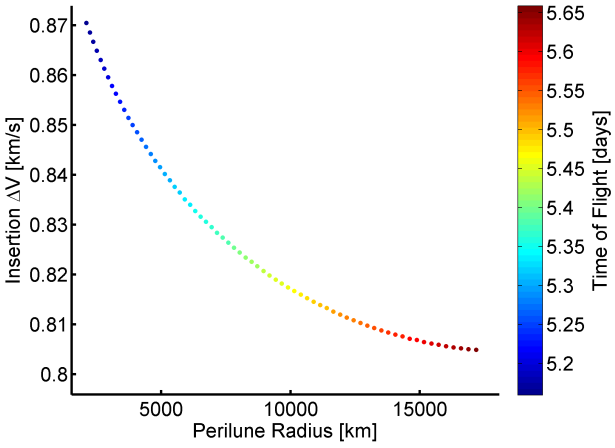

(a) Characteristics for transfers from LEO to apolune on the L_2 NRHOs.

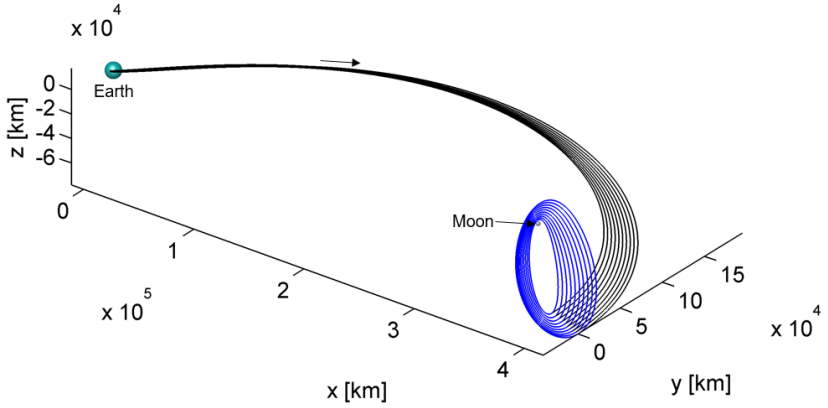

(b) Transfer family that shares a similar geometry to that shown in Figure 5.20.

Figure 5.21. Planar periodic DROs about the Moon.

are ongoing and may reduce insertion maneuver costs, as explored by Folta, Pavlak, Haapala, and Howell [30] as well as Loucks, Post, and Carrico [31]. This preliminary

investigation, however, serves to demonstrate that transferring directly from LEO to the L_2 NRHOs is feasible and can be accomplished for a reasonable cost and time of flight.

5.3.2 Accessing Distant Retrograde Orbits from NRHOs

Transfers between the primary DSG orbit, an NRHO, to other orbits in cislunar space, particularly libration point orbits, serves to prepare for future DST functionality to reach the translunar vicinity enroute to Mars and deeper into space. Gerstenmaier suggests that by the year 2026, capabilities to access other cislunar orbits from an NRHO are planned in support of the DST functionality build-up. [1] In support of this goal, various transfer options from the southern L_2 NRHOs to the DROs are preliminarily explored. For greater understanding of the dynamical environment, optimality conditions on time of flight and transfer cost are *not* enforced. A strict focus on optimal results typically reduces the basin of convergence and, therefore, the variety of transfer geometries that are able to be explored.

Transferring between an NRHO and a DRO is particularly challenging due to the relative stability of orbits in both of these families and, therefore, the lack of useful manifold structures. An additional challenge is the almost 90° plane change that is required to shift from one family to the other. [29] The NRHOs are dominated by their out-of-plane component, while the DROs are completely planar, as is apparent in Figure 5.22. Although some of the NRHOs are technically unstable, the rate of departure along the manifolds corresponding to these orbits is much too slow to represent a reasonable time of flight and, numerically these manifolds are challenging to compute as the slow departure leads to the build-up of numerical error. Therefore, for the purposes of transfer design between the NRHOs and DROs, the NRHOs are assumed to be operationally stable and their manifolds are not exploited for initial guess generation.

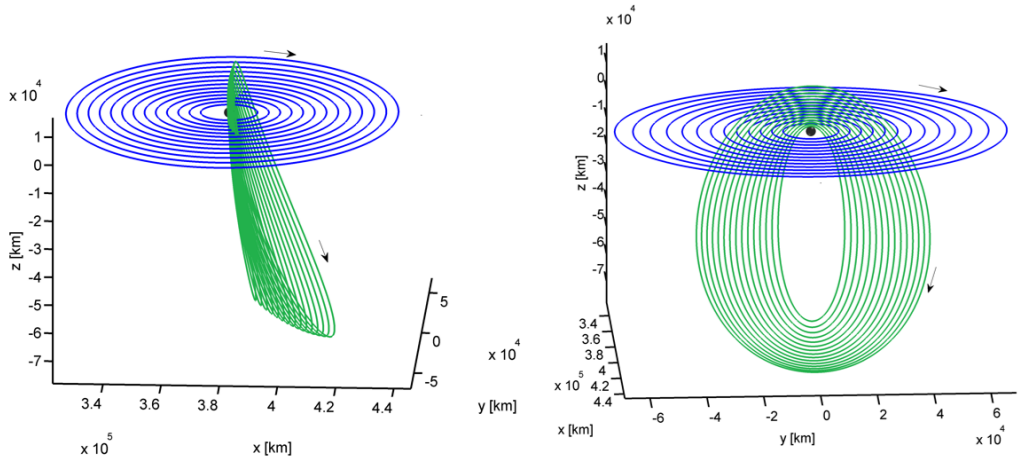

Figure 5.22. Relative orientation of the NRHOs (green) and the DROs (blue).

Methodology

Since there are no usable manifold structures for transfers between the NRHOs and DROs, an initial guess for a transfer in the differential corrections algorithm must be generated using trajectory arcs from other sources, however, must remain sufficiently accurate in the multi-body design space. For example, trajectory arcs from other known orbits in the CR3BP or manifold arcs associated with various unstable orbits can be leveraged to form an initial guess. Illustrated in Figure 5.23, various segments from other orbits are discretized to deliver patchpoints for a differential corrections scheme and then linked together into a continuous transfer; the patchpoints appear as black dots along the trajectory segments. Note that the first segment and the intermediate segment(s) do not possess patchpoints at their respective end points. Since a continuity constraint is enforced at these locations, the position state at the end of one segment must be equal to the position state at the beginning of the next and, therefore, no patchpoint is necessary. The magenta dots serve as locations along the periodic orbits for departure and arrival, respectively. Typically, departure

and arrival constraints are applied only in position, as the difference in velocity at the magenta points corresponds to the required departure and arrival maneuvers, respectively.

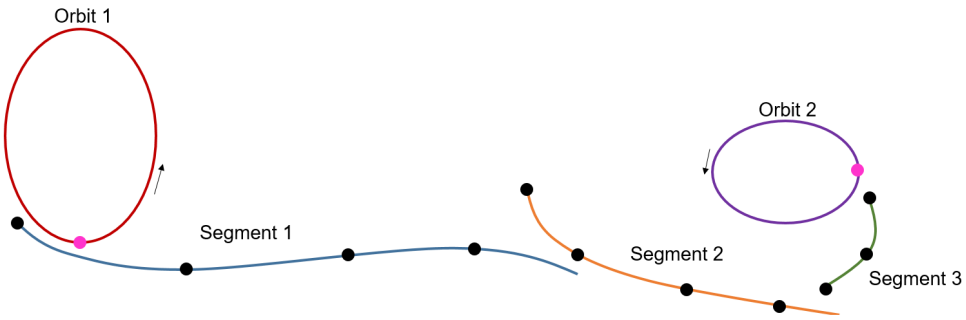

Figure 5.23. Transfer design schematic reflecting trajectory arcs discretized into patchpoints for application in a multiple shooting differential corrections scheme.

To design transfers between NRHOs and DROs, trajectory arcs from two specific sources of are the focus of this initial search for feasible transfer concepts. In the first case, termed a Poincaré Mapping Strategy, a series of initial conditions, seeded from the apolune state on the 4:1 synodic resonant NRHO are propagated forward in time and recorded on a Poincaré map. Then, a segment with desirable characteristics (e.g., one that approaches the vicinity of the DRO and crosses the xy-plane with a small $\dot{z}$ component) is discretized into patchpoints for input to a differential corrections scheme. A second approach exploits a Period-3 Distant Retrograde Orbit (P3DRO) with a Jacobi constant value equal to that of the target DRO. The P3DRO is an unstable orbit and possesses stable and unstable manifolds. Thus, a segment along the P3DRO stable manifold is selected to generate a trajectory segment that approaches the NRHO in reverse time. Since the manifolds of the P3DRO remain planar, a second segment adds to the elements of a plane change. This additional segment departs apolune of the NRHO and generates patchpoints that correspond to an arc that departs from apolune on the NRHO and approaches the vicinity of the P3DRO

manifold. Such an approach is termed the P3DRO Manifold Strategy. These two strategies yield the design framework to construct the NRHO-to-DRO transfer.

Results: Poincaré Mapping Strategy for Initial Guess Generation

Since the dynamical regime is complex and transfers must be three-dimensional to connect the NRHOs to the DROs, a Poincaré mapping strategy is employed to concisely visualize available pathways and reduce the dimension of the problem. [49] First, the apolune state corresponding to the departure NRHO is noted. Then, a range of initial conditions are constructed in terms of various maneuvers to depart the NRHO at apolune. These various departure maneuvers seed the examination of available trajectory segments and are generated by introducing a maneuver of magnitude 0.051 km/s in various directions on a unit sphere at apolune along the 4:1 synodic NRHO, as illustrated in Figure 5.24. The unit sphere is discretized into

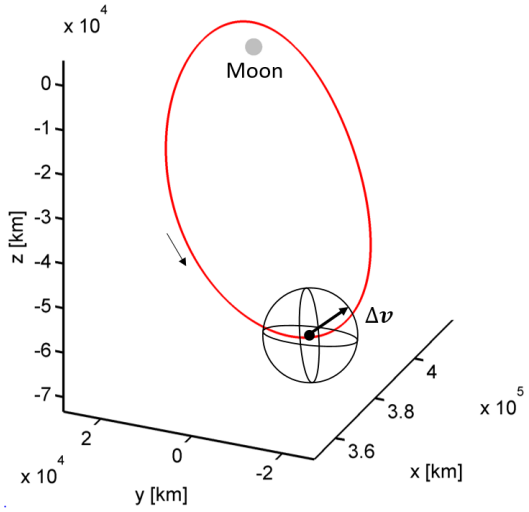

Figure 5.24. Schematic of departure maneuvers in directions along a unit sphere at apolune along a 4:1 synodic resonant NRHO, as computed in the CR3BP.

a series of directions by defining two angles, θ_{long} and θ_{lat}, corresponding to the longitude and latitude angles along the sphere, respectively. The longitude angle, θ_{long}, is defined by 30 equally spaced angles between 0° and 360° and, the latitude angle, θ_{lat}, is defined by 15 equally spaced angles between 0° and 180°. Pairs of $(\theta_{long}, \theta_{lat})$ determine the direction of the impulsive maneuver at the apolune point along the NRHO, i.e., the maneuver is defined as

$$\Delta \mathbf{V} = \Delta V \left(\sin\theta_{lat}\cos\theta_{long}\hat{x} + \sin\theta_{lat}\sin\theta_{long}\hat{y} + \cos\theta_{long}\hat{z}\right) \tag{5.14}$$

where ΔV is the magnitude of the maneuver, 0.051 km/s and $\hat{x}, \hat{y}, \hat{z}$ correspond to the rotating frame. For transfers between the NRHOs and DROs, a hyperplane is selected at $z = 0$. The DROs exist solely in the plane at $z = 0$ and, therefore, information about trajectories at this plane crossing is useful to the transfer design process. Each crossing of the hyperplane is recorded on a plot as the x-y coordinate of the crossing. To supply additional information concerning the 6-dimensional state along the trajectory at the plane crossing, a glyph is added to the map at the crossing location [49], i.e., an arrow in the direction of $(\dot{x}, \dot{y})$ is added to the plot with a length corresponding to the inverse of the magnitude of the $\dot{z}$ value at the hyperplane. Therefore, for a crossing with a large $\dot{z}$ component, the arrow will be small, and for a crossing with a small $\dot{z}$ component, the arrow will be large. The resulting x-y Poincaré map appears in Figure 5.25 with a portion of the DRO family included for completeness. A trajectory segment selected from the Poincaré map, based on desirable properties, serves as an initial guess for a transfer between an NRHO and DRO. A desirable segment is identified by a map crossing that is close to the DRO in (x, y) position space. Additionally, the in-plane velocity direction for a desirable trajectory segment, as illustrated by the orientation of the glyph, must be directed in approximate alignment with the velocity vector along the DRO (oriented clockwise in the xy-plane). Due to the planar nature of the DROs, a small $\dot{z}$ component at the crossing, indicated by a longer arrow on the map, is desired; a small $\dot{z}$ component at the $z = 0$ crossing likely leads to a smaller insertion maneuver since the trajectory

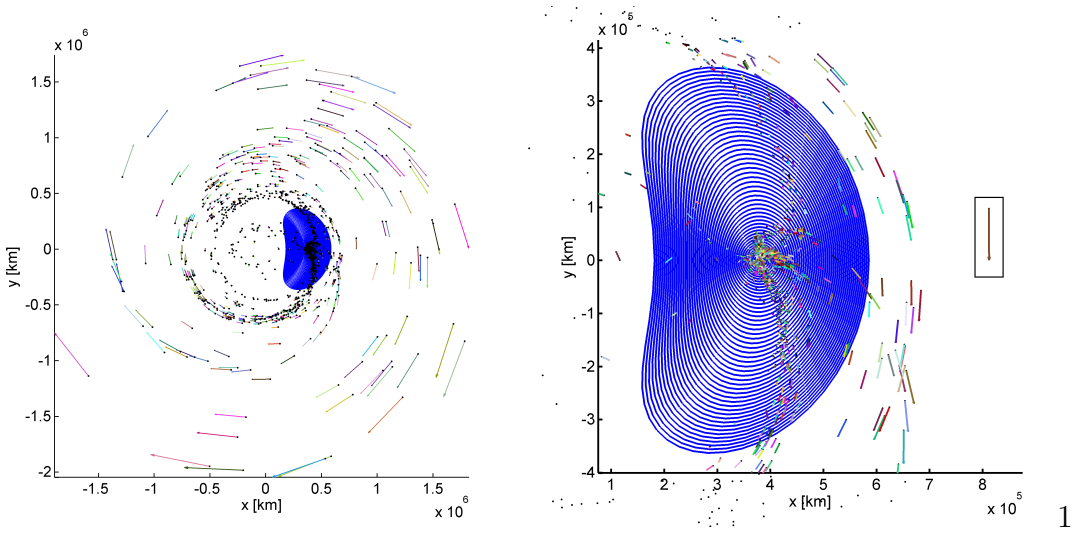

(a) Poincaré map with departure maneuver equal to 0.051 km/s at apoapsis on the NRHO.

(b) Zoomed-in view of the DRO region.

Figure 5.25. A Poincaré map is used to find a viable initial guess for a transfer trajectory from the NRHOs to the DROs.

motion is naturally more planar at the plane crossing. One such crossing is highlighted by a box in Figure 5.25(b). This crossing corresponds to an initial maneuver, computed in the CR3BP rotating frame, of $\Delta\mathbf{v} = -0.0396\hat{x} - 0.0043\hat{y} - 0.0318\hat{z}$ km/s at apolune on the 4:1 synodic resonant NRHO. Moving from the NRHO departure point to the selected plane crossing requires a time of flight of approximately 60 days. Exploiting the trajectory segment from the Poincaré map as an initial guess for a differential corrections algorithm, a transfer from the 4:1 synodic resonant NRHO to a 26.3 day period DRO is constructed, and plotted in Figure 5.26.

The transfer in Figure 5.26 includes an intermediate maneuver to aid in completing the plane change while meeting a tangential arrival constraint. This intermediate transfer is marked with a red star along the trajectory path in Figure 5.26. This transfer requires a total cost of 0.7310 km/s with a time of flight equal to 74.2627 days. Additional understanding of the transfer geometry is enhanced by considering

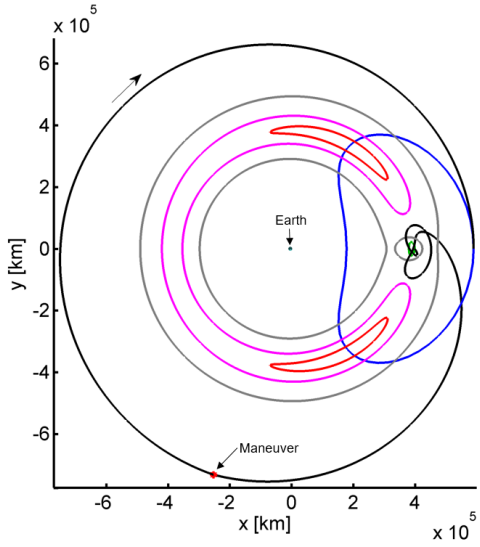

(a) Planar view of a transfer from a 4:1 NRHO to a 26.3 day period DRO.

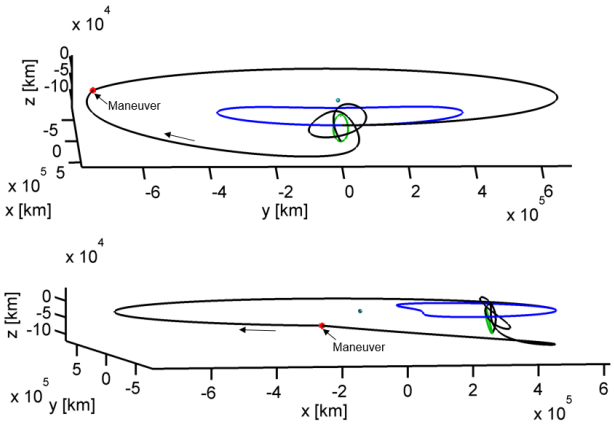

(b) Alternate out-of-plane views of a transfer from a 4:1 NRHO to a 26.3 day period DRO.

Figure 5.26. Transfer from the 4:1 synodic resonant NRHO to a 26.3 day period DRO.

the evolution of the forbidden regions over each segment along the path. The segments are separated by propulsive maneuvers and include: (1) the NRHO, (2) the segment between the NRHO departure maneuver and the intermediate maneuver, (3) the

segment between the intermediate maneuver and the DRO insertion maneuver, and (4) the DRO. The ZVCs corresponding to each trajectory segment (corresponding to different values of Jacobi constant) are plotted in the figure. In Figure 5.26, the ZVC for the Jacobi constant value corresponding to segment (1) appears in magenta; the red curve in the figure reflects the ZVC for the Jacobi constant value associated with segment (2); and, the grey curves represent the ZVC for segment (3). The ZVC for the DRO (segment (4)) is not included in the figure as the corresponding ZVS is out-of-plane and curves do not intersect with the x-y plane (i.e., $JC_{DRO} > JC_{L_4}$).

Using a continuation scheme, a transfer geometry similar to the transfer in Figure 5.26 recurs for transfers from the 4:1 synodic resonant NRHO to smaller DROs in the family. Thus, the continuation scheme relies upon the previous converged guess as an initial guess for a transfer to the next smallest DRO in the family, where the DROs are pre-computed. As a consequence, two additional examples appear in Figure 5.27. In Figure 5.27(a), a transfer to a smaller DRO with an orbital period of 20.97 days is constructed; the time of flight is 80.8 days and the total cost of the maneuvers is equal to 0.5799 km/s. An additional transfer to a second, even smaller, DRO with an orbital period of 13.76 days appears in Figure 5.27(b). The time of flight of this transfer is 75.5 days with a total ΔV equal to 1.206 km/s. Note that as the size of the target DRO changes, the Jacobi constant (and the corresponding ZVC) along each transfer segment changes, as well. The transfer in Figure 5.26 is observed to have no interaction with the ZVCs, while the transfers in Figure 5.27 both apparently approach and "bounce off" of the ZVC. Seemingly bouncing off of a ZVC results in a slightly modified geometry. The exterior part of the transfer in Figure 5.27(b), the path moving far from the Moon, expands in size to accommodate the ZVC corresponding to the third trajectory segment, plotted in grey; this third segment is associated with the path between the intermediate and arrival maneuvers. Due to the modified geometry and increase in size of the transfer, the position of the intermediate ΔV shifts from a negative $\hat{y}$ location to a location with a positive

$\hat{y}$ value. Additionally, the transfer segment between the departure maneuver and the intermediate impulsive ΔV, segment (2), decreases its value of Jacobi constant value and the associated ZVC (plotted in red in Figure 5.26) disappears from the x-y plane since the ZVS no longer intersects the plane. This specific transfer geometry suggests transfer-ZVC interactions influence the transfer characteristics.

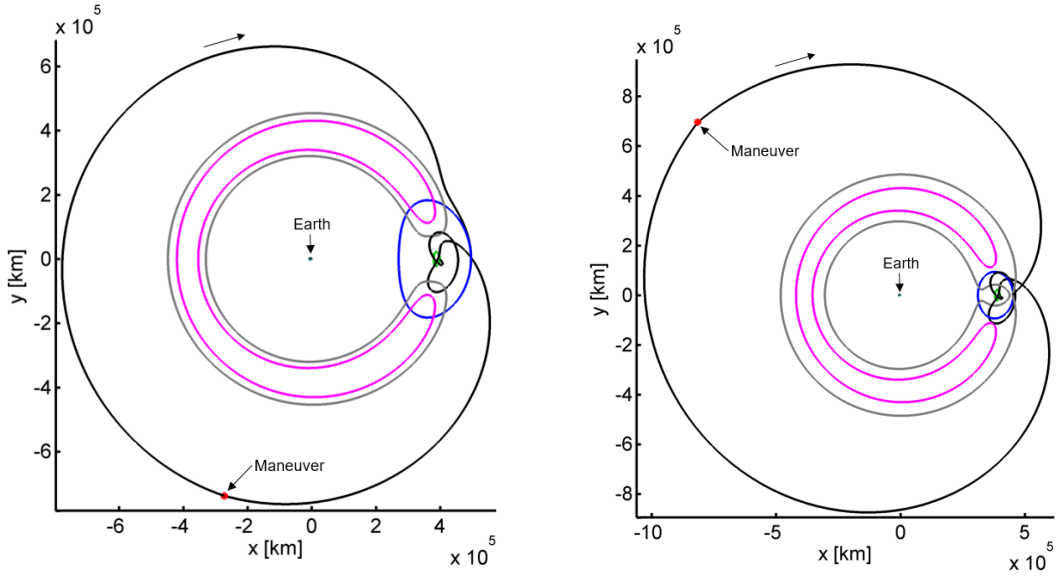

(a) Transfer from the 4:1 synodic resonant NRHO to a 20.97 day period DRO.

(b) Transfer from the 4:1 synodic resonant NRHO to a 26.3 day period DRO.

Figure 5.27. Transfers from the 4:1 synodic resonant NRHO to various DROs.

Continuing the transfer family from the original 26.3 day period DRO to a much smaller DRO family (possessing a 1 day period) results in a transfer geometry characterized by one large path in the exterior region beyond the ZVC boundary, denoted as an external transfer. This geometry is apparent in Figures 5.26 and 5.27. However, if the converged transfer to the smallest DRO is then employed to initiate a continuation scheme to determine transfers to increasingly larger DROs, the resulting family of transfers yields a slightly different geometry than the original. In other

words, if the original converged transfer is introduced as an initial guess for transfers to increasingly smaller DROs, then the family is continued in the opposite direction (towards larger DROs) once it reaches the smallest member, two different geometries with different times of flight result and require different levels of maneuvers. Examples of transfers that reflect the second type of geometry are plotted in Figure 5.28. Figure 5.28(a) exhibits a transfer to a 20.97 day period DRO, the same destination

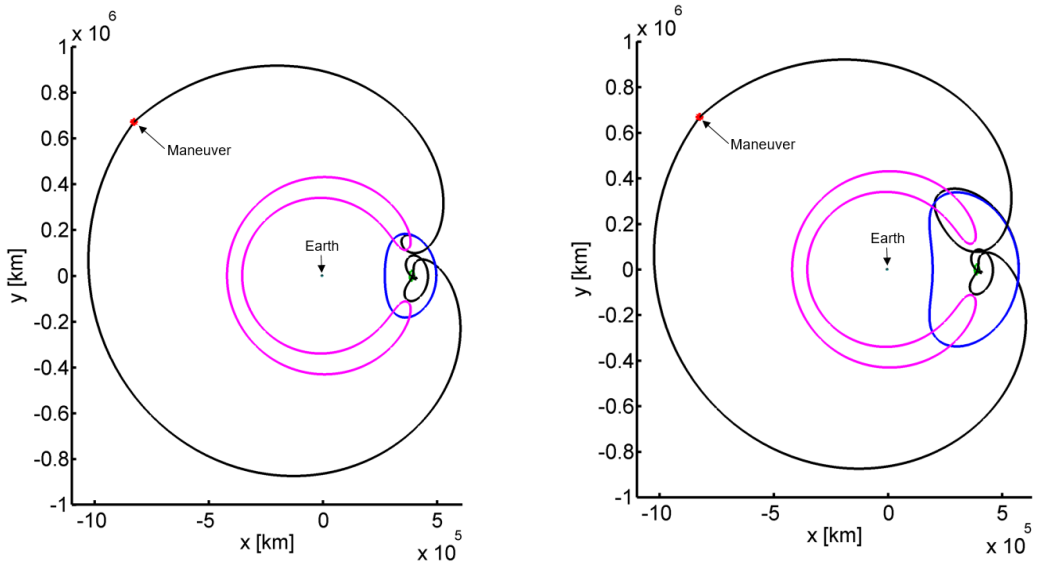

(a) Transfer from the 4:1 synodic resonant NRHO to a 20.97 day period DRO.

(b) Transfer from the 4:1 synodic resonant NRHO to a 26.3 day period DRO.

Figure 5.28. Transfers from the 4:1 synodic resonant NRHO to various DROs showing an alternative geometry.

orbit as that in Figure 5.27(a). However, the time of flight for this transfer is 82.95 days and the total transfer cost is 0.8814 km/s, slightly larger than the transfer with the original geometry. In Figure 5.28(b), a transfer to a 26.3 day period DRO, which is the same DRO as in Figure 5.26, is plotted. In the case of the second continuation process, however, the time of flight for the tranfer is 88.42 days and the total maneuver cost is 0.8574 km/s. The time of flight has increased due to the addition

of a loop in the trajectory near the insertion into the DRO. The characteristics for both geometries in the transfer family are summarized in Figure 5.29. The bottom curve, that originates at the magenta star and ends at the red star, corresponds to the first continuation direction, moving towards destination orbits that are increasingly smaller DROs. The top curve, between the red star and the green stars, corresponds to the second continuation direction, where the converged solution evolves towards larger DROs. The discontinuity in the lower curve in Figure 5.29 corresponds to a

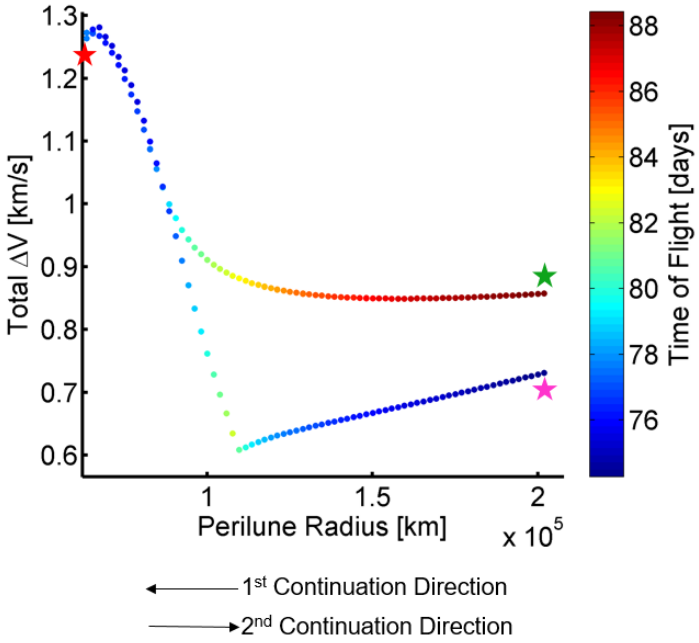

Figure 5.29. Characteristics for transfers from apolune on the the 4:1 synodic resonant NRHO to the far-side $y = 0$ location on various DROs.

location where the basin of convergence has shifted, i.e., the low-cost transfer basin that is characterized by a maneuver location with a negative y-component switches to a convergence basin that is characterized by slightly more expensive transfers that have maneuver locations corresponding to a positive y-component. Important for future developments, it is observed that continuation schemes are *not* symmetric and,

moreover, the initial guess used in a corrections method influences the geometry of the converged solution.

The second transfer geometry suggests manifolds of a periodic orbit. In fact, the third segment of these transfers (between the intermediate maneuver and the DRO insertion) shares characteristics with P3DRO manifolds. As an example, further exploration is offered of the transfer, plotted in Figure 5.30, that originates from the 4:1 synodic resonant NRHO and arrives at an 18.05 day period DRO. This particular

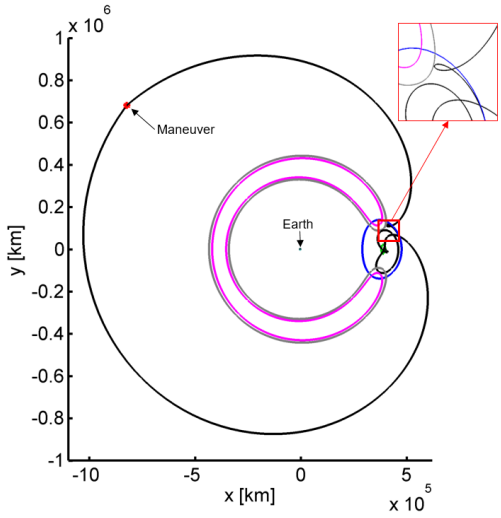

Figure 5.30. Transfer from the 4:1 synodic resonant NRHO to a 18.05 day period DRO.

transfer requires a total maneuver cost of 0.9772 km/s and a time of flight of 79.4 days. The third segment of this transfer possesses a Jacobi constant value of 3.0572. A P3DRO with the same value of Jacobi constant is plotted in Figure 5.31(a) along with the destination DRO that possesses an 18.05 day orbital period, and the 4:1 synodic resonant NRHO. Additionally, in Figure 5.31(b), the stable and unstable manifold crossings of the P3DRO in Figure 5.31(a) are plotted on an x-$\dot{x}$ Poincaré map in blue and red, respectively. This x-$\dot{x}$ Poincaré map has a hyperplane defined at the $y = 0$ plane. Propagating the third transfer segment (between the intermediate and arrival

maneuvers) of the transfer in Figure 5.30 both forward and backward in time and plotting the crossings in green on the Poincaré map in Figure 5.31(b) demonstrates that this transfer shares similar characteristics to the P3DRO manifolds; thus, the P3DRO manifolds are useful for transfer design in this region.

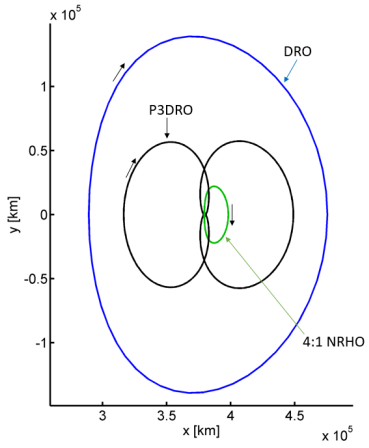

(a) A P3DRO with a Jacobi constant value of 3.0572, a DRO with orbital period of 18.05 days, and the 4:1 synodic resonant NRHO, as computed in the CR3BP.

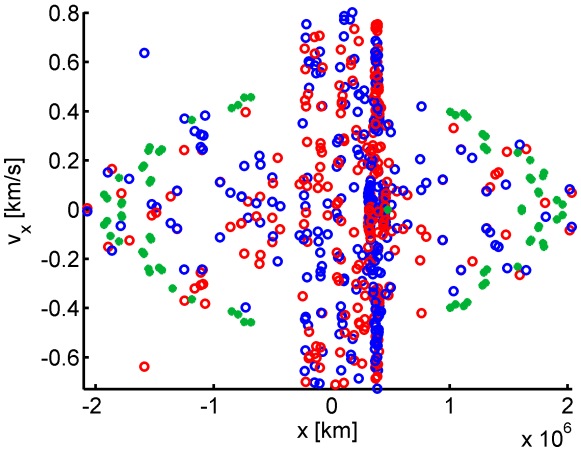

(b) Poincaré map marking crossings of the transfer arc (green dots), the unstable manifold of the P3DRO (red dots), and the stable manifold of the P3DRO (blue dots).

Figure 5.31. A particular transfer geometry that shares characteristics with the P3DRO manifolds.

Results: P3DRO Stable Manifold Strategy for Initial Guess Generation

The P3DROs are unstable planar orbits in the vicinity of the DROs with manifold structures that serve as good initial guesses for transfers between the NRHOs and DROs. As is evident in Figure 5.31, motion in cislunar space shares the characteristics of these manifolds and, therefore, suggests possible transfer geometries. To design

transfers using a P3DRO manifold, first, a DRO of interest is selected. For example, the DRO with a Jacobi constant value of 2.9418. This DRO is plotted in Figure 5.32(a). Then, selecting a P3DRO with approximately the same Jacobi constant (2.9419), also illustrated in Figure 5.32(a), the stable and unstable manifolds are computed. These manifolds are represented in blue and red, respectively, on the x-$\dot{x}$ Poincaré map with a hyperplane of $y = 0$ in Figure 5.32(b). Additionally, the

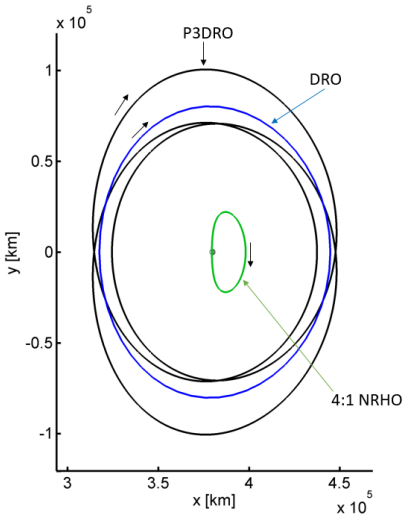

(a) A P3DRO with a Jacobi constant value of 2.9419, a DRO with Jacobi constant value equal to 2.9418, and the 4:1 synodic resonant NRHO, as computed in the CR3BP.

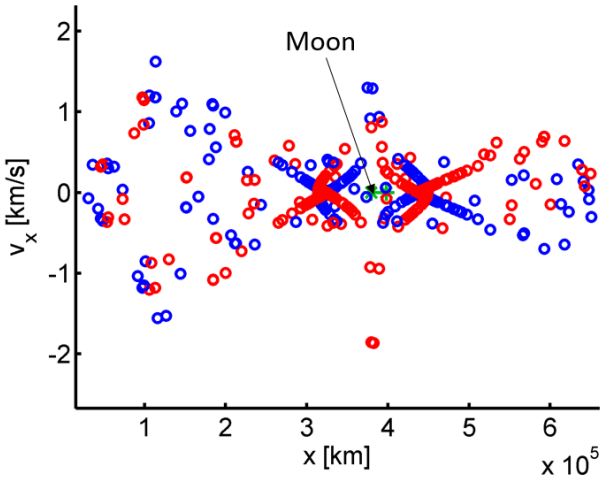

(b) Poincaré map for the stable (plotted in blue) and unstable (plotted in blue) manifolds of a P3DRO with a Jacobi constant value of 2.9419.

Figure 5.32. A particular P3DRO and DRO that possess approximately equal Jacobi constant values.

crossings corresponding to the NRHO are plotted as green stars on the map. Since the DRO and P3DRO are in close proximity, flow that departs or arrives at the P3DRO in the form of manifolds also departs from or arrives in the DRO vicinity, as well. From the Poincaré map in Figure 5.32(b), crossings that approach the NRHO vicinity (i.e., a crossing near the Moon) are preferred for further investigation. A transfer that

departs from an NRHO *towards* a DRO is the focus and, therefore, a stable manifold (potted as a blue dot in Figure 5.32(b)) is most likely to be useful since the motion along a stable manifold is consistent with the desired direction of motion. In other words, a stable manifold approach the P3DRO vicinity, and, thereby, also approaches the DRO, in forward time. A few manifolds of interest appear in Figure 5.33. These manifolds are selected directly from the Poincaré map due to their close approaches to the Moon and the fact that they are "interior" to the ZVCs. An interior transfer is explored to offer an additional transfer geometry between the NRHO and DRO. Patchpoints from the manifold are used to construct an initial guess and, due to this fact, the entire manifold is not necessary. Hence, the portion of the manifold that approaches the P3DRO is trimmed and omitted from the figure. Note that the origin of each manifold occurs in the vicinity of the NRHO and each manifold arc ends with a positive $\dot{y}$ component to allow for a smooth insertion into a DRO. Three different states from the Poincaré map are identified to generate manifold segments. The resulting manifold arcs in Figure 5.33 all approach the P3DRO differently.

Using the Poincaré Mappping Strategy, in which trajectories are seeded by departures from apolune on the NRHO, an additional segment that departs the NRHO and reaches the $y = 0$ plane crossing near the manifold segment offers a potential link to apolune point along the NRHO. This additional step offers points along the path to aid the plane change and allow for more successful convergence. Once an NRHO departure segment that approaches the desired manifold arc is identified, the patchpoints from both segments are incorporated to deliver a continuous transfer. Continuity constraints between the patchpoints and the apolune departure as well as a near-side arrival constraint are implemented in this process. A transfer from the 4:1 synodic resonant NRHO to a DRO with a Jacobi constant value approximately equal to that of the P3DRO manifold is found using the manifold segment in Figure 5.33(c). This transfer is plotted in Figure 5.34 and has a total cost of 0.5495 km/s ($\Delta V_1 = 0.2530$ km/s and $\Delta V_2 = 0.2965$ km/s) and a time of flight of 143.9 days.

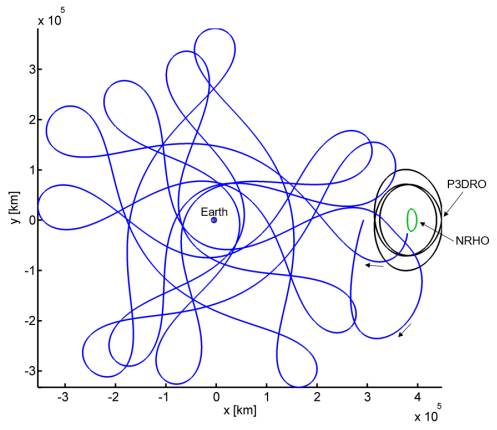

(a) x_0 = (0.7605 0 0 0.1864 0.5154 0) nd, Integration Time = -41.25 nd ≈ -179 days

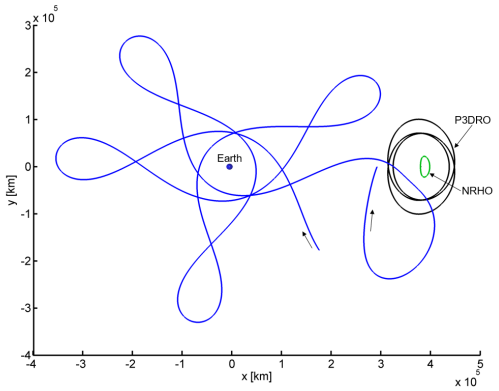

(b) x_0 = (0.7598 0 0 0.1880 0.5160 0) nd, Integration Time = -15 nd ≈ -65 days

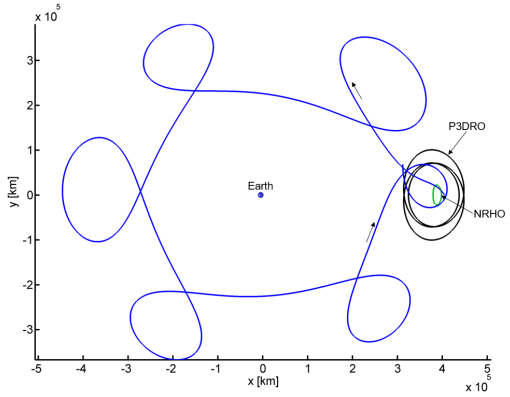

(c) x_0 = (1.0528 0 0 0.3591 0.5166 0) nd, Integration Time = +30 nd ≈ +130 days

Figure 5.33. P3DRO manifolds that offer possible transfer geometries between an NRHO and DRO.

Note that the converged transfer trajectory maintains the geometry of the initial guess. Then, a continuation process is used to maintain the path geometry for transfers to other DRO family members. The transfer family is plotted in Figure 5.35. Characteristics for this family of transfers between the 4:1 synodic resonant NRHO and the DRO family are plotted in Figure 5.36. The transfers in Figure 5.35 display resonant behavior. It is apparent that resonant orbits and their manifolds may offer

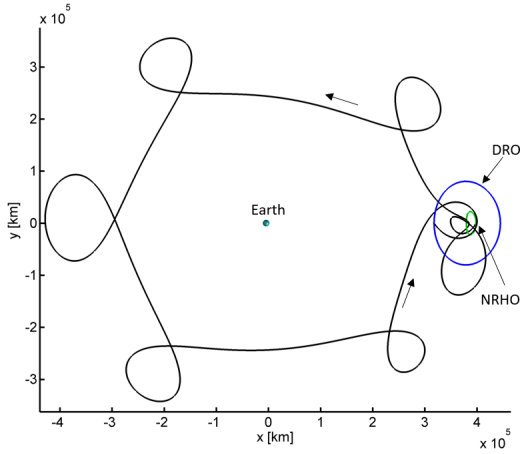

Figure 5.34. Transfer from apolune of the 4:1 synodic resonant NRHO to a 12.1534 day period DRO with Jacobi constant value of 2.9418.

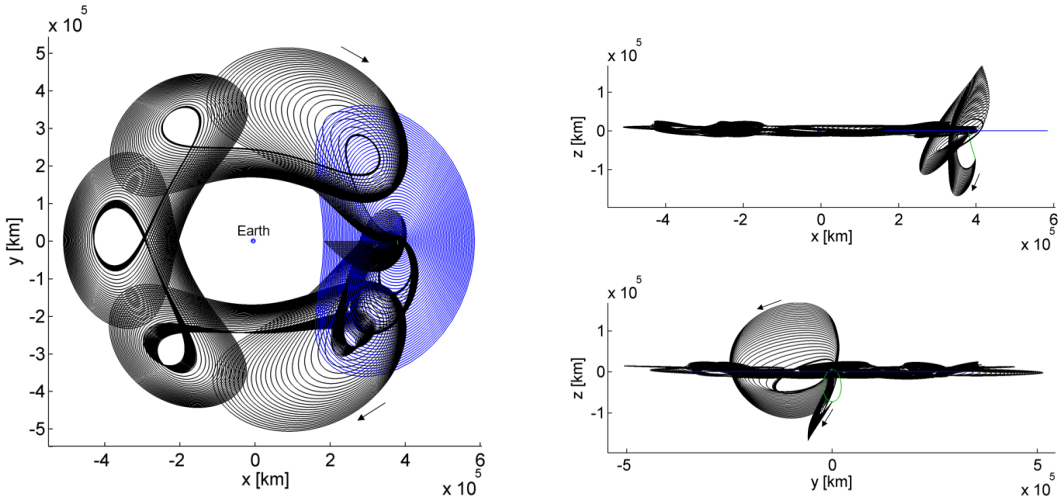

(a) x-y view of the transfer family found using the interior P3DRO stable manifold arc.

(b) Alternate views of the transfer family found using an interior P3DRO stable manifold arc.

Figure 5.35. A P3DRO stable manifold arc that remains interior to the Earth-Moon region offers an alternative transfer geometry between an NRHO and the DROs.

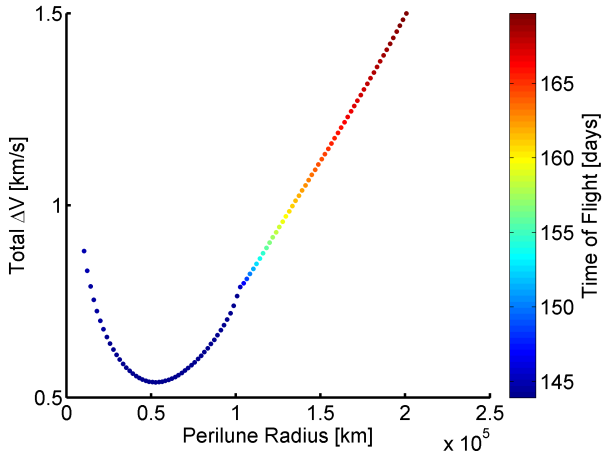

Figure 5.36. Characteristics for the transfer family plotted in Figure 5.35.

good initial guesses for transfers between stable orbits, in particular, the NRHOs and DROs. Investigation into this application is ongoing.

6. CONCLUDING REMARKS

6.1 Summary of the Present Investigation

As a far-reaching sustainable human presence in deep space is a near-term goal for a robust space economy and exploration infrastructure, the Deep Space Gateway (DSG) is currently planned as a largely Earth-independent long-term habitat on the far side of the Moon. This facility offers a proving ground for capabilities and systems, as well as a support platform for the future Deep Space Transport (DST). [1,5] An orbit of interest to support this habitat mission is a southern L_2 near rectilinear halo orbit, however, fundamental questions concerning this type of orbit are yet unanswered. Thus, the overarching goal of this investigation is the characterization of the near rectilinear halo orbits in terms of stability properties and eclipse avoidance strategies in order to support of the creation of a long-term crewed habitat in cislunar space. In pursuit of this objective, strategies for design in a multi-body dynamics regime are implemented. To begin, dynamical models and differential corrections strategies in the form of shooting algorithms are derived and defined. Using strategies to evolve related solutions, multiple examples of periodic orbit families in the CR3BP, including the DROs, P3DROs, and halo oribts, are computed and analyzed. A Poincaré mapping technique that allows for concise visualization of dynamical information as well as a strategy to compute manifolds of periodic orbits is also presented. Additionally, for higher-fidelity applications, a metric to quantify changes in orbital geometry for orbits that are transitioned into the N-body ephemeris model from the CR3BP, termed to apse angle, is defined. Linear stability analysis using the eigenvalues of the monodromy matrix to gain insight into the dynamical behavior

of perturbed trajectories nearby reference solutions is presented. From this analysis, the L_1 and L_2 NRHOs are defined as the largely out of plane portions of the halo orbit families characterized by bounded stability indices. Orbital resonance, both synodic and sidereal, is presented in the context of an eclipse avoidance strategy. A method to avoid eclipsing through the use of synodic resonance and careful choice of the insertion epoch date choice is presented.

A secondary objective of this investigation is a preliminary analysis of a direct transfer orbit to reach the NRHOs from low Earth orbit and a methodology to connect the NRHOs with the distant retrograde orbit family, neither of which possess usable manifold structures. Transfers are investigation in support of the goal to ultimately move easily within and beyond cislunar space. A direct transfer from LEO to an NRHO is formulated by using a portion of a lunar free-return trajectory as an initial guess. A short time of flight and total transfer cost are comparable to other transfers to the vicinity found by previous authors. Two strategies are explored for designing transfers between stable orbits (the NRHOs and the DROs) that lack usable manifold structures typical of transfer design strategies. Both strategies, a Poincaré mapping technique seeded with conditions that depart from apolune on a representative NRHO, and a method of initial guess generation that uses P3DRO stable manifolds, produce viable transfers.

6.2 Concluding Remarks

To be considered a suitable candidate for a long-term crewed habitat in cislunar space, the NRHOs must possess various favorable characteristics. Through this investigation, it can be concluded that:

- In terms of linear stability properties, the NRHOs are suitable candidates for a long-duration habitat in cislunar space. It is found that the L_2 NRHO class

of orbits is stable or nearly stable in a linear sense, indicating that departure or escape from these orbits is slow. Due to these favorable stability properties, stationkeeping costs over a long-duration are likely to be low as spacecraft will naturally remain close to the nominal NRHO path. This conclusion was found to hold in the higher-fidelity ephemeris model, as well.

- Eclipse events can be easily avoided by using orbits in resonance with the synodic period of the Moon. Orbits with y:1 synodic resonances, such as the 3:1 and 4:1 synodic resonant NRHOs, are particularly suitable for eclipse avoidance due to the large gaps in the trajectory, as viewed in the Sun-Moon rotating frame, that allow for the lunar shadow to be entirely avoided with careful insertion epoch selection. Earth eclipses can be avoided, as well, if the spacecraft is near the apolune of the NRHO during the full Moon phase. If eclipse events do occur, however, they are relatively short as the largely out of plane geometry of the NRHOs lead to eclipses occurring near perilune where the spacecraft moves quickly. Careful insertion epoch selection paired with synodic resonance allows for the NRHOs to meet potential eclipse time constraints without the use of any maneuvers. Since resonant behaviors are maintained in a higher-fidelity ephemeris model, eclipse avoidance strategies are applicable to real-world scenarios.

- NRHOs are a good candidate for a staging-ground location since transfers from these stable orbits to other locations of interest are available using multiple transfer geometries. Effective methods for trajectory design between stable (or nearly stable) orbits that lack usable manifold structures are offered by a Poincaré Mapping Strategy and a P3DRO Stable Manifold Strategy. Each of these strategies offers insight into the dynamical regime and allows for viable transfer designs.

Overall, it can be concluded from this investigation that the L_2 southern NRHOs, due to their stability properties, natural eclipse avoidance characteristics, and the

availability of transfer options to other orbits in the vicinity, are a suitable candidate for a long-duration habitat in cislunar space, such as the Deep Space Gateway.

6.3 Recommendations for Future Work

As plans grow near for the construction of a long-duration facility in cislunar space that will serve as a staging ground for deep space missions to expand human presence deeper into the solar system, there are many interesting topics related to this investigation that have yet to be addressed. In particular a deeper understanding of available transfers to other destinations, such as low Lunar orbit, the butterfly family, returns to low Earth orbit, and paths that reach into translunar space, will aid in the understanding of the dynamical road-map that exists in the vicinity of the NRHO class of orbits. Such an orbital road-map will help provide the necessary insight to develop a permanent presence of humans in deep space and support the Deep Space Transport capability. A transfer study of this type should include the use of periodic orbits and their manifolds for initial guess generation; preliminary results of this study suggest that this type of initial guess can aid in transfer design. Once an understanding of available transfer geometries and destinations is developed, i.e., basins of convergence are better characterized and understood, optimization of transfer trajectories should be conducted. Real world implementations of transfers to other destinations typically includes optimal time of flight or minimized total transfer cost. An understanding of any additional basins of convergence for transfer geometries prior to optimization allows for educated decisions to be made in the mission design process. Thus, additional transfer geometries between the NRHOs and DROs should be explored, as well.

REFERENCES

REFERENCES

[1] William H. Gerstenmaier. Progress in Defining the Deep Space Gateway and Transport Plan. `https://www.nasa.gov/sites/default/files/atoms/files/nss_chart_v23.pdf`, March 28, 2017.

[2] B. F. Kutter and G. F. Sowers. Cislunar-1000: Transportation Supporting a Self-Sustaining Space Economy. In *AIAA SPACE 2016, Long Beach, CA*, 2016.

[3] Michele Gates, Dan Mazanek, Brian Muirhead, Steve Stich, Bo Naasz, Paul Chodas, Mark McDonald, and Jim Reuter. NASA's Asteroid Redirect Mission Concept Development Summary. In *Aerospace Conference, 2015, IEEE*, March 7-14, 2015.

[4] Darrel Raines. Orion Multipurpose Crew Vehicle (MPCV) Overview - Embedded Flight Software. 2015.

[5] Deep Space Gateway to Open Opportunities for Distant Destinations. `https://www.nasa.gov/feature/deep-space-gateway-to-open-opportunities-for-distant-destinations`, March 28, 2017. Editor: Kathryn Hambleton.

[6] John V. Breakwell and John V. Brown. The 'Halo' Family of 3-Dimensional Periodic Orbits in the Earth-Moon Restricted 3-Body Problem. *Celestial Mechanics*, 20:389–404, November 1979.

[7] Kathleen Howell and John Breakwell. Almost Rectilinear Halo Orbits. *Celestial Mechanics*, 32(1):29–52, January 1984.

[8] Robert W. Farquhar. *The Control and Use of Libration-Point Satellites*. Ph.D. Dissertation, Stanford University, 1968.

[9] Kathleen Connor Howell. Three-Dimensional, Periodic, 'Halo' Orbits. *Celestial Mechanics*, 32:53–71, January 1984.

[10] Isaac Newton. *The Principia: Mathematical Principles of Natural Philosophy*. University of California Press, 1999. Translated by I. Bernard Cohen and Anne Whitman.

[11] J. Barrow-Green. *Poincaré and the Three Body Problem, History of Mathematics Vol. 11*. American Mathematical Society, 1997.

[12] Victor Szebehely. *Theory of Orbits: The Restricted Problem of Three Bodies*. Academic Press, Inc., New York, 1967.

[13] G. W. Hill. Reasearches into the Lunar Theory. *American Journal of Mathematics*, 1(1):5–26, 1878.

[14] J. H. Poincaré. *Les Méthodes Nouvelles de la Mécanique Céleste, Vol. 1-3*. Gauthier-Villars et fils, 1899.

[15] Robert Farquhar, Daniel Muhonen, and L. Church. Trajectories and Orbital Maneuvers for the ISEE-3/ICE Comet Mission. In *Astrodynamics Conference*, 1984.

[16] Mark Woodard, David Folta, and Dennis Woodfork. ARTEMIS: the First Mission to the Lunar Libration Orbits. In *21st International Symposium on Space Flight Dynamics, Toulouse, France*, 2009.

[17] Martin W. Lo, Bobby G. Williams, Williard E. Bollman, Dongsuk Han, Yungsun Hahn, Julia L. Bell, Edward A. Hirst, Robert A. Corwin, Philip Hong, Kathleen C. Howell, et al. Genesis Mission Design. *Journal of the Astronautical Sciences*, 49(1):169–184, 2001.

[18] Herbert B. Keller. *Numerical Solution of Two Point Boundary Value Problems*. SIAM, 1976.

[19] S. M. Roberts and J. S. Shipman. Continuation in Shooting Methods for Two-Point Boundary Value Problems. *Journal of Mathematical Analysis and Applications*, 18(1):45–58, 1967.

[20] S. M. Roberts and J. S. Shipman. Justification for the Continuation Method in Two-Point Boundary Value Problems. *Journal of Mathematical Analysis and Applications*, 21(1):23–30, 1968.

[21] Mike R. Osborne. On Shooting Methods for Boundary Value Problems. *Journal of Mathematical Analysis and Applications*, 27(2):417–433, 1969.

[22] Thomas A. Pavlak. *Trajectory Design and Orbit Maintenance Strategies in Multi-Body Dynamical Regimes*. Ph.D. Dissertation, School of Aeronautics and Astronautics, Purdue University, West Lafayette, Indiana, May 2013.

[23] Forest Ray Moulton. *Periodic Orbits*. Carnegie Institution of Washington, 1920.

[24] Daniel J. Grebow. Generating Periodic Orbits in the Circular Restricted Three-Body Problem with Applications to Lunar South Pole Coverage. M.S. Thesis, School of Aeronautics and Astronautics, Purdue University, West Lafayette, Indiana, May 2006.

[25] Wayne R. Schlei. *Interactive Spacecraft Trajectory Design Strategies Featuring Poincaré Map Topology*. Ph.D. Dissertation, School of Aeronautics and Astronautics, Purdue University, West Lafayette, Indiana, May 2017.

[26] Davide Guzzetti, Emily M. Zimovan, Kathleen C. Howell, and Diane C. Davis. Stationkeeping Analysis for Spacecraft in Lunar Near Rectilinear Halo Orbits. In *Paper No. AAS 17-395, AAS/AIAA Spaceflight Mechanics Meeting, San Antonio, Texas*, February 2017.

[27] Diane C. Davis, Sagar A. Bhatt, Kathleen Howell, Jiann-Woei Jang, Ryan Whitley, Fred Clark, Davide Guzzetti, Emily Zimovan, and Gregg Barton. Orbit Maintenance and Navigation of Human Spacecraft at Cislunar Near Rectilinear Halo Orbits. In *Paper No. AAS 17-269, AAS/AIAA Spaceflight Mechanics Meeting, San Antonio, Texas*, February 2017.

[28] Davide Guzzetti. GRANT: NNX13AK60 Final Report. Technical Report, Purdue University, NASA, 2016.

[29] Lucia Capdevila, Davide Guzzetti, and Kathleen Howell. Various Transfer Options from Earth into Distant Retrograde Orbits in the Vicinity of the Moon. In *AAS/AIAA Space Flight Mechanics Meeting, Sante Fe, New Mexico*, January 2014.

[30] David C. Folta, Thomas A. Pavlak, Amanda F. Haapala, and Kathleen C. Howell. Preliminary Design Considerations for Access and Operations in Earth-Moon L1/L2 Orbits. In *Paper No. AAS 13-339, 23rd AAS/AIAA Spaceflight Mechanics Meeting, Kauai, Hawaii*, February 10–14, 2013.

[31] Michel Loucks, Kevin Post, and John Carrico. Lunar Near Rectilinear Orbits and Cis-Lunar Transfer Trajectories in Support of the Deep Space Proving Ground. In *Paper No. AAS 16-244*, 2016.

[32] Ryan Whitley and Roland Martinez. Options for Staging Orbits in Cis-Lunar Space. In *IEEE Aerospace 2015*, March 2015.

[33] D. J. Grebow, M. T. Ozimek, K. C. Howell, and D. C. Folta. Multi-Body Orbit Architectures for Lunar South Pole Coverage. In *Paper No. AAS 06-179, AAS/AIAA Spaceflight Mechanics Meeting, Tampa, Florida*, January 2006.

[34] Emily M. Zimovan, Kathleen C. Howell, and Diane C. Davis. Near Rectilinear Halo Orbits and Their Application in Cis-Lunar Space. In *3rd IAA Conference on Dynamics and Control of Space Systems, People's Friendship University of Russia, (RUDN University), Moscow, Russia*, May 30th – June 1st 2017.

[35] Wang Sang Koon, Martin W. Lo, Jerrold E. Marsden, and Shane D. Ross. *Three Body Problem and Space Mission Design*. Springer-Verlag, 2006.

[36] Charles H. Acton Jr. Ancillary Data Services of NASA's Navigation and Ancillary Information Facility. `https://naif.jpl.nasa.gov/naif/`, January 1996.

[37] Natasha Bosanac. *Leveraging Natural Dynamical Structures to Explore Multi-Body Systems*. Ph.D. Dissertation, School of Aeronautics and Astronautics, Purdue University, West Lafayette, Indiana, August 2016.

[38] Joaquim R. R. A. Martins, Peter Sturdza, and Juan J. Alonso. The Complex-Step Derivative Approximation. *ACM Transactions on Mathematical Software*, 29:245–262, 2003.

[39] R. A. Broucke. Periodic Orbits in the Restricted Three-Body Problem with Earth-Moon Masses. Technical Report, Jet Propulsion Laboratory, 1968.

[40] M. Hénon. Numerical Exploration of the Restricted Problem. VI: Hill's case: Non-Periodic Orbits. *Astronomy and Astrophysics*, 9:24–36, 1970.

[41] E. Doedel and V. Romanov. Elemental Periodic Orbits Associated with the Libration Points in the Circular Restricted 3-Body Problem. *International Journal of Bifurcation and Chaos*, 17(8):2625–2677, 2007.

[42] Herbert B. Keller. Numerical Solutions of Bifurcations and Nonlinear Eigenvalue Problems. *Applications of Bifurcation Theory*, pages 359–384, 1977. Editor: Paul Rabinowitz, Academic Press.

[43] A. E. Roy and M. W. Ovenden. On the Occurence of Commensurable Mean Motions in the Solar System. The Mirror Theorem. *Monthly Notices of the Royal Astronomical Society*, 115:296–309, 1955.

[44] B. Hufenback, K. Laurini, N. Satoh, C. Lange, R. Martinez, J. Hill, M. Landgraf, and A. Bergamasco. International Missions to the Lunar Vicinity and Surface – Near-Term Mission Scenario of the Global Space Exploration Roadmap. In *IAF 66th International Astronautical Congress*, October 2015.

[45] Jacob Williams, David E. Lee, Ryan L. Whitley, Kevin A. Bokelmann, Diane C. Davis, and Christopher F. Berry. Targeting Cislunar Near Rectilinear Halo Orbits for Human Space Exploration. In *Paper No. AAS 17-395, AAS/AIAA Spaceflight Mechanics Meeting, San Antonio, Texas*, February 2017.

[46] Lawrence Perko. *Differential Equations and Dynamical Systems*. Springer-Verlag, New York, 3rd Edition, 2001.

[47] Daniel J. Grebow, Martin T. Ozimek, Kathleen C. Howell, and David C. Folta. Multi-Body Orbit Architectures for Lunar South Pole Coverage. *Journal of Spacecraft and Rockets*, 45(2):348–358, 2008.

[48] Amanda Haapala. Adaptive Trajectory Design (ATD) Tutorial: Version 3.0. Tutorial, Purdue University, NASA Goddard Space Flight Center, 2014.

[49] Amanda Haapala. *Trajectory Design in the Spatial Circular Restricted Three-Body Problem Exploiting Higher-Dimensional Poincaré Maps*. Ph.D. Dissertation, School of Aeronautics and Astronautics, Purdue University, West Lafayette, Indiana, December 2014.